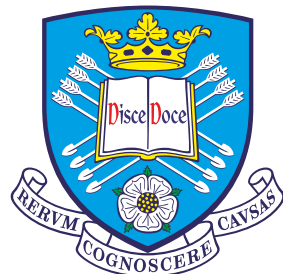


# **Macrospicules, Jets and the Solar Chromosphere**



**Samuel Middleton Bennett**

School of Mathematics and Statistics

The University of Sheffield

This dissertation is submitted for the degree of

*Doctor of Philosophy*

Supervisor: Robertus Erdélyi

September 2016



To Sue and Steve, thank you for everything.



## Acknowledgements

I would like to thank my family, Sue, Steve and Kathryn for their confidence in me, infinite patience when and for keeping me grounded. Kimberley, thank you for your non-stop belief in me. I also need to thank all the teachers, lecturers and assistants from high school to University (twice), who have imparted to me their knowledge, wealth of experience and enthusiasm for Physics, and without whom I would not have been able to achieve so much.

I am an immensely annoying person to live with, so I would like to thank Nabil Freij for putting up with my slovenliness for three and a half years. Stuart Mumford, for the Python lessons, particularly during first year, and Drew Leonard for being a rubber duck on all too regular a basis. Thank you to Stevie Chaffin, Alex Hague, Freddie Mather, Chris Nelson and all the solar physics PhD's in the office of doom, for mutual stress in the difficult times and elation in the good. I would also like to thank everyone at the University of Sheffield Cycle Club (UoSCC!), there are too many to mention by name, you were an excellent outlet when I needed one.



## Abstract

Given recent advancements in observational solar physics, both in quality and quantity, the time is right to revise the chromospheric feature, macrospicules. These jet-like phenomena are larger than their semi-namesake spicules, which only extend to 10 Mm as an absolute maximum and are ubiquitous in the solar chromosphere, particularly within intergranular lanes. However, macrospicules are not as large as the so-called coronal jets or the X-ray jets, generally observed in hotter temperature lines and penetrating much higher into the solar atmosphere. The aim of this work is to better classify macrospicules as a population and to detect any possible relationships; such as relation to the solar cycle, impacts on coronal heating or as a solar wind accelerator, on a global scale.

This is achieved first by means of a statistical sample of macrospicules. We utilise the first two and a half years of Atmospheric Imaging Assembly on board the Solar Dynamics Observatory's (AIA/SDO) operation window and measure macrospicules properties throughout. This two and a half year sample acts as a proxy for the ramp from solar minima in mid 2010 to maxima in late 2012. Over this time period we find a general increasing trend for the properties of the macrospicules. A range of characteristic features of the macrospicules, such as: maximum length and width, maximum velocity and lifetime are stated and compared to the current literature. This same sample is then tested against the Carrington longitude to test for any relation to what has been termed, an active longitude. In this case, we find that the macrospicules do have a correlation to the so-called active longitude.

Lastly, this work presents a detailed case study of a macrospicule, utilising a wide range of available imagers. The case study involves a jet-like feature that is seen at the solar limb in Crisp Imaging Spectropolarimeter at the Swedish Solar Telescope, AIA/SDO and the Extreme Ultra Violet Imager on STEREO (Solar Terrestrial Earth RElations Observatory). Applying a Markov Chain Monte Carlo method we analyse the spectroscopic data from CRISP and build a profile of the line of sight velocities of the jet. Lastly, we attempt to determine whether or not the jets have an effect on the atmosphere above it.



# Table of contents

<b>Table of contents</b>	<b>ix</b>
<b>1 Introduction</b>	<b>1</b>
1.1 The Sun . . . . .	1
1.1.1 From core to photosphere . . . . .	1
1.1.2 The solar atmosphere . . . . .	6
1.1.3 Observations . . . . .	12
1.1.4 Technology . . . . .	20
1.2 Plasma behaviour . . . . .	27
1.2.1 Magnetohydrodynamics . . . . .	29
1.2.2 Reconnection . . . . .	33
<b>2 Jets and Macrospicules</b>	<b>37</b>
2.1 The ejecta zoo . . . . .	37
2.1.1 Spicules . . . . .	37
2.1.2 X-ray Jets . . . . .	40
2.1.3 Coronal Jets . . . . .	43
2.2 Macrospicules . . . . .	46
<b>3 On the Statistics of Macrospicules</b>	<b>51</b>
3.1 Introduction . . . . .	51
3.2 Observations . . . . .	52
3.3 Results and Discussions . . . . .	54
3.3.1 General Properties . . . . .	54
3.3.2 Inclination . . . . .	56
3.3.3 Relation between macrospicule properties . . . . .	56
3.3.4 How the macrospicule general properties change over the sample period . . . . .	58
3.3.5 Ballistics . . . . .	59
3.3.6 Energetics and scale-height . . . . .	63

3.4 Conclusion . . . . .	64
<b>4 On relationships with an active longitude</b>	<b>69</b>
4.1 Introduction . . . . .	69
4.2 Observations and Databases . . . . .	70
4.3 Statistical Study of the Latitudinal Distribution of MS . . . . .	70
4.4 Statistical study of longitudinal distribution of MS . . . . .	72
4.4.1 Activity maps of active longitudes based on sunspots . . . . .	72
4.4.2 Relationship between the AL and MS longitudinal distribution .	73
4.5 Summary . . . . .	74
<b>5 A detailed case study of a jet-like feature at the limb</b>	<b>75</b>
5.1 Introduction . . . . .	75
5.2 Observations . . . . .	77
5.3 Time-Distance Evolution . . . . .	79
5.3.1 Onset . . . . .	79
5.3.2 Evolution . . . . .	79
5.3.3 STEREO-A . . . . .	81
5.4 Doppler shift . . . . .	82
5.4.1 MCMC Method . . . . .	83
5.4.2 Analysis . . . . .	83
5.5 Effect on the atmosphere . . . . .	87
5.6 Discussion & Conclusion . . . . .	88
<b>6 Conclusions</b>	<b>91</b>
<b>References</b>	<b>95</b>

# Chapter 1

## Introduction

### 1.1 The Sun

The Sun is an extremely complex ball of plasma, the formation of which generated the collection of planets and asteroids we call the solar system. As such, the study of our nearest star should be at the forefront of our research into the cosmos; any model we build to examine other stars must first accurately describe our star. The Sun takes its place on the Hertzsprung-Russell [Hertzsprung \(1909\)](#) [Russell \(1914\)](#) diagram as an early life main sequence star at the yellow end of the stellar spectrum. It is a population 3 star, meaning that it has a high metallic content, a fact which aids in our observations immeasurably.

#### 1.1.1 From core to photosphere

The sun is approximately  $6.96 \times 10^8$  m in diameter and has an average density of  $1.4 \text{ gcm}^{-3}$ , approximately 40% more than the density of water and constitutes 98% of the mass within our solar system.

The structure of the Sun can be divided into internal and external regions. Internal structure has been inferred by the use of techniques such as seismology, therefore we still have many questions as to the exact mechanisms dominating below the photosphere. These examinations have revealed a stratified structure, and the centre of which is the fusion core. Currently, the fusion process is converting 2 Hydrogen atoms to 1 Deuteron, positron and neutrino; this Deuteron then reacts with another proton to form  ${}^3\text{He}$  and a gamma particle, and lastly two  ${}^3\text{He}$  combine to form  ${}^4\text{He}$  and two protons, known as the proton-proton chain as demonstrated in [Bethe \(1939\)](#). These radiation processes require extremely high pressure and temperature in order to overcome the binding energy of the atoms taking part in

the process. The conditions needed for this fusion process are generated by gravitational pressure exerted by the rest of the star which inherently increases the temperature in accordance with the ideal gas law [Larson \(2003\)](#).

The radiative zone is appropriately named, in that, the excess energy generated in the core radiates through this section. It has been estimated that a photon emitted in the core takes on average 100,000 years to move through the radiative zone as a result of the random walk, a process by which a photon is emitted and absorbed repeatedly.

The tachocline, as discussed in [Brun \(2001\)](#), is a thin layer between the radiative zone and the convection zone, of which not a great deal is known. A particular impact of the tachocline's existence, is that the *p-mode* oscillations used in helioseismology, interact strongly with it, as demonstrated in [Chaplin \(2014\)](#), to the point of filtering high order oscillations out. There have been recent studies, such as [Obridko and Shelting \(2007\)](#) which suggest that the tachocline is responsible for several 1.3 to 3 year cycles in feature observed higher in the solar atmosphere, however this has not been definitively proven. It has also been proposed as the source for a dynamo generating the magnetic field. The most important result of the tachocline is that at this point, the motion changes from uniform behaviour of the radiation zone to the differential rotation of the convective zone. This differential rotation is the cause of much of the complexity inherent in the solar body.

Beyond the tachocline, radiative heat transport ceases to be as effective, and as such, convection becomes the primary form of energy transport, thus, this region is named the convection zone. A result of this lower temperature is a transformation in the bulk motion and overall behaviour of the plasma. Within the radiative zone the plasma is approximately 5 MK and is consequently fully ionised, however with the decrease in temperature, comes a transition in the behaviour of the plasma, density drops, and the heavier elements are now not ionised.

The process by which convection takes place is cellular in nature, hot plasma rising and cool plasma falling back through the solar interior. The condition which must be fulfilled by a fluid element in order to begin a convecting behaviour is named the Schwarzschild criteria [Schwarzschild \(1958\)](#). This criteria describes the motion of a fluid element upon being perturbed by external forces, the element is then referred to as being stable or unstable against convection. If the element is perturbed and the resulting buoyancy force causes movement upwards or downwards in accordance with the density of the feature *i.e.* if it is less dense, causing motion upwards, or more dense causing the element to sink for a given constant pressure.

The cellular nature onset is a result of the less dense fluid element rising until it becomes hotter than its surroundings and expands, leading to a cooling phase

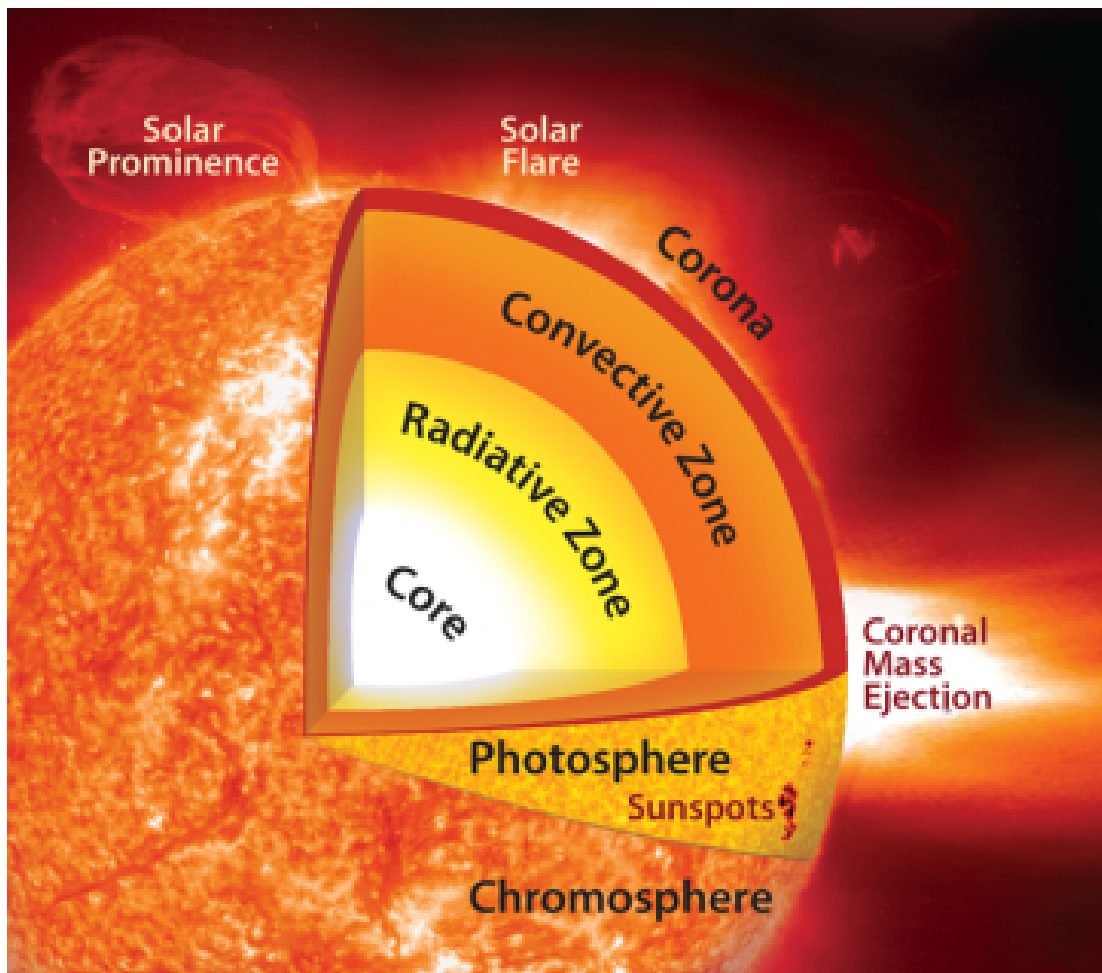


Fig. 1.1 Cartoon of the solar structure as a cutaway. The ‘atmosphere’ nominally begins at the photosphere. Image Credit: Katherine Cantner, AGI

as is to be expected from the ideal gas laws. The plasma then cools, and a perturbation from an external force will cause the plasma to fall back through the convection zone; a result of it now being cool and therefore denser than its surroundings. This can be expressed simply by stating that when the temperature gradient is greater than the adiabatic gradient, then the onset of convection can begin Hansen et al. (2004). Clearly, there will be a set of environmental factors which will lead to the above condition being fulfilled. When the gas is completely ionised, the adiabatic gradient will be constant and convection, unimportant. In order to completely ionise a gas, a relatively high temperature must be attained, therefore let us consider the case for Hydrogen, the dominant element in nearly all stars. At the temperature of 10,000 K, Hydrogen will be totally ionised and convection will not occur, however, less than this and an adiabatic gradient will become apparent. The pressure gradient will also impact the onset of the convection, if the scale height is greater, the higher the fluid element will have to travel before it expands and cools. In reality, when applied to the solar interior, these conditions are fulfilled when the temperature drops to 2,000,000 K, this is due to the non ideal state and not all the atoms and molecules are Hydrogen. As a result we get the transition from radiation zone to convection zone.

The photosphere is the layer of the Sun which we can observe with the naked eye when used in conjunction with appropriate instrumentation, such as a camera obscura. The photosphere is so called, because this layer emits light in the visible spectrum, and has a temperature range of 6000 K at the base, and 4700 K at the top. From a distance, the photosphere appears to be a smooth sphere, however upon closer inspection we observe granulation, as a result of the convection zone, is ubiquitous throughout the layer, excepting regions of high magnetic complexity, such as sunspots or pores. Granulation, Figure 1.2, appears as dark lines and bright 'bubbles' expanding and collapsing as hot material rises, cools and consequently falls back down into the solar interior, Åke Nordlund et al. (2009) . These features tend to measure approximately 2 Mm from one boundary to the other, which, are known as inter-granular lanes. When granules bulk motion is observed , it becomes apparent that they group into larger, super-granules, where the overall motion of the granules radiates away from a central point until they fade at a point where they meet similar granules from another super-granule.

The most prominent feature in the photosphere are sunspots, these are widely documented, observed by early Chinese astronomers were able to view them through thin cloud. These features are significantly cooler than the surrounding photosphere, with a dark centre, known as the umbra, through which open magnetic field emerges from the solar interior. Spreading away from the umbra is the penumbra, a ring

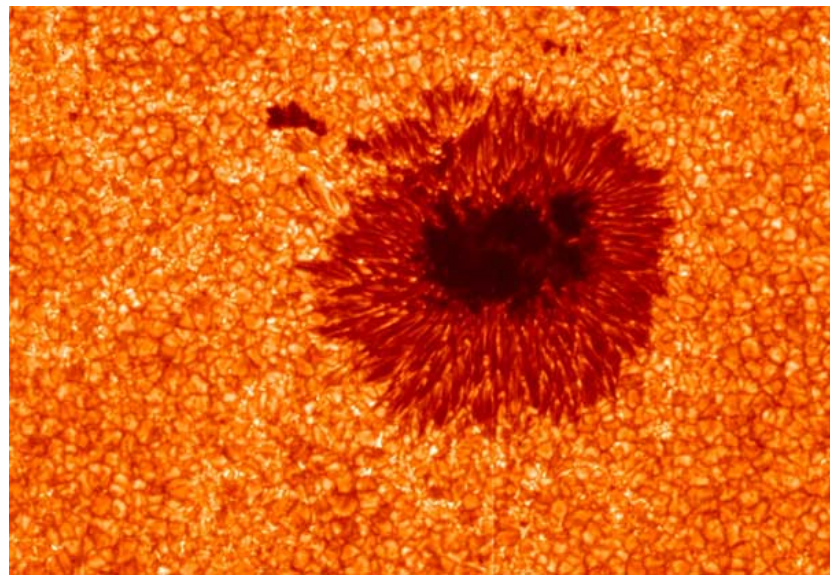


Fig. 1.2 An image of the photosphere featuring its most prominent structures. The sunspot is comprised of the Umbra, dark plasma at the centre, and Penumbra, the thin structures leading away from the Umbra. It is through the Umbra that the magnetic field emerges, causing a lowering of temperature, hence its dark appearance. The rest of the image is dominated by granulation. See the tops of the cells as bright plasma surrounded by the darker, cooler, intergranular lanes  
<https://www.aps.org/units/dfd/pressroom/papers/sun.cfm>

of long thin structures spreading away from the umbra. These have been widely studied and have become known as fibrils. The reason these are so widely studied, is that it has become clear that waves travel up these features from the solar interior. Sunspots are normally part of an extremely complex system of magnetic field, meaning that there are usually many in one active region. It is not yet clear the exact mechanism by which sunspots are formed, however the favoured hypothesis is that of flux rope emergence. In this model a 'rope' of magnetic field is forced up through the convection zone and the photosphere carrying plasma frozen into the magnetic field lines with them. As a result of this formation mechanism, active regions have regions of both negative and positive polarity. In some cases, Sunspots are observed to rotate as they track across the solar surface. In such situations they are observed rotating, the rotation is away from the equator, while at the same time they migrate to the equator in accordance the magnetic configuration between the poles, [Dezsö et al. \(1968\)](#).

### 1.1.2 The solar atmosphere

The first observations of the chromosphere were made during total solar eclipses. When the Moon entirely covered the solar disk *i.e.* the photosphere, apparent at the solar limb were colourful streamers radiating from the solar centre. The density drops sharply from the photosphere to the order of  $10^{-4}$  and is approximately 2 Mm thick. Over this 2 Mm layer the temperature rises from 4000 K to 25,000 K, see *e.g.* [Withbroe and Noyes \(1977\)](#). This result is currently one of the primary focuses of the solar research community. The chromosphere is incredibly complex in terms of its magnetic structure and the transport of heat, consequently the chromosphere plays an essential role in the formation of explosive events such as solar flares and coronal mass ejections (CMEs).

It is in the chromosphere, and subsequently the corona, where we now see the magnetic fields which are rooted in the sunspots we observe in the photosphere, demonstrated in [Athay and Beckers \(1976\)](#). These appear as large-scale loops of plasma which has been locked into the magnetic field lines, extending through this region and right into the corona, they regularly reach 10's of Mm into the atmosphere. Lower in the chromosphere, we find a second, smaller-scale population of loops, and are a few Mm across on average. Small-scale chromospheric loops have been presented as a possible link between the photosphere and the chromosphere, due to their most likely formation being a small-scale flux emergence event [Ulm-schneider and Stein \(1982\)](#).

Examining any image of the chromosphere, it is almost impossible to miss the fabled ‘forest of spicules’. Spicules are small, short-lived, explosive events with origins in the chromosphere which extend through the transition region and into the corona, [Beckers \(1972\)](#). They are ubiquitous in the chromosphere, their number density being of the order of  $10^5$  at any given time, however, their spatial distribution is not uniform. They are found to form on intergranular lanes, as such there is much debate about how they form. Candidates for the formation mechanism are; magnetic reconnection, *p*-mode driven and plasma drains, although there is no conclusive evidence for any of these drives. Spicules high number density has lead many to propose them as a possible solution to the coronal heating problem, be that through instability or propagation of waves into the atmosphere directly. Recent in depth study has revealed the possibility of two populations of spicules, dubbed, Type-I and Type-II, a concept presented by [de Pontieu et al. \(2007\)](#). Type-I have been defined to be longer lived and less explosive, they are also observed to emerge and have a ballistic motion away from and returning to the Sun. However, Type-II show significantly more explosive velocities, up to 150 km/s recorded during their initial

formation, however, they are not observed to return and lifetimes are not expected to exceed 5 mins. However, scientific consensus has yet to be reached, [Zhang et al. \(2012\)](#) do not find any separation in population, more on which in Chapter 2.

Particularly noticeable in the chromosphere is the appearance of coronal holes, a review of which can be found in [Cranmer \(2009\)](#). These appear as regions of dark amongst the bright chromospheric features, this is a result of the cool plasma, lower in the atmosphere becoming visible through these holes. During the minimum phase of the solar cycle, there are usually two prominent coronal holes at the solar poles. These can cover half of the solar disk during particularly inactive solar minima, however, at solar maxima, these polar coronal holes disappear as the magnetic field becomes increasingly complex. The coronal holes are characterised by magnetic field lines extending up though the solar atmosphere, whereas, in the quiet Sun (areas not coronal holes) the magnetic field lines are closed, generally forming small and large scale loops.

This magnetic field configuration of open field lines at the poles and profound non-uniformity between is a result of the differential rotation above the tachocline. Due to faster angular velocities at the equator than at the poles, magnetic field lines which would be straight, pole to pole, are warped in accordance with the frozen in condition. Eventually, the magnetic field between  $60^\circ$  and  $-60^\circ$  forms into approximate bands of alternating opposing polarity magnetic field. The mechanism by which this structure forms, results in converging bands, *i.e.* a sideways 'V' symmetrical around the equator. This can act as a guide for other solar features, such as sunspots, pushing them towards the solar equator from either side.

A demonstration of this complex magnetic field, is the network bright point [Muller and Roudier \(1992\)](#). They are caused by the squeezing of granules and resulting fluz compression. Theses are prevalent throughout the solar atmosphere, we observe them in the photosphere and corona, however, they are primarily chromospheric features. They are thought to be regions of very high magnetic pressure, causing lower gas pressure and therefore an increase in temperature.

There are several large-scale features with their roots in the photosphere. Filaments, reviewed in [Engvold \(2004\)](#), and their off limb counterparts prominences, stand out spectacularly when observing in  $\text{H}\alpha$ . Filaments are observed as dark strands of plasma, having risen from the cool photosphere against the hotter chromosphere, that can extend far across the solar disk and have lifetimes of many months. Prominences are the same features observed over the limb, and hence appear as bright features against the dark sky. This allows us to observe the impact on the atmosphere more closely. [Kawaguchi \(1970\)](#) observe the plasma falling away from the main body of the prominence, becoming known as coronal rain. The effect this

rain has on the atmosphere is not yet fully understood, but there has been discussion as to its merits in terms of possible heating or cooling effects.

At the top of the chromosphere, the temperature of the plasma increases rapidly over a very short distance, approximately 500 km. This is known at the transition region, [Mariska \(1986\)](#). It acts as a barrier, and amplifier, between the chromosphere and corona with the temperature rising from 25,000 K to 1 MK. The mechanism which causes this is still not understood and is one of the prominent problems in solar physics.

Above the transition region we find the corona, [Golub and Pasachoff \(2009\)](#), high temperature plasma whose behaviour is now dominated by the magnetic field which has emerged from the solar interior. Iron is plentiful, which, we can tell is ionised from observations, and such the temperature has a minimum value of  $1 \times 10^6$  K. The corona is a complex system where exceptionally large scale features can have far reaching effects on the solar environment, [Reale \(2014\)](#). Here, we observe very large scale structures such as coronal loops and streamers, as well as transient explosive events such as solar flares and CME's, regularly in the same event. Streamers are self-descriptive flows of plasma moving radially away from the solar disk. They are particularly prevalent above the coronal holes and over magnetic features, such as loops. The resulting plasma from these streamers, goes on to contribute to the solar wind. Coronal loops, CME's and solar flares are tightly related. As the footpoints of the coronal loops, sunspots rotate and migrate towards the equator. The magnetic tension of the loop increases to the point at which a reconnection event is the only way of reducing the magnetic energy in the system. Solar flares are caused by large-scale magnetic reconnection events. The material in the overlying loops becomes unbound as a result of the release of magnetic tension, and is released in the form of a CME, although this is not always the case.

The above model applies more to solar flares which are observed low in the corona and chromosphere. There is a separate model in which the reconnection occurs much higher in the corona. There is a standard model for the formation of solar flares, [Brown and Smith \(1980\)](#). The models' initial condition involves an arcade of coronal loops, with open magnetic field lines forming a streamer around the outside. At the top of the coronal loop, a region of cool, dense plasma forms, however, it remains suspended by the magnetic field. Eventually the system will reach a non-equilibrium state and the filament will be ejected outwards from the loop system. The resulting elongation of the magnetic field eventually leads to the field lines, previously on opposite sides of the loop, becoming close enough that magnetic force brings them together. This effectively severs the anchor holding the plasma filament in place, releasing it into the high corona and solar wind. This

release of energy also has the effect of accelerating particles down the underlying coronal arcade, causing heating and brightening. The nature of these events is sufficient to cause bursts in the electromagnetic spectrum. This is the phenomena that has been named the solar flare, a classification of which is presented initially by [Bai and Sturrock \(1989\)](#), and NOAA classify in terms of classes, B, C, M and X, with X being the highest energy ( $\text{Wm}^{-2}$ ) and B being the lowest and 9 subdivisions within each class.

The remaining ejected material then either falls back to the solar surface or carries on to form a coronal mass ejection (CME). These are very large scale features in the corona, both spatially and temporally, reviewed in, *e.g.* [Chen \(2011\)](#). They propagate through the corona, into the solar wind and beyond Earth. They are categorised (in the LASCO database) based upon the appearance, Halo, partial halo and complete. This is based on the difference with respect to the Earth/viewing position. A CME which is directed at Earth will appear as a halo around the Sun. Viewed from the side, we see the fine structure of the CME, prevalent is the leading edge, at the fore of the propagating feature beneath which is a void. [Manchester et al. \(2005\)](#) show this leading edge regularly forms a shock, and particles already in the solar wind can be accelerated. The centre of the CME is generally the core, comprising of the filament that has just detached from the solar surface. They are inherently imbued with the magnetic field that originated in the solar atmosphere. As this magnetic field propagates through the solar wind, a shock is thought to form at the bow of the feature. These shocks may also excite heavy ions in the solar wind causing turbulence and heating.

When the coronal material, bulk motion becomes radial, it is defined to be the solar wind. At this point the plasma is dominated by the magnetic field and may be considered collisionless *i.e.* the distance between the ions is greater than the mean free path. Due to the Parker spiral, [Owens and Forsyth \(2013\)](#), the magnetic field is perpendicular to the bulk velocity of the plasma, the solar wind is not, however, uniform. The structure is divided into two modes, fast and slow solar wind. The difference between the two modes was highlighted by the readings taken by the Ulysses mission, while in a slingshot polar orbit around Jupiter and the Sun. The SWOOPS instrument on-board, measured the velocities of ions in the solar wind and found that the distribution is non uniform. Above the poles, the plasma reaches velocities up to  $800 \text{ km s}^{-1}$  whereas, around the quiet Sun regions we find a lower range,  $300 - 400 \text{ km s}^{-1}$  [McComas et al. \(2003\)](#).

With such an energetic feature extending far into the solar system, how this interacts with the planets is of the utmost importance. Planets such as Mercury and Mars with little or no magnetic field to speak of, are bombarded by the energetic

particles in the solar wind. This is also the case for the Moon, with only small local magnetic fields (no global dynamo) it is directly exposed. The Moon provides the best opportunity to examine such a system. We therefore observe multiple different ways the solar wind interacts with it. [Bhardwaj et al. \(2015\)](#) present a mechanism for proton back scattering off the lunar surface as energetic neutral atoms, revealing roughly 8 - 28% of the particles scattered are Hydrogen. Conversely, we also observe sputtering, however  $\text{He}^{++}$  atoms are much better sputtering agents than  $\text{H}^+$ , so were we to mine the lunar surface, we might find significant resources of this element. As such, the Sun's relationship with these, generally, rockier, less well 'protected' planets and solar system bodies is always going to result in direct contact between the solar surface and the surface.

The alternative is clearly planetary bodies which produce a global magnetic field. In the case of the Earth, the magnetic field dynamo is the convecting cells of the molten magma core, whereas, in the case of the gas giants, the extremely high density causes the hydrogen to be in a metallic form and convecting cells of hydrogen are believed to be the initiator of Jupiters magnetic field, [Kutner \(2003\)](#).

In this case, we observe an extremely complex structure and system. The solar wind approaches with the magnetic field perpendicular to the orbital plane and the Earths' magnetic field in an approximate dipole state. Therefore, we have a case where two vertical magnetic fields meet. This leads to an increase in the magnetic field strength, ion density and potential, this feature is known as the bow shock, this system is comprehensively reviewed in [Wilkinson \(2003\)](#). All the elements of the solar wind that interact with the bow shock will be affected in some way. Ions and particles backstream off the bow shock, [Fredricks \(1975\)](#), reflected by the potential barrier formed by the increase in magnetic field strength, and the solar wind magnetic field wraps around that of the Earth. Behind the bow shock we find the magneto sheath, a magnetically turbulent region comprising the material that has managed to pass through the bow shock. The density of particles and the magnetic pressure decreases over the magnetosheath until the pressure from this region is balanced by the Earths magnetic pressure, whereby, the magnetopause is formed.

Given that this region of the Earth's magnetosphere is heavily influenced by the solar wind, the exact structure of it is defined by the state of the solar wind. As such, the fast solar wind will compress this region further as the magnetic pressure will be higher and events such as CME's which increase the particle density, also altering this region significantly.

As the solar wind magnetic field wraps around this region, it will eventually come into contact with the open magnetic field lines at the Earths poles. This leads to a reconnection event, releasing the magnetic tension in the open fields lines and

causing them to be dragged out behind the Earth, forming the magneto tail, and eventually reconnecting with magnetic field which has made the same journey on the opposite side of the Earth. This forms a current sheet roughly in the equatorial plane, however, this will be impacted and changed by the solar wind and geomagnetic events in the same way as the magneto-sheath.

A second result of the open magnetic field lines at the Earth's poles is that particles from the solar wind may interact with, and consequently spiral down these open magnetic field lines. Particles spiralling down a magnetic field line are accelerating and, therefore, have excess energy which is dissipated as electromagnetic radiation. This manifests as the phenomenon known as the Aurora, observed at high magnitude latitudes, appearing as a ring of light when viewed from space. Hence, when the Earth is bombarded by geomagnetic storms created by flaring and CME type events, we see warping of the bowshock/magnetopause system and increased appearance of Aurora over a wider range of latitudes, [Baker \(1995\)](#).

The question becomes, is the magnetospheric model we observe at Earth, applicable to the gas giants? The answer appears to be yes, firstly, we observe Aurora on the poles of both Jupiter and Saturn, strongly implying a similar dipole magnetospheric structure with open field lines over the poles. Differentiating the two systems is the massive size of Jupiter's magnetic field, 20,000 times larger than that of Earths and extending 100 times further. This significantly larger extent is, in part, due to the reduced pressure from the solar wind, allowing the magnetosphere to expand more significantly, but also attributed to the more powerful dynamo (sufficiently strong, that the Van Allen belts that are toroidal at Earth are flattened out by Jupiters magnetic field).

The Sun's influence ends with the termination shock. At this point the outward solar wind pressure is finally in balance with the pressure of the interstellar medium. The result is that the solar wind suddenly decelerates, causing a shock to form, it has been proposed recently that Voyager 2 has made it across this boundary becoming the first man made object to leave the solar system. The region between the solar system and the inter stellar medium draws parallels with that between the solar wind and our magnetosphere. There is a bow shock due to the Sun's progress around the galactic disk, a heliosheath and heliopause, all of which have proxies in the Sun-Earth interaction.

For all of these reasons, it is clear that the study of the Sun, its local environment and the explosive events are essential to our continued existence. Geomagnetic storms have previously knocked out power lines and will affect the operations of satellites in orbit, consequently, predicting and understanding these explosive events is essential.

### 1.1.3 Observations

#### History

Mankind has been fascinated with the Sun for as long as we have been sentient, which is understandable given that it dictated seasons, whether crops grew and was a giant burning orb in the sky. As such, in early civilisations it was regularly worshipped as a god. Early Mesopotamian cultures worshipped Shamash, Rah was the Sun god of the Egyptians and Amaterasu is the Shinto goddess. Around these gods, mythologies were built; the Egyptian solar chariot, carrying the Sun across the sky, battled demons overnight to rise again on the other side; in Hinduism, the Sun god is named Surya and is driven across the sky in a seven-horsed chariot representing the days of the week. These mythos speak to the inherent importance of the Sun to civilisation on Earth, however, it was not until the 17<sup>th</sup> century that scientific observations really begin to occur seriously.

Fresh advancements in glasswork and lens technology allowed the development of telescopes and camera obscuras. Utilising the telescope to project the image (as not to look directly at the Sun) observers hand-drew their direct observations of the solar surface. This was clearly the photosphere, due to its emissions being in the visible spectrum. The most prominent feature of the photosphere are the sunspots appearing at the surface; therefore, the early telescopes allowed significant study of this feature.

The work of Johannes Kepler demonstrated that the Sun rotated on its axis and sunspots were first observed by Harriot and the Fabricius family using a camera obscura. Initially there was debate as to what these dark features were - one hypothesis was that these were shadows of planetary bodies inside Mercurys orbit, however, Galileo demonstrated that their origin must lie on the surface of the Sun.

Given the formative solar observation technology, this is where solar studies stayed for a very long time, a fact not aided by the period now termed the Maunder minimum (named for English astronomer Edward Maunder who presented this hypothesis). This period lasted between 1675 and 1715, during which time the sunspot count almost entirely diminished. During this minimum, the Earth's climate went in to what has become to be known as a 'Little Ice Age', where global temperatures lowered to a point where rivers, that were usually clear of ice, would freeze over to the point they could be reliably walked upon.

Study of the Sun took a large step forward when observatories such as the Royal Greenwich Observatory began taking measurements in 1874. Now with consistent imaging from the same source and a history of smaller observations combined, larger patterns within sunspots was revealed. Taking a monthly average of the sunspot

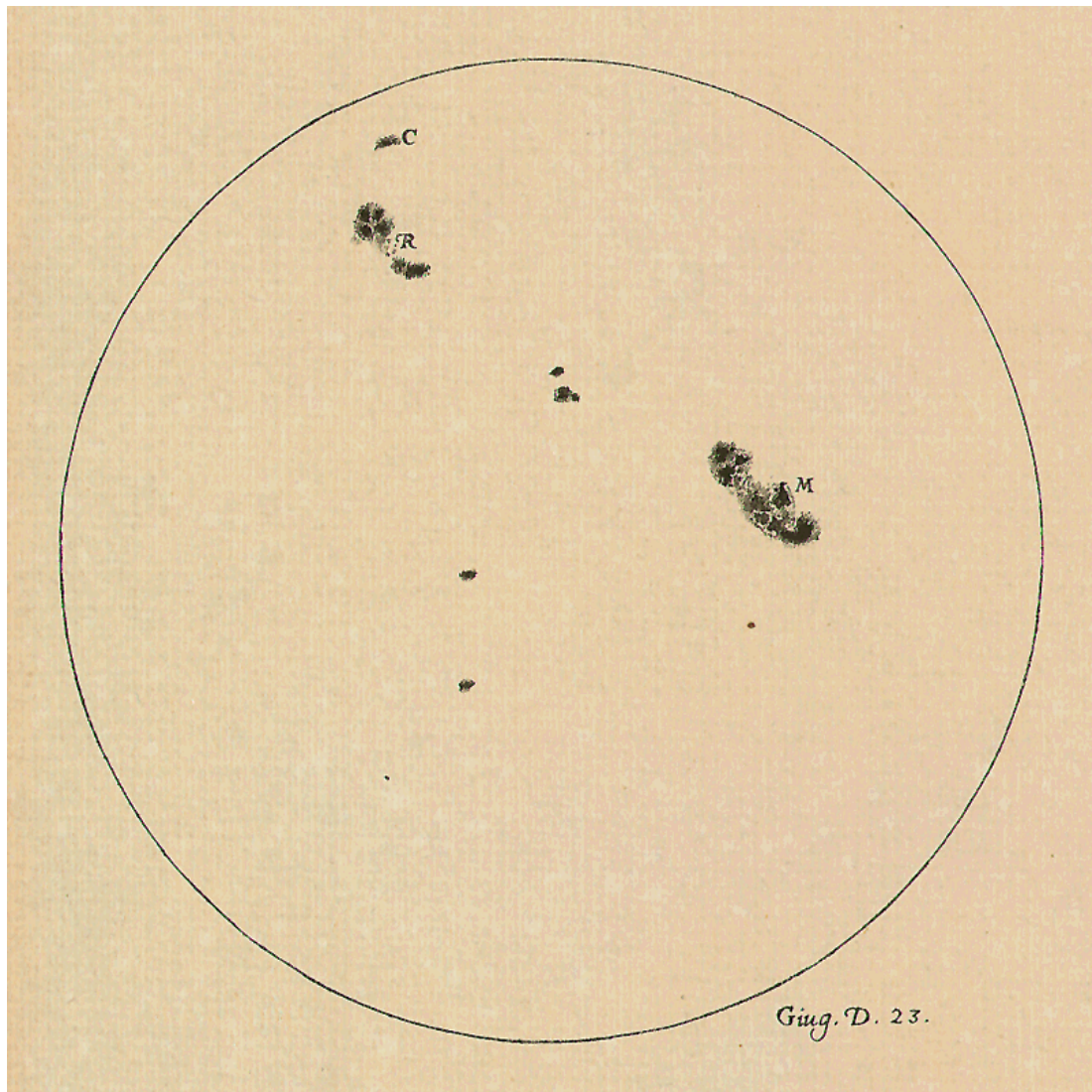


Fig. 1.3 Galileo's catalogue of hand drawn images of the solar photosphere, is one of the best examples of early solar observations. Something we take for granted in modern solar observational techniques, is that we now have routines to correct the solar orientation. Due to the nature of the observations, Galileo and his contemporaries' records, the drawing will always demonstrate the 'angle' resultant of their observing position.

count revealed a rise and fall in the sunspot number count over an 11 period, now referred to as the solar 11-year cycle. Sunspot numbers in modern times are calculated by the number of sunspot groups multiplied by 10 as that is the average number of sunspots in a sunspot group. This definition is utilised by the National Oceanic and Atmospheric Administration (NOAA) in America and Solar Influences Data Analysis Centre in Belgium (SIDC) in Belgium. Both of these organisations monitor the Sun and its impact on Earth including radio flux and total solar irradiance. All of these can be used as a proxy to demonstrate the 11-year solar cycle.

If we plot the date of the sunspots occurrence with respect to their latitude, we produce another diagram demonstrating the 11-year cycle. This is the now famous butterfly diagram 1.4, in which populations of sunspots tend to form closer and closer to the equator before a break point at which they begin forming further away, the time scale of which is 11 years.

This is a result of the previously discussed differential rotation mechanism in action in the Sun's motion. As the magnetic field becomes increasingly complex and the bands of magnetic polarity grow closer, increasingly more sunspots are pushed to the solar equator. This demonstrates that the 11-year cycle is result of the magnetic field and dynamo. However, this is not the full picture. As a result of the ever increasing complexity of the magnetic field the poles eventually flip. It is at this point that the butterfly diagram moves from a narrow range of latitudes to a significantly wider one, therefore, the 11-year cycle is actually two halves of a 22-year cycle in which the magnetic field flips and then returns to its initial configuration.

## Spectroscopy

Newton was the first to observe that light from the Sun could be divided into its component parts using a simple prism, but it was a very long time before we would reach a point where this information could be used for science. In 1802, approximately 100 years after Newton's initial observation, William Wollaston observed the dark lines in the solar spectrum. His results were published in a paper in which he tested the limits of compound refraction when prisms are used with water, sulphuric acid, crystalline lens of an ox, human cuticle, beeswax (from an island where there were no bees, however, when compared to beeswax, was similar) and other such everyday substances. He let a beam of sunlight enter a dark room and become incident upon a prism of flint glass. He records that he observes two dark lines in green and blue, which, he notes 'in an imperfect experiment, might be mistaken for the boundary of these colours'.

Joseph von Fraunhofer investigated these lines even further using multiple prisms,

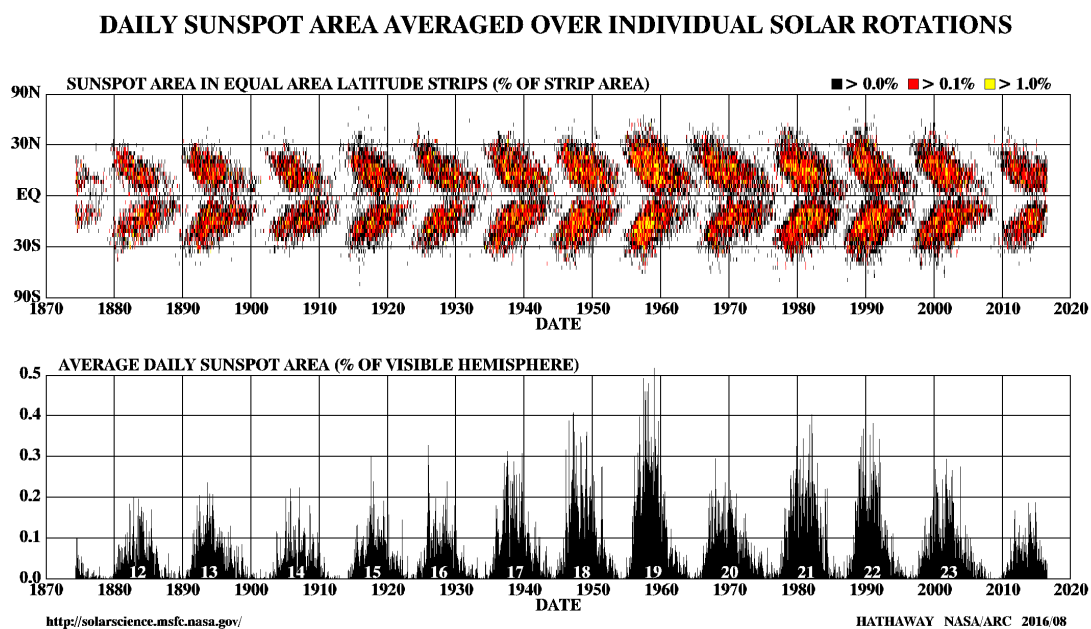


Fig. 1.4 Plotting the latitude of the Sunspot against the time of its appearance is plotted above. It reveals the now characteristic butterfly shape as the Sunspots migrate to the equator over the solar cycle, as shown on the bottom. The area of sunspots as a percentage of the solar surface against the time at which it formed. It conveniently demonstrates the 11 year solar cycle. <http://solarscience.msfc.nasa.gov/SunspotCycle.shtml>

enabling him to produce much higher refractive indices. He proceeded to measure and document all of the dark lines he could find (over 570) and designated the stronger lines A-K and weaker lines the rest of the alphabet. Of course, due to the limitations of technology at the time, these lines are all in the visible spectrum and hence the wavelength range of 300 – 900 nm.

These lines are dark because they are absorption lines. They are a result of the quantum mechanical effects of the electron energy shells around atoms and molecules. In the case of the Sun, a continuous spectrum is radiated from the photosphere and this light then interacts with the elements higher up in the atmosphere. Upon collision with an atom or molecule, the exact wavelength of light which corresponds to the energy required to excite an electron from one energy level to another is absorbed by that electron. The direct result of this is that the wavelength absorbed in the energy transaction is absent from the white-light spectrum being emitted from the photosphere, and hence appears as a dark line when observed from beyond the solar atmosphere.

The field progressed and we began to fully understand the elements and electron transitions responsible for these absorption lines. One of the most famous examples of these is the Balmer series, named for the man himself, Johann Balmer. This series is a set of 4 transitions to or from energy level  $n = 2$ , as can be seen in [1.6](#).

The transition from  $n = 3$  to  $n = 2$  is termed Hydrogen alpha ( $H\alpha$ ),  $n = 4$  to  $n = 2$ , Hydrogen beta and so on for  $n = 5$  and  $n = 6$ , gamma and delta respectively. However, while the concept of a simple 1-1, such as the above transition is clear, this does not always bear out in reality. There can be environmental effects, such as temperature or magnetic field affecting the states of the energy level, which can cause alteration of the wavelength of light emitted from the decay of the electron. For instance, Hydrogen alpha is extremely useful for solar observations due to the high abundance of the atom in the atmosphere. However, due to external factors influencing the energy levels, when we observe Hydrogen alpha, the deviation from the theoretical transition is sufficient to broaden the line to include both the upper photosphere and lower chromosphere. Of course, Hydrogen does not just have transitions to the  $n = 2$ , there are series associated with;  $n = 1$ , Lyman,  $n = 3$ , Paschen, Brackett details transitions to  $n = 4$  and Pfund,  $n = 5$ .

Clearly this methodology can be applied to all atoms and molecules that are in the solar atmosphere, allowing us to create a larger picture of the structure of the atmosphere. We can do this by abundance and position, *i.e.* there appears to be large amounts of a given transition line emission in this region and forming a structure by inspection of an image taken using an appropriate filter. As has already been said, we can associate certain transitions with specific places in the solar atmosphere.  $H\alpha$

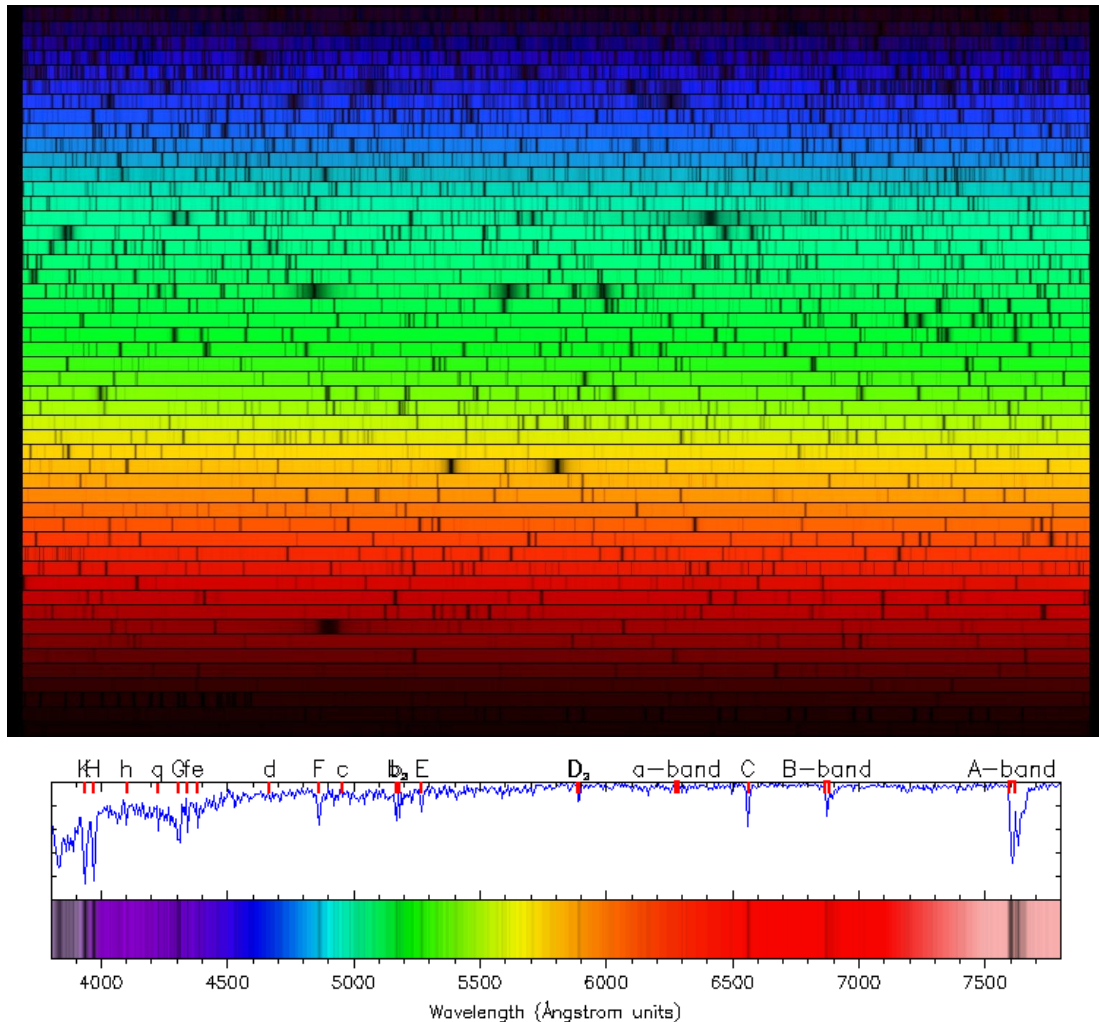


Fig. 1.5 The top figure is a visible light measurement of the Sun. It demonstrates that there are elements in the atmosphere absorb the light and appears on this spectrum as a dark line. The Fraunhofer lines (absorption lines) are marked on a continuous spectrum with an intensity profile below. [http://media.radiosai.org/journals/Vol\\_05/01JAN07/04-musings.htm](http://media.radiosai.org/journals/Vol_05/01JAN07/04-musings.htm)

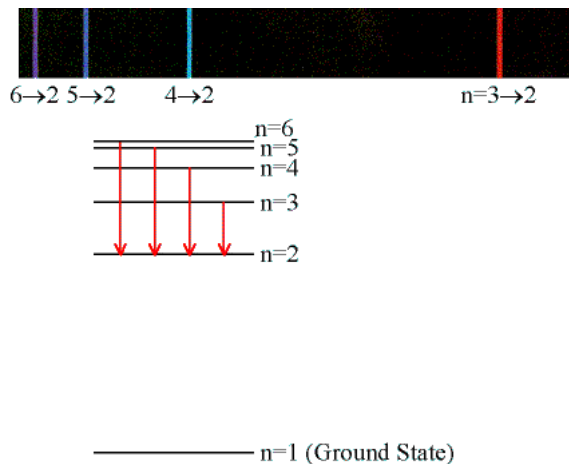


Fig. 1.6 A demonstration of the Balmer lines, transitions in the hydrogen atoms. In this case, specifically transitions between other lines and  $n = 2$ . [http://www.daviddarling.info/encyclopedia/B/Balmer\\_series.html](http://www.daviddarling.info/encyclopedia/B/Balmer_series.html)

has already been discussed. Moving up the atmosphere, we find He II 30.4 emission which is a Balmer- $\alpha$  transition, so  $n = 3$  to  $n = 2$ , and has the same issue as H $\alpha$ , in that it is extremely broad. Calcium II and silicon IV are both emitted in the transition region and are observed by the most recent (at the time of writing) space-borne solar telescope, IRIS, [De Pontieu et al. \(2014\)](#). They are closely associated with the thin transition region, but we do also observe separate features not exclusively within the transition region.

Above the transition region iron is bounteous, and so we have many emissions lines with which to examine the corona due to the high number of available transitions. Fe VIII (13.1 nm), Fe IX (17.1 nm), Fe XII (19.3 nm), Fe XIV (21.1 nm), Fe XVI (33.5 nm) and Fe XVIII (9.4 nm) are all observed by the spacecraft Solar Dynamic Observatory (SDO) with the Atmospheric Imaging Assembly (AIA), [Schmelz et al. \(2013\)](#). As the temperature of the atmosphere increases, the amount of available energy changes and different transitions are excited. The various lines here therefore apply to different temperatures.

The emission lines produced can also be affected by the environmental magnetic field, and as such we can find more out about the state of the plasma via spectroscopy. The effect which allows us to do this is known as the Zeeman effect, whereby the magnetic field causes the energy levels to split based upon the spin of an electron, up or down. This results in a splitting of what would be a single peak, into two, with the separation of the peak dependent of the size of the magnetic field present. Finally, the peak that is produced is very weak, consequently, this is an unsuitable method when applied to the chromosphere and upwards.

A more suitable method by which we analyse the solar magnetic field is Stokes

$$\begin{aligned}
 S_{\text{LHP}} &= I_0 \begin{pmatrix} 1 \\ 1 \\ 0 \\ 0 \end{pmatrix}, & S_{\text{LVP}} &= I_0 \begin{pmatrix} 1 \\ -1 \\ 0 \\ 0 \end{pmatrix}, & S_{\text{L+45P}} &= I_0 \begin{pmatrix} 1 \\ 0 \\ 1 \\ 0 \end{pmatrix}, \\
 S_{\text{L-45P}} &= I_0 \begin{pmatrix} 1 \\ 0 \\ -1 \\ 0 \end{pmatrix}, & S_{\text{RCP}} &= I_0 \begin{pmatrix} 1 \\ 0 \\ 0 \\ 1 \end{pmatrix}, & S_{\text{LCP}} &= I_0 \begin{pmatrix} 1 \\ 0 \\ 0 \\ -1 \end{pmatrix},
 \end{aligned}$$

Fig. 1.7 The variations of the polarisation of light by the magnetic field. Q-left to right and up and down. U, Inclined to 45, and V, circularly polarised.  
[https://spie.org/publications/fg05\\_p12-14\\_stokes\\_polarization\\_parameters](https://spie.org/publications/fg05_p12-14_stokes_polarization_parameters). A Fieldguide to Polarisation.

Polarisation Parameters, which describe the degree to which passing through a magnetic field has affected the electromagnetic radiation. With this method, the total intensity of an optical beam is defined to be a sum of three forms of polarisation. These three polarisations and the total are referred to as the polarisation parameters, I, Q, U and V, Figure 1.7. I is raw intensity of the electromagnetic radiation, Q is the linear polarisation horizontally and vertically, U is also linearly polarized however is rotated  $\pm 45^\circ$  from Q and lastly V, which is polarised circularly, both left and right handed. Using a combination of the 4 intensities it is possible to construct a vectorgram of the magnetic field. This is the method used by the SDO instrument Helioseismic and Magnetic Imager (HMI) to examine features on disk. These magnetograms, Figure 1.8 are ineffective at the limb, which is a limitation of the method. This is because a feature at the limb has no background light source to use as an origin to test the result of any polarisation.

The vector magnetograms are used widely when studying active regions, due to the very high magnetic field strength. They can track magnetic flux cancellation which regularly leads to the formation of other features, such as solar flares and CMEs, due to the release of magnetic energy into the corona Welsch (2006).

We also observe the small magnetic bright point and network bright points, observed in the photosphere and chromosphere, respectively, Almeida et al. (2010).

They are an inherent part of what is known as the magnetic network which was visible in original measurements of the solar magnetic field over the boundaries of supergranular cells. The magnetic field emerges from the supergranule boundaries as open magnetic field lines, extending up, into the chromosphere and above (Hasan et al., 2005). Of course, the structure therefore takes roughly the same form as the photospheric observations in G-Band (a Fraunhofer emission line; 43.079 nm), but with bright structures highlighting the supergranular lanes 1.8. As a result, we have open magnetic field lines emerging with a canopy of closed magnetic field between the two boundaries. A structure such as this can be a catalyst for physical processes such as reconnection.

It is within these regions that the magnetic bright points reside. They appear as points of extreme intensities against the cool dark plasma of the intergranular lanes, due to their intense 0.1 T magnetic field strengths. They are demonstrated to drift and move as the granules evolve (Chitta et al., 2012) which has led the community to suggest that these points could diffuse large amounts of heat into the solar atmosphere.

### 1.1.4 Technology

In the current solar observation climate, we have a wealth of information, coming from many different sources. Understanding the functionality of these instruments in terms of the raw method is essential to rigorous science and accurate readings.

#### Charge Coupled Devices (CCD's)

CCDs are essential to current observational techniques and are utilised by almost every single solar mission. CCDs are comprised of individual detectors all of high quantum efficiency arranged in a large grid, each element of which is a single pixel. An individual pixel keeps an electronic record of the photons striking it (summing them to an intensity). Each pixel behaves as a potential well, trapping electrons produced as a result of the photoelectric events with the incoming photons. The charge resulting from the build up of electrons within the well will eventually reach a point at which it exceeds said well. The resultant discharge of the capacitor is passed to the next in the row until it reaches the end of the row, at which point a charge amplifier is used to record a voltage for the row, eventually building up an image.

The particular advantage to a CCD is the one-to-one response to the incoming photons, giving extremely accurate results. With respect to background noise and errors, the CCD is much easier to take regular dark current measurements (taking a

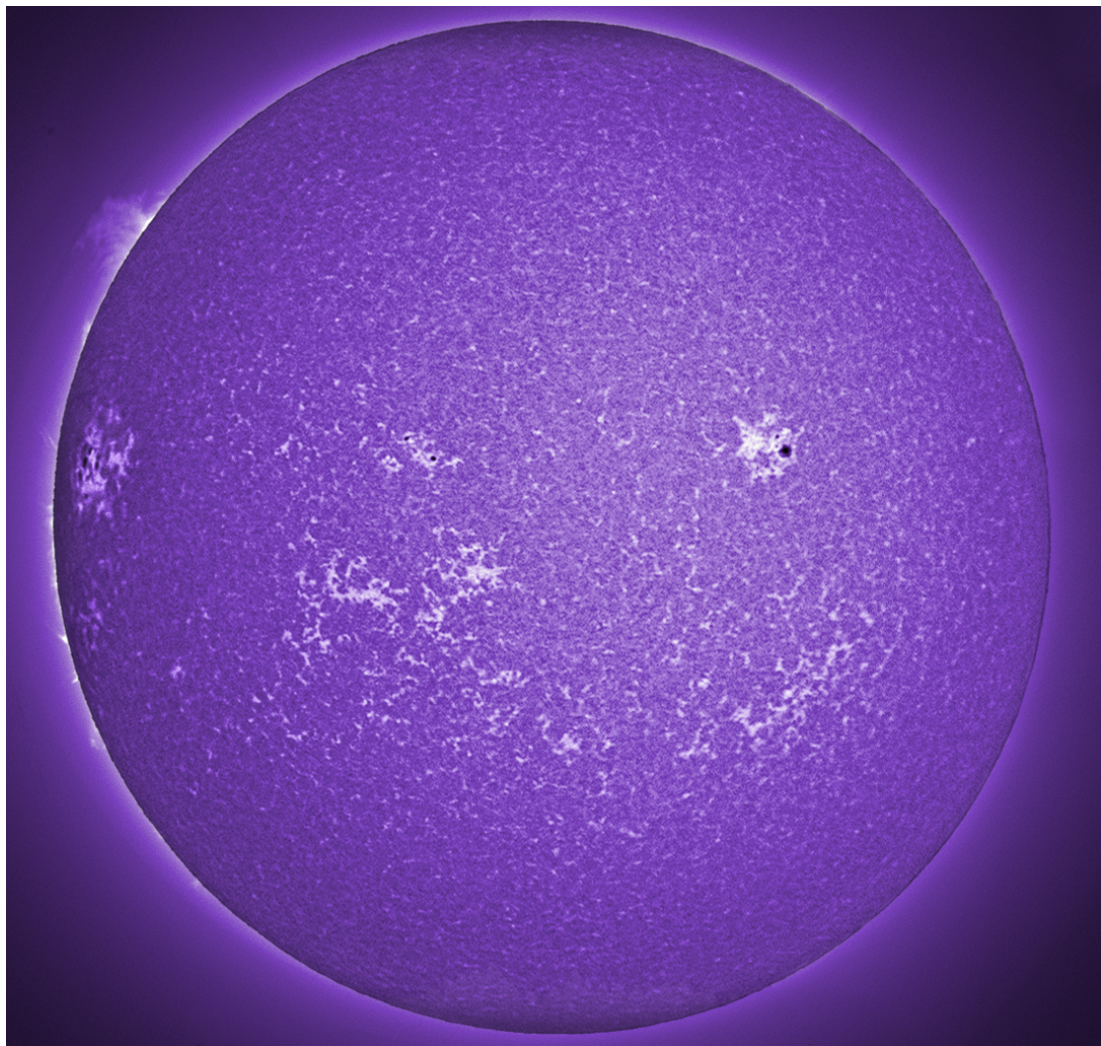


Fig. 1.8 Calcium K filter image of the low solar photosphere. Observe the regions of bright lines highlighting the intergranular lanes where the bright points appear. Clusters of intensity designate active regions where there is significantly more magnetic activity. [http://science.nasa.gov/science-news/science-at-nasa/2008/02oct\\_oblatesun/](http://science.nasa.gov/science-news/science-at-nasa/2008/02oct_oblatesun/)

reading with zero light coming in) and pixel-to-pixel variation is accounted for using flat-fielding (exposing the grid to uniform field). The grid of pixels approach also allows for much more flexibility in analysing data and correcting for the effects of events such as cosmic rays. This is possible due to the ability to read these recordings into a computer.

### **Ground-Based Telescopes**

Solar physics spent its early development being applied in ground-based solar telescopes, as has already been discussed, particularly in centres such as Royal Greenwich Observatory and Meudon Observatory in Paris. In the modern era, the most powerful instruments, delivering high cadence and spatial resolution, are based on the ground. Due to the challenges of observing on the ground, the location of these facilities is carefully chosen, regularly at high altitude, minimising disturbance of the signal by the atmosphere, and away from busy, polluting cities for the same reason. The main advantages of ground based telescopes over space borne, is that the instruments can be heavier and literally more extensive given that they do not need to be transported into space.

On La Palma in the Canary Islands, at 2360 m altitude, the Swedish Solar Telescope is situated. It utilises a 1.0 m mirror in a refracting, vacuum solar telescope. The vacuum is necessary due to the quantity of light the mirror reflects, causing heating which would disrupt the signal being transmitted down to the receiver. The 'receiver' is what has become known as the optical bench; here the light beam is sent to one of several possible processing suites which are easily accessible to structure observations as needed.

The SST has two such pipelines, one for the red end of the electromagnetic spectrum and another examining the blue end. The CRisp Imaging SpectroPolarimeter (CRISP), focuses on the red end of the visible spectrum, whereas the soon to be updated instrument, Chromis, analyses the blue end. The beam is split upon its arrival at the optical bench and sent to either of these instruments, but before the beam reaches CRISP there is a layer of correction known as adaptive optics.

Adaptive optics corrects for atmospheric scintillation, aberration and stabilises image motion. These cumulative effects result in an optical path difference of the light incident with the lens/mirror of the telescope. Given this information, it is crucial to know the atmospheric physics overlying and surrounding the telescope. It is for this reason that observatories such as the Big Bear Solar Observatory ([Cao et al., 2010](#)) in Los Angeles and the proposed new Chinese Giant Solar Telescopes ([Liu et al., 2014](#)) are built on and by lakes, since the temperature will be lower, thus

reducing heat haze, and therefore atmospheric effects. The primary atmospheric parameters influencing the setup of the adaptive optics are the Fried parameter (which measures the quality of optical transmission), the Greenwood frequency (the bandwidth required for optimal correction) and the atmospheric turbulence profile (which allows a calculation of the refractive index of the atmosphere) as shown in [Rimmele and Marino \(2011\)](#).

As a result of the above points, the images from the SST are extremely customisable. They are usually returned as data cubes, the dimensions of which are time, wavelength, x and y. The resolution of these features are therefore changable dependant on the requirements of the observation. Cadence can be as low as 2.5 s, the spectral increment, 0.02 nm, and spatial resolution of 0.12 arcsec. A part of what makes this form of observation viable is the ability to directly download the received signal, which is a limitation of space borne instrumentation. Given the possibilities of ground based observations, the method is popular, with the aforementioned Big Bear Observatory joined by a plethora of other facilities, Richard B. Dunn solar telescope (DST) in New Mexico, Mauna Loa Solar Observatory on Hawii, which will shortly be joined by the Daniel K. Inouye Solar telescope (DKIST). DKIST promises to be the most powerful solar telescope ever created with a 4 m mirror, enabling resolution of 10 km per pixel and overcoming the current quantity of photons issues at the limb for spectropolarimetry.

## Space Based Telescopes

Space bourne telescopes have a significant advantage over their ground based counterparts due to the nearly constant un-interrupted, view of the Sun without the atmospheric effects disturbing the signal. As a result, the volume of space based instrumentation has grown exponentially since the early Skylab missions taking solar images from a low Earth orbit.

The first solar mission to move on from imagers on space stations was the Solar Heliospheric Observatory (SoHO). Placed at the gravitationally stable Lagrange point, L1, between the Sun and Earth, it affords constant viewing of the Sun. It was one of the first missions to comprehensively cover the entire solar environment, the instruments of which are described in [St. Cyr et al. \(1995\)](#). The science covers dopplergrams of the photosphere, EUV imaging of the chromosphere and out to LASCO, monitoring the solar wind.

Following SoHO, the Advanced Composition Explorer (ACE), [Garrard et al. \(1997\)](#), was placed near the L1 point as well. It was launched in 1997 with a much more specific goal of analysing the contents of the solar wind, extremely pertinent as

the constituents and energy inherent in the solar wind can have extensive effects at Earth. As a result of this, the scientific mission of ACE is heavily leant towards instrumentation which physically measures the energy and identity of a given particle. The Solar Wind Ion Mass Spectrometer (SWIMS) and Solar Wind Ion Composition Spectrometer (SWICS), [Gloeckler et al. \(1992\)](#), are used to measure these properties. SWICS was initially built for the ULYSSES [Wenzel et al. \(1992\)](#) mission which orbited the Sun in a novel slingshot orbit around Jupiter, normal to the plane of orbit.

The results this instrument produced provide one of the most iconic sets of readings in the modern era of solar physics. As Ulysses completed its orbit, the radial velocity profile of the solar wind was found to vary over solar latitude, Figure 1.9. At lower latitudes, the solar wind was found to be of the order  $200\text{-}400 \text{ km s}^{-1}$ , before getting to higher latitudes and a distinct transition to much higher velocities. At the time of this first orbit, the Sun was at a solar minimum, consequently there were clear and distinct coronal holes and quiet Sun, matching with the fast and slow wind respectively.

The confirmation of this association between wind mode and magnetic environment came in the next orbit of Ulysses. In this orbit, the Sun was at maximum, therefore, it was almost entirely constituted of quiet Sun magnetic environments. During this orbit, the solar wind was found to be uniformly chaotic , 1.9. Velocities were found to climb as high as those found in a fast solar wind mode, however, it is not the uniformly distributed fast mode emitted from the coronal holes, as evident in the solar minima readings.

Given that we now know that the solar wind and corona have significant reach and influence, a new mission was designed and initiated, the Transition Region and Coronal Explorer (TRACE) [Gaeng \(1998\)](#). As the name suggests, this instrument was designed with the specific intention of investigating the higher reaches of the solar atmosphere. Specifically, the aim of the mission was to investigate the three-dimensional structure of the low plasma beta atmosphere. TRACE is a uniquely designed telescope, following the popular Cassegrain design, in which the primary mirror is divided up into 4 quadrants with separate coatings in order to filter the incoming light. This method allows simple and efficient image co-aligning. Given that TRACE was to observe the high atmosphere, Extreme Ultra Violet lines (with the rest of the EM spectrum filtered at entrance to the detector) were selected for the imaging instruments. These consisted of Fe IX 17.1 nm, Fe XII 19.5 nm and Fe XV 28.4 nm.

The Japanese Aerospace Exploration Agency have organised several solar missions. Solar-A, renamed Yohkoh, [Tsuneta et al. \(1991\)](#) upon its successful launch and commencement of observations, pre-dates SoHO. It covered soft and hard X-Ray

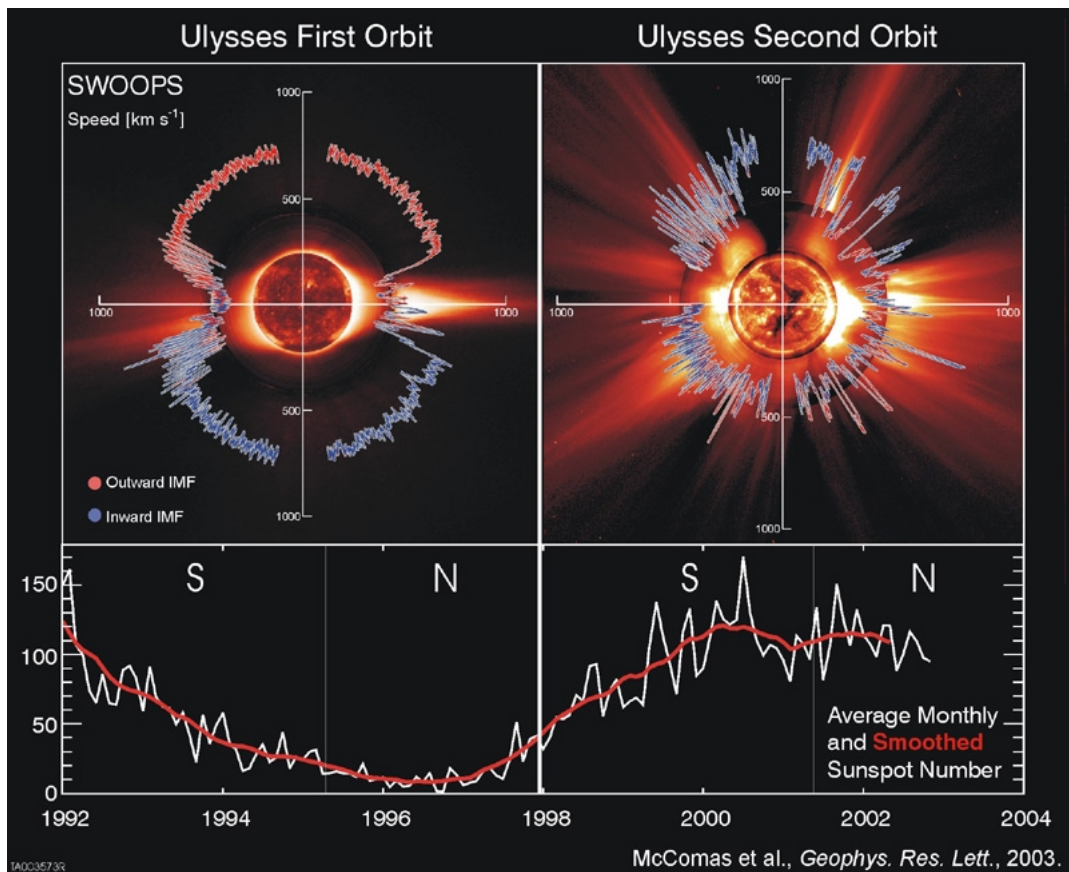


Fig. 1.9 The landmark solar wind measurements. On the left the solar wind during minima. A strictly divided solar wind in which high velocities are detected over the poles and lower values over the more magnetically complex equatorial quiet Sun. On the right, almost homogeneous high velocities at the solar max. This is due to a greater amount of large scale structures, such as streamers and CME's, producing fast solar wind all over the solar atmosphere. [McComas et al. \(2003\)](#)

ranges and spectrometers covering, specifically, the coronal iron lines and a wide band spectrometer. Yohkoh was particularly successful with respect to the detection of high energy events producing large amounts of energy and X-ray emission, such as coronal jets and solar flares. Building on the success of Yohkoh, a new mission was planned, sequentially named Solar-B. It was later renamed Hinode, Sunrise in English, upon its successful launch and is presented in [Kosugi et al. \(2007\)](#).

Hinode's launch in 2007 signified a significant move forward in space based solar observations, building from what was successful in Yohkoh. The mission introduced small wavelength increment spectroscopy to space based missions. The EUV Imaging Spectrometer (EIS) is designed to examine the chromosphere using two specific imaging techniques. It is extremely flexible with 4 slit or slot positions, 1" pixel slit, 2" pixel slit, 40" pixel slot and 266" and two different modes for spectroscopy.

Possibly the most adventurous mission to probe the solar environment to date, is the STEREO mission (Solar TErrestrial RElations Observatory) described in [Kaiser et al. \(2008\)](#). As is suggested by the name of this mission, the primary focus was to form a more comprehensive picture of the solar atmosphere, by positioning two satellites in such an orientation to build a three dimensional picture. Consequently, two identical satellites were launched into orbit, ahead of and behind the Earth. There is an inherent differential in the angular velocity of the spacecraft, in order to move the spacecraft ever further around the orbit at approximately 45° per year. The primary objective of this stage of the mission was to obtain the optimal angle to produce three dimensional images of the Sun using a tomographic technique.

Given that STEREO was designed to give varying angles of the Sun-Earth environment, the instruments on the mission are tailored to this need. SECCHI is a suite of 5 imagers, utilising white-light coronographs, an extreme ultra violet imager and two wide angle Heliospheric Imagers (HI) designed to track CMEs to 1 AU. IMPACT detects solar wind electrons and the in-situ solar wind magnetic field strength and vector, while PLASTIC measures the composition of heavy ions, alpha particles and protons. Given the instrumentation, STEREO is used extensively by space weather forecasters at NOAA, which will increasingly become an essential part of our lives.

STEREO's positioning is advantageous to this work as it affords a different viewing angle on features. This can come in useful when considering features at the limb. If STEREO is positioned correctly, it aid in removing uncertainty when considering possible line of sight effects.

Building on all of the above missions, the Solar Dynamic Observatory (SDO) mission began in 2010 [Kaiser et al. \(2008\)](#). The instruments are developments of concepts used on previous missions but expanding them to allow constant viewing

of the entire solar disk. Consequently all instruments on SDO view the full solar disk, at all times, maintaining the same temporal cadence. Therefore, the SDO mission produces significantly more raw data than any previous missions. From a purely engineering standpoint, the instruments were carefully selected to facilitate the downloading of the data. As such, SDO has three instruments; the Helioseismic and Magnetic Imager (HMI) examining the solar variability and finer scale structure of the solar magnetic field; the Extreme Ultraviolet Variability Experiment (EVE) measures the total solar irradiance in the Extreme Ultra Violet section of the spectrum and the Atmospheric Imaging Assembly (AIA) investigating the upper chromosphere and corona.

AIA's imaging suite provides full disk images in  $4096 \times 4096$  resolution and most importantly at 12 second cadence. However, its distinguishing feature is the array of wavelengths analysing the atmosphere [Lemen et al. \(2012\)](#) associated with various temperatures corresponding to the appropriate electron transitions. The instrument ranges through 170, 30.4, 160, 17.1, 19.3, 21.1, 33.5, 9.4 and 13.1 nm providing a temperature range of 5000 K to  $1.6 \times 10^7$  K.

Without SDO the work in this thesis would not be possible. The constant full disk viewing greatly increases the chances of capturing the total evolution of a macrospicule. As such, it is used extensively in all of these studies as the main observational tool in Chapter 3, Chapter 4, and plays an essential roll in Chapter 5

## 1.2 Plasma behaviour

Stars are incredibly complex features despite their apparent simplicity when viewed by the naked eye. Their behaviour is entirely unlike any planetary body, and as has already been discussed, their inherent magnetic field makes their structure extremely complex. All of these affects can be traced back to the fact that the Sun consists of gas kept at high temperature and pressure, which causes it to form the 4<sup>th</sup> state of matter, plasma. Plasma is defined as a gas in which the molecules reached an energy level that cause them to eject their outermost electrons and become ions, causing the gas to be a neutral mixture of charged ions and free electrons (produced from ionising the molecules). It can be formed in several situations on Earth, such as a discharge of current from the atmosphere to the ground, manifesting as lightning as the propagating current ionises the air.

The motion and behaviour of a plasma can be defined on small scales by 3 factors; the plasma approximation, bulk interaction and the plasma frequency. The plasma approximation states that the particles must be close enough together that any given particle must influence all particles within the Debye screening length.

The length is dependant on the permittivity of free space, the Boltzmann constant, electron charge, temperatures of the ions and electrons, density of electrons and density of an atomic species and can be written as.

$$\lambda_D = \sqrt{(\epsilon_0 \kappa_B T_e) / (n_e q_e^2)} \quad (1.1)$$

Bulk interaction refers to the statement that the Debye screening length is small compared to the overall scale of the plasma, this implies that the motion of the interior guides the characteristic behaviour, rather than motion at the edges. Lastly the plasma frequency refers to the oscillation of the electrons within the plasma, which is valid in the case that the frequency is higher than the collisions between electrons and neutrals. In this case, the electrostatic interactions dominate over the standard, gas-like behaviour we would otherwise see. Of course, the case where all the molecules or atoms are ionised is the ideal case, however, in nature this is not always true. The degree of the ionisation is defined in terms of the ratio of ions to electrons,  $\alpha = n_i / (n_i + n_n)$  where  $i$  is the number density of ions and  $n$  for neutrals.

As is evident from the Debye screening length, the temperature of the plasma can have a dominating effect on the characteristics of the plasma. The temperature is a measure of the kinetic energy of the plasma, clearly higher kinetic energy therefore equates to a higher temperature of the plasma. However, electrons will reach a thermal equilibrium significantly faster than the ions and neutrals, in which situation the plasma will have two, or even three, populations. In the case where the plasma's electrons and ions are in thermal equilibrium with the neutrals the plasma is said to be thermal. In nonthermal plasmas, the electrons, whose temperatures raise quicker, will be at a higher temperature than the heavier ions and neutrals. The degree of ionisation of the plasma that results in a thermal equilibrium is defined;

$$x^2/x - 1 = (2\pi m_e)^{3/2} / h^3 (\kappa_B T)^{5/2} / p_{gas} \exp(-\chi / \kappa_B T), \text{ Saha (1920)} \quad (1.2)$$

where  $p_{gas}$  is the gas pressure,  $m_e$  is the mass of the electron and  $\chi$  is the ionisation energy (energy required to remove the least bound of the electrons around an atom). This form of the Saha ionisation equation will hold for Hydrogen, but does not take into account multiple ionisation processes, as would be the case for a more complex atom or molecule. The result of this is that degree of ionisation in a gas will increase with increases in temperature. It therefore follows that not all plasmas are fully ionised. At lower temperatures, the heavier elements won't gain enough energy to ionise, sometimes despite the fact that the electrons are orders of magnitude higher in temperature.

Plasma dynamics are significantly more complicated than those of a gas, due to the presence of inherent magnetic field. We therefore need a set of laws to define how the plasma behaves on scales such as those applicable on the Sun and in the atmosphere.

### 1.2.1 Magnetohydrodynamics

Magnetohydrodynamics are the set of laws by which we describe the motion of plasma on large scales. They were derived by [Alfvén \(1942\)](#), an achievement for which, Alfvén was awarded the Nobel Prize. The rules set up are a combination of the gas pressure equations and Maxwell's laws of electrodynamics, so let us now examine this relationship.

When considering a plasma, it is important to remember that while the total charge of the plasma will be quasi-neutral, the ions and electrons which constitute the mixture still carry charge. Consequently, motions in the plasma will cause the charges to have a change in velocity. In accordance with Faraday's law, a moving charge will cause a magnetic field to be induced and Ohms' law will also become a factor with charges moving through a magnetic field. As such, this can be an extremely complex problem. Let us begin our discussion with Maxwell's equations;

$$\nabla \times \mathbf{E} = -\frac{\partial \mathbf{B}}{\partial t} \quad \text{Faradays Law} \quad (1.3)$$

$$\nabla \times \mathbf{B} = \mu_0 \mathbf{j} + \frac{1}{c^2} \frac{\partial \mathbf{E}}{\partial t} \quad \text{Ampère Law} \quad (1.4)$$

$$\nabla \cdot \mathbf{E} = \frac{\tau}{\epsilon_0} \quad \text{Gauss' Law} \quad (1.5)$$

$$\nabla \cdot \mathbf{B} = 0 \quad \text{Gauss' law of magnetism} \quad (1.6)$$

(1.7)

where  $\mathbf{E}$  is the electric field strength,  $\mathbf{B}$  the magnetic field,  $t$  is time,  $c^2 = (\epsilon_0 \mu_0)^{-1}$ ,  $\epsilon_0$  is the vacuum permittivity,  $\mu_0$  is the permeability of free space,  $\mathbf{j}$  is the current density and  $\tau$  is the charge density. Faraday's law describes how a changing magnetic field would induce an electric field, hence it is also known as the Induction equation ([Goedbloed and Poedts, 2004](#)). Ampère's law describes the manner in which the magnetic field integrated around a closed loop, related to the electric current passing through said loop. Gauss' law for magnetism is also known as the Solenoidal condition and states that no magnetic monopoles exist and the eponymous law describes the resulting electric field caused by an electric charge.

The second 'half' of the magnetohydrodynamic equations are the laws for gas

dynamics, expressed in terms of the partial derivatives:

$$\frac{\partial \rho}{\partial t} + \nabla \cdot (\rho \mathbf{v}) = 0 \quad \text{Equation of mass conservation} \quad (1.8)$$

$$\frac{\partial p}{\partial t} + \mathbf{v} \cdot \nabla p + \gamma p \nabla \cdot \mathbf{v} = 0 \quad \text{Conservation of entropy} \quad (1.9)$$

in the Eulerian time-derivative reference frame, evaluated for a fixed position within the fluid. In the case of these two sets of equations, there is currently no link other than the velocity vector,  $\mathbf{v}(\mathbf{r}, t)$  which can be introduced through the equation of motion for a fluid element. The equation for the motion of the fluid element is derived from the rate of change of momentum equations

$$\frac{d}{dt} \int_V dV \rho \mathbf{v} = \int_V dV \rho \frac{d\mathbf{v}}{dt} = \text{rate of change of momentum} \quad (1.10)$$

In this case the rate if change of momentum will equal the net force on the fluid element, in accordance with newtons second law, therefore;

$$\rho \frac{d\mathbf{v}}{df} = \rho \mathbf{g} + \nabla \cdot [X] \quad (1.11)$$

where  $X$  is the total of all forces exerted on the fluid element. Therefore the equation which will incorporate all of these terms and calculate the acceleration on a fluid element is:

$$\rho \frac{d\mathbf{v}}{dt} = \mathbf{F} \equiv -\nabla p + \rho \mathbf{g} + \mathbf{j} \times \mathbf{B} + \tau \mathbf{E} \quad (1.12)$$

As we are currently assuming that we have a totally ionised fluid, therefore the electric field is defined as

$$\mathbf{E}' \equiv \mathbf{E} + \mathbf{v} \times \mathbf{B} = 0 \quad (1.13)$$

and therefore,  $\mathbf{E}'$  in a co-moving frame will vanish. The last assumption we need to make, is that the velocity of the plasma is not relativistic  $v \ll c$ .

This allows us to make some assertions as to the scale of the terms in Ampère's equation, the length scales of  $l_0$  and  $t_0$  are shown such that  $v = l_0/t_0$ . This means we can neglect the displacement current from Ampère's Law and define the current  $\mathbf{j}$  purely in terms of  $\mathbf{B}$ :

$$\mathbf{j} = \frac{1}{\mu_0} \nabla \times \mathbf{B} \quad (1.14)$$

As a result of which, we can neglect the effects of space charge on the plasma.

Additionally, the non-relativistic assumption means that we can also make a simplification to the acceleration of a fluid element equation as the electrostatic acceleration is small, as well, Gauss' law can be dropped through lack of need. As such the electric field can be expressed merely in terms of the velocity and magnetic field vectors:

$$\mathbf{E} = -\mathbf{v} \times \mathbf{B} \quad (1.15)$$

But applying the above assumptions, and substituting in for  $\mathbf{E}$  and  $\mathbf{j}$ , we obtain the basic equations of ideal magnetohydrodynamics (MHD).

$$\frac{\partial \rho}{\partial t} + \nabla \cdot (\rho \mathbf{v}) = 0 \quad (1.16)$$

$$\rho \left( \frac{\partial \mathbf{v}}{\partial t} + \mathbf{v} \cdot \nabla \mathbf{v} \right) + \nabla p - \rho \mathbf{g} - \frac{1}{\mu_0} (\nabla \times \mathbf{B}) \times \mathbf{B} = 0 \quad (1.17)$$

$$\frac{\partial p}{\partial t} + \mathbf{v} \cdot \nabla p + \gamma p \nabla \cdot \mathbf{v} = 0 \quad (1.18)$$

$$\frac{\partial \mathbf{B}}{\partial t} - \nabla \times (\mathbf{v} \times \mathbf{B}) = 0 \quad (1.19)$$

$$\nabla \cdot \mathbf{B} = 0 \quad (1.20)$$

These equations are therefore applicable to the case where; 1) the plasma is strongly collisional, such that the time-scale of the collision between the particles is much smaller than the characteristic time scales of the entire system. 2) The resistivity of these collisions is small *i.e.* the magnetic diffusion time scale much be longer than any other process occurring within the plasma. 3) The time-scale must be greater than that of the kinetic processes occurring within the plasma, such as ion gyration, Landau damping and length-scales longer than the ion skin depth and Larmor radius, [Goedbloed and Poedts \(2004\)](#).

By making choices with respect to the units for length, mass and time, the MHD equations can be made dimensionless. A typical length scale can be chosen such as  $l_0$  to be something sensible and  $\rho_0$  and  $B_0$  are chosen from a representative point in the plasma and the time unit can be inferred from a basic speed of the plasma, *e.g.* the sound speed or Alfvén speed.

$$v_0 \equiv v_{A,0} \equiv \frac{B_0}{\sqrt{\mu_0 \rho_0}} \text{ which leads to } t_0 \equiv \frac{l_0}{v_0} \quad (1.21)$$

The density, velocity, magnetic field etc. are then used to define new dimensionless parameters and substituted back into the MHD equations, which remain un-

changed but now have an operator for these variables instead of the variable themselves. The crucial outcome here is that the equations are not dependent on the size of the plasma evaluated, the magnetic field strength, the density or the time scale. After scaling  $l_0$ ,  $B_0$  and  $t_0$ , the pressure term becomes of vital importance and is linked to the ratio between the kinetic pressure of the plasma and magnetic pressure. This ratio is commonly referred to as the plasma beta, which is defined as:

$$\beta \equiv \frac{2\mu_0 p_0}{B_0^2} \quad (1.22)$$

This is an extremely useful flag when considering the behaviour of a plasma at a less precise level, as it indicates the forces dominant in a region. If  $\beta \gg 1$  the kinetic pressure terms are dominant, meaning that the kinetic motions of the plasma will determine its overall behaviour, such as in the photosphere and below. Whereas, in the chromosphere and upwards, the balance more favours the magnetic field and the gas movement is determined by magnetic effects. This leads us to another important result of ideal MHD, the frozen in condition.

We must first discuss the magnetic Reynolds number, which gives a dimensionless value to the ratio between the induction and diffusion taking place within the plasma. It can be defined, therefore, as a ratio of the two.

$$\mathfrak{R}_m = z \frac{VB/L}{\lambda B/L^2} = \frac{LV}{\lambda} \quad (1.23)$$

where  $B$  is the typical magnetic field,  $V$  is the typical velocity,  $L$  is the typical length and  $\lambda = c^2/4\pi\sigma$  is the magnetic diffusivity (Choudhuri, 1998). We can conclude that the Reynolds number depends significantly on the overall size of the plasma, and is therefore almost always large for astrophysical plasmas. We can now apply this to the induction equation in the context of said large scale astrophysical plasma. Here, we will examine the ideal MHD limit, which states that the plasma will be infinitely conductive. We can therefore write;

$$\frac{\mathbf{B}}{t} = \nabla \times (\mathbf{v} \times \mathbf{B}) \quad (1.24)$$

Then using the identity  $\frac{\mathbf{Q}}{t} = \nabla \times (\mathbf{v} \times \mathbf{Q})$ , which is applicable to the above equation and results in;

$$\frac{\partial}{\partial t} \int(S) \mathbf{B} \cdot d\mathbf{S} = 0 \quad (1.25)$$

we discuss this equation in terms of the Lagrangian operator, as we wish to follow integrated surface, as applied to the plasma, as a fluid element and examine the

variations in time. We can therefore deduce that the plasma will move with the magnetic field lines, this is known as Alfvén's theorem of flux freezing. Take a large-scale plasma such as those that originate in solar active regions. When a reconnection event occurs, magnetic fields can become detached from the solar atmosphere and can be ejected into the solar wind. The frozen in condition implies that the plasma which was on those field lines, will be carried with it. Alternatively, in a situation where the gas pressure is dominant low in the atmosphere, a gas perturbation will cause the magnetic field to wave as well.

### 1.2.2 Reconnection

The above processes are considered to be ideal cases for energy emission, for example, the dissipation of MHD waves is an ideal solution to the problem, converting magnetic energy into kinetic energy. The process is referred to as ideal, as it fulfils the conditions we highlighted above, that the plasma obeys Alfvén's theorem of frozen in-flux, and that 3 premises of effects of a kinetic scale are obeyed. However, in the reconnection process the frozen in condition is violated, as two plasma blobs which were connected by a field line, will now no longer be. It also, impinges on the assumption that the magnetic diffusion occurs on time scales significantly greater than the dynamic phenomena within the plasma, as reconnection takes place on much shorter time scales. This means that the reconnection mechanism itself is non-ideal. In such processes, the magnetic energy is converted to kinetic energy and heat, more on which later.

Reconnection was first proposed as a mechanism for magnetic X-type null points, such as those found in solar flares as demonstrated in [Giovanelli \(1946\)](#). The null point is considered to be the point at which the magnetic field vector has a resultant vector equal to zero, something which regularly occurs when two magnetic fields are interacting, for example during flux emergence. Subsequently this was followed up by [Dungey \(1953\)](#) who demonstrated that the collapse of the magnetic field near an X-type null point would lead to the formation of a current sheet. He also proposed the concept of breaking the magnetic field lines.

The first MHD model to describe a reconnection event, was the Sweet-Parker model ([Parker, 1957](#); [Sweet, 1958](#)), where the phrase, 'reconnection of field lines' was first utilised. Although, the model was flawed, the reconnection it predicted was insufficiently quick to describe a solar flare and subsequent massive release of energy. In the Sweet-Parker model, the current sheet that forms as a result of the interacting magnetic fields is on the global scale of the system, whereas [Petschek \(1964\)](#), utilised a current sheet many orders of magnitude smaller than that of Sweet-Parker.

In order for us to build a model for a reconnective event, we will need a few components, the magnetic field equations that describe the null point and a description of the current flowing over the change in magnetic field. Let us begin our discussion with the null points, of which, there are two kinds, elliptical and ‘X-type’. The ‘X-type’, which can be applied to who separate magnetic field systems coming together, is the situation which occurs most regularly within the solar atmosphere so we shall consider this mechanism.

In the situation, the field lines are hyperbolic, bending away from the centre, forming an X-type neutral point, of the type applied to the solar flare problem by the authors above. The limiting field lines are defined in terms of their angle of separation. These lines go through the origin, and are known as separatrices, and form the characteristic ‘X-type’ null point. The  $\bar{\alpha}$  value, which defines the angle between said separatrices, is related to the current density. Which we can calculate by taking the curl of the magnetic field, [Priest and Forbes \(2007\)](#)

$$\mathbf{j} = -\frac{B_0}{\mu_0 L_0} (1 - \bar{\alpha}^2) \hat{\mathbf{z}} \quad (1.26)$$

Where  $\hat{\mathbf{z}}$  points out of the  $xy$  plane. Now we have reached the point where the current density can be discussed with respect to the null point.

The current sheet typically appears at neutral points where there is a tangential discontinuity, in which case the the magnetic field is tangential and the plasma flow across the current sheet is zero. When the system is in equilibrium, the plasma either side of the sheet, and in the sheet itself, are in pressure balance. Usually, the total magnetic field on the current sheet will be zero, and we assume that the ambient pressures vanish, we can say that the magnetic pressure either side of the sheet is equal to the gas pressure on it:

$$\frac{B_2^2}{2\mu} = p_c = \frac{B_1^2}{2\mu} \quad (1.27)$$

where  $B_1$  and  $B_2$  are the magnetic fields either side of the current sheet and  $p_c$  is the gas pressure at the current sheet. It follows that the magnetic field undergoes an exact reversal in the magnetic field. If it is the case that the magnetic field within the sheet is parallel to the  $y$  axis and varies in  $x$ , is defined  $\mathbf{B} = B_y(x)\hat{\mathbf{y}}$ , applying Ampere's law can give us the current density in  $z$ :

$$j_z = \frac{1}{\mu} \frac{dB_y}{dx} \quad (1.28)$$

This means that when we get a steep gradient in  $B_y$  with respect to  $x$ , a strong current along the current sheet is produced perpendicular to the field lines. This is the

current sheet that lies at the heart of reconnection models, however the tangential discontinuity is susceptible to instabilities. Now that we have the null point between the two magnetic fields and the current sheet that forms as a result, we have the environment necessary to begin the reconnection of magnetic field lines.

Let us consider the induction equation again defining how the magnetic field changes with respect to the magnetic field,

$$\frac{\partial \mathbf{B}}{\partial t} = \nabla \times (\mathbf{v} \times \mathbf{B}) + \eta \nabla^2 \mathbf{B} \quad (1.29)$$

with the first term representing the advection and the second the diffusivity of the magnetic field. The ratio of these two terms can be represented by the magnetic Reynolds number,  $\mathfrak{R}_m = LV/\lambda$ , and of course, this value will dictate the evolution of the induction. The diffusion term dominates in the case where  $\mathfrak{R}_m \ll 1$ , however, we must be aware that this condition will not apply on large scales in the solar atmosphere, although it may be true on very small scales. The magnetic field can be defined in terms of a convection equation,  $\frac{\partial B}{\partial t} = \eta \frac{\partial^2 B}{\partial x^2}$ , describing the way the field diffuses away. We are assuming a thin current sheet in this case, with the magnetic field diffusing at a rate of  $\eta/l$ , where  $l$  is the width of the sheet and changes with  $(\eta t)^{1/2}$ , increasing with time. Whereby the magnetic field at a fixed position decreases, it is concluded that it has been annihilated.

The second mechanism for the changing of the magnetic field lines is advection. Under the condition  $\mathfrak{R}_m \gg 1$ , we drop the diffusive term from the induction equation. On these scales the frozen in condition applies, and the plasma is free to move up and down the magnetic field lines. In this scenario we define the velocity field lines to trace out a hydrodynamic stagnation point flow. This causes the field lines to flow inwards, and accumulate at  $x = 0$  at which point the magnetic field increases significantly. We also find that when the induction equation is considered in  $y$ , there is also a build up of field at  $x = 0$ , growing exponentially with time.

Examining the current sheet, and the accompanying increase in magnetic field strengths leads to a problem; on small scales of  $X$ , the diffusivity terms take over. Therefore there must exist a balance at which the rate of plasma transporting magnetic field in, must be balanced by the rate of diffusion away from  $x = 0$ , producing a steady state. Consequently, at  $x = 0$  we have the two magnetic fields meeting and cancelling, and in the case where resistivity is small, the magnetic gradient will be large, causing increasing amounts of magnetic energy to be converted to kinetic. While the magnetic field lines will disappear, the plasma which was formerly hosted on them will not, the result of this is that it will flow out of the system in  $z$ .

One of the first papers to demonstrate this in action at the solar surface was

Innes et al. (1997). The authors use the SUMER instrument to examine the Si IV 139.3 nm in two 90 minute observing windows with rastering consisting of 5 s exposures. The authors captured a 4 minute explosive event, 90 s after the onset of the feature the doppler shifts maximised, and the event had doubled in size in the east-west direction. They found that the asymmetries in the emission line, mirror those expected of a bidirectional jet, the flow axis of which is away from the line of sight and the centre of the two flows is paired with the origin of the jet. The velocity is calculated from the doppler shift, and given as  $100 \text{ km s}^{-1}$ . The apparent length of the jet 0.4 Mm, giving a true jet length of 1.2-2.4 Mm, therefore the jet stretches across the chromosphere and possibly encroached on the corona. This length falls in the lower end for macrospicules, however its lifetime is 3 minutes, which is a little low for a macrospicule.

# Chapter 2

## Jets and Macrospicules

The appearance of thin, explosive features with a relatively short lifespan has for a long time, been a part of solar physics. Spicules were first observed in 1877 by a Vatican observer, Angelo Secchi. This was aided by their sheer ubiquity, they were distinctly visible at the solar limb nearly all the time. However the larger-scale, more infrequent jets were more difficult to observe, particularly with early techniques.

### 2.1 The ejecta zoo

#### 2.1.1 Spicules

Jets and jet-like features are observed throughout the solar atmosphere, and as such a review of the topic is in order. As has already been discussed, spicules are among the smallest jets formed in the solar atmosphere. Most easily observed at the limb, they are long thin structures appearing brightly at the solar limb [Beckers \(1972\)](#). Spicules are found in the chromosphere, regularly observed in the H $\alpha$ , He II 30.4 nm, Ca II and Si IV. Work by [de Pontieu et al. \(2007\)](#) divided spicules into two populations, Type-1 and Type-2, with Type-1 being long lived while Type-2 have distinctly shorter lifetimes but are significantly more explosive and grow to much longer lengths. Type-1 spicules have an uprising speed of approximately  $20 \text{ km s}^{-1}$  and extend to 1 Mm in height with lifetimes of 10 mins, whereas the Type-2 spicules have been shown to extend approximately 5 Mm into the atmosphere and last for an average of 1-2 mins. The most comprehensive difference between the two is in the overall evolution of the feature. Type-1 spicules are observed to have a parabolic evolution, *i.e.* their tip traces out a ballistic arc when plotted against time. Conversely, Type-2 spicules are observed to dissipate or vanish as they evolve, and are primarily observed in the quiet Sun and coronal holes. Type-1 develop in active regions, and as

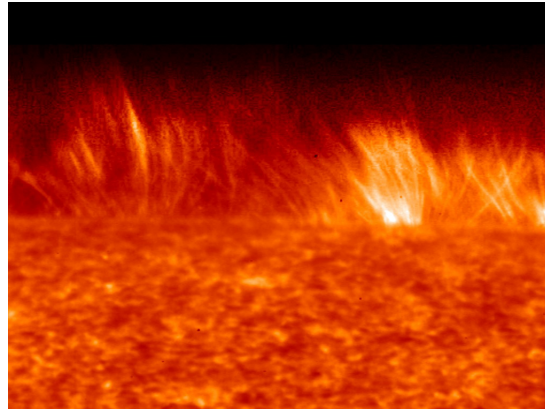


Fig. 2.1 Spicules as observed by at the solar limb using the new IRIS instrument observing at transition region temperatures. [http://www.nasa.gov/sites/default/files/images/751917main\\_highres4\\_full.jpg](http://www.nasa.gov/sites/default/files/images/751917main_highres4_full.jpg)

such Type-2 are far more numerous when recorded in a study such as Pereira et al. (2012).

Spicules are visible on the disk as well, but here they are seen as dark thin structures against the bright lower chromosphere. These were initially named mottles and fibrils, but have since been inherently linked with spicules - see De Pontieu et al. (2007); Rouppe van der Voort et al. (2009).

Since these initial propositions, however, there has been doubt cast as to whether this is the case or not. Zhang et al. (2012) found no statistical separation of populations within spicules. However, Pereira et al. (2014) have presented evidence that Type-2 spicules disappear from Ca II and reappear in the hotter Si IV and Mg II lines. There is also the proposal that these Type-2 features are RBE's, Kuridze et al. (2015); Rouppe van der Voort et al. (2015). This would imply that spicules are heating as they accelerate through the atmosphere. Whether this is because the underlying formation mechanism is different or because there is sufficient energy in the creation of the spicules to cause heating as they propagate through the atmosphere, has yet to be made clear.

The formation of spicules is still a matter of much debate given our currently limited ability to examine small scales in current observations. However, when observations are unable to provide explicit results, numerical and analytic approaches are utilised to fill in the gaps. De Pontieu et al. (2004) outline a mechanism for the formation of spicules which originates in the photosphere based on an analytic model. *P*-mode oscillations cannot pass through the photosphere due to the minima in the global temperature. However, leakage can occur in specific circumstances, allowing energy to transfer through this gap, until temperatures become high enough to allow propagation to start again. Essential to this model is the inclination of

the background magnetic field. The authors report that an inclined field vastly increases the cut-off frequency of waves tunnelling through the atmosphere. The lower density in the upper solar atmosphere causes the photospheric velocity generated by the *p*-modes to steepen into shocks, which leave an oscillating wake in the chromosphere, the spicule.

However, this is only one of many competing theories. [Takeuchi and Shibata \(2001\)](#) demonstrate a magnetic reconnection model driving formation of spicules, whereas [Martínez-Sykora et al. \(2011\)](#) formed a 3 dimensional model utilising the Lorentz force to push plasma across the solar surface until it meets vertical magnetic field which forces the plasma upwards. [Hollweg \(1982\)](#) demonstrate that a quasi-impulsive source in the photosphere is capable of generating a chain of rebound shocks in the chromosphere, causing the formation of a spicule. The issue with these mechanisms, is that they are significantly less repeatable in the solar environment, consequently the model proposed by [De Pontieu et al. \(2004\)](#) is still the best candidate for the formation of spicules.

A particularly pertinent model is proposed by [Moore et al. \(2011\)](#), in which magnetic reconnection is instigated by granule-sized 'magnetic bubbles'. This is applicable, as spicules are generally observed to form on the intergranular lanes. The authors propose that Type-2 spicules are an analogue for X-ray jets (more on which later). In this scenario, magnetic dipoles emerge from the photosphere which then interacts with the ambient field of the lower chromosphere, forming a raft of reconnection external to the dipole. During this reconnection, the interior of the dipole remains inert, while the outermost sections of the structure are released causing a 'sling shot snapping' of the magnetic reconnected field lines producing an upward jet (Type-2 spicule), Alfvén waves propagating up the ambient magnetic field lines and a fast MHD wave upwards across the magnetic field.

The advantages of this scenario for reconnection are that the environment which generates these spicules is extremely common in the solar atmosphere. The scenario here is particularly convenient as it also answers questions with respect to heating of the solar atmosphere. As a result of reconnection between the canopy region which forms over the granules and the more open magnetic fields higher in the atmosphere, shocks and waves are formed, which propagate upwards. The dissipation of the energy within these disturbances has been proposed on numerous occasions to be the central source of heating of the corona [Athay \(2000\)](#); [Klimchuk \(2012\)](#); [Kudoh and Shibata \(1999\)](#).

What becomes evident, after all of these models are formed, is that none of them generate both Type-1, and Type-2 spicules. It is therefore likely that they are indeed two separate features with [De Pontieu et al. \(2004\)](#) creating Type-1 macrospicules

and a reconnection model like that of [Moore et al. \(2011\)](#) is responsible for Type-2.

### 2.1.2 X-ray Jets

Throughout the solar atmosphere, we observe much larger jet-like features than spicules. They have been observed extensively, and not solely in the chromosphere. The first observations of more large scale jets were undertaken using the Soft X-Ray telescope on board Yohkoh [Tsuneta et al. \(1991\)](#). [Shimojo et al. \(1996\)](#) undertook the first statistical study of jets, finding a nice round 100 examples to study. With any study looking for specific features, the authors utilised the following selection criteria: 1) that the plasma was collimated and that the movement of the feature was in the direction of the collimation; 2) the aspect ratio of length to width is greater than 3; and 3) the time between the pre-jet image and the image in which the jet first appears is less than an hour. These are an excellent example of selection criteria which aide in forming the search, however, they are broad enough not to introduce bias into the sample.

The authors find that the jets are primarily initiated by a microflare/sub-flare at the base/footpoint (the terms are used interchangeably in literature) of the jet, sometimes apparent as a bright point. They find their lengths to be of the order 10 - 400 Mm and widths are of the order 5-500 Mm. Velocities along the direction of collimation are observed to range between 10 and 1000 km s<sup>-1</sup>, averaging at approximately 200 km s<sup>-1</sup>, and lifetimes can be up to 10 hours. In terms of physical evolution of their shapes, the authors find that 76% of the jets demonstrated converging shapes, *i.e.* the width of the jet would be constant over its evolution or decreasing with distance from the footpoint. The constant form were found to come from a wide variety of apparent source configurations, whereas the converging forms were, explicitly formed from energetic points. This work has formed the basis of much of the study of jet phenomena, however, this is merely an exploratory study around which future studies have been expanded.

## Models

What has become known as the standard model for the formation of solar jets is demonstrated by [Shibata et al. \(1992\)](#). Within this paper, the authors use the Soft X-Ray telescope on Yohkoh to examine 20 jets, and present their spatial properties, very similar to those of [Shimojo et al. \(1996\)](#), but the authors go on to describe a possible formation schematic. The model is based upon the flux emergence from the lower solar atmosphere, and is backed up by data in the Solar Geophysical Data. The authors demonstrate that the observations reveal a void at the jet base, similar

in appearance to voids observed in reconnection-driven events such as flares and CMEs. They proposed that the jets are rooted in the chromosphere, based on an inspection of the emission measure. Consequently it is likely that the mass is from the chromosphere. The authors go on to posit that the undulating and meandering shape of the jet lends itself to a helically twisting magnetic structure, suggesting that the jet itself emanates from a relaxation of the magentic field along a global flux tube [Shibata and Uchida \(1986\)](#). Such a reconnection event between twisted and untwisted magnetic field would be capable of producing a jet of this size, lifetime, and more importantly, velocity.

This model for the standard jet requires that there be open magnetic field lines, and that a smaller-scale, twisted, emerging flux loop rise from the lower atmosphere in order to initiate a reconnection event. As a result of the reconnection event, material in the emerging loop is than transferred into the open magnetic field lines, 'sling shotting' around the loop it was formerly a part of and up the open field lines, thus creating a collimated beam of plasma. The mechanism highlighted in this particular model produces exclusively narrow jets, a couple of megameters in width. It also results in the dissipation of large amounts of energy which manifests as brightenings in many observations. From the source of the reconnection, energised plasma then dissipates down the loops highlighting the entire structure. The visual effect of the long, collimated beam/plasma spire and the newly brightened loop of plasma, reveals an 'inverted-Y' shape or Eiffel tower-like structure, similar to the 'cusp' shape observed in significantly larger features high in the corona round streamers and flares [Vourlidas \(2006\)](#). These terms have gained common usage in literature and will be used hereafter.

An excellent example of this type of formation is demonstrated in [Nishizuka et al. \(2011\)](#). Within this work, the authors demonstrate what is referred to as an anemone jet, so called as the dome-like bipole magnetic bubble may be viewed as a feature similar to the sea creature. The model they build as a result of this is in three dimensions - consequently, the small scale loops of the standard model could be projected into 3D as an anemone-like shape. The authors observed the jet in Ca II, it formed along an inclined line approximately 45° away from normal, in the inverted-y format. With the jet forming in Ca II, we can conclude that this particular jet is formed in the upper chromosphere, and with this particular jet the authors observe the formation loop itself. The jet feature is found to extend 14 Mm into the atmosphere with a width of 6 Mm, and a maximum velocity of 100 km s<sup>-1</sup>. However, this maximum is observed 10 minutes into the evolution of the jet, contrary to what you might expect.

The standard jet model accurately describes a prominent section of the jet pop-

ulation. Those which it does not cover are highlighted in [Moore et al. \(2010\)](#). The specific example that the standard jet model does not cover is the case where the width of the jet is more than that predicted by the standard model. [Moore et al. \(2010\)](#) utilise Hinode/XRT to look for X-ray jets occurring in the polar coronal holes, and where possible the authors observed the same features in EUVI as well.

The initial magnetic field topology is largely similar to that of the standard jet, consisting of a small-scale loop within an open magnetic field region extending upwards. The difference in these models is that the emerging bipole arch in the case of the standard jet remains untwisted and without shear. In the case of blowout jets, this arch/loop is sufficiently twisted and sheared that it can drive an explosive eruption. In terms of the physical evolution, there is no difference between the two until the emerging flux element triggers a reconnection burst at the boundary between said emerging flux and the open magnetic field lines.

The authors then go on to suggest two resolutions to the reconnection event; the first is that the boundary becomes unstable on its own, and consequently reconnection begins on its own. This results in breakout reconnection, expelling the loop's outer magnetic field, which lifts the restriction on sheared flux lower in the system; consequently allowing the core of the emerging flux to erupt upwards. This forms a chain event, with emerging core events causing more reconnection and consequent releases and so on, similar to [Antiochos \(1998\)](#). The second permutation is that the sheared core begins to erupt before any reconnection takes place at the boundary. In this scenario, an instability in the emerging bipole causes the previously stable core to begin emerging. As a result, magnetic pressure at the boundary current sheet between the loop and open magnetic field, increases to the point at which breakout reconnection is triggered.

This work clearly has an impact on the current relationships between the various jets of scales larger than spicules (which clearly are their own feature). The authors propose that the blowout jets correspond to the macrospicule features in the chromosphere, more on which later. As for implications with respect to the division of standard and blowout jets, observations of the formation mechanism would clarify the feature. Standard jets would have large originating loops spanning approximately 20 Mm or not visible at temperatures lower than  $10^6$  K, whereas blowout jets need to produce strong signals in H $\alpha$  and He 30.4, due to the cooler plasma thrown upwards from the unstable magnetic bipole emerging.

### 2.1.3 Coronal Jets

One of the most comprehensive sets of jet observations is undertaken by [Madjarska \(2011\)](#), in which the authors observe a jet in an equatorial coronal hole, utilising SUMER on SoHO, EIS and XRT on Hinode and the EUVI instruments on the STEREO A and B. The authors find that the jet can be heated by microflares at the moment of reconnection, raising the temperature up to 12 MK. This was obtained using a DEM technique which combined the emission from a range of spectral lines to estimate the temperature. The density was approximated at  $4 \times 10^9 \text{ cm}^{-3}$  using a similar technique. The feature was found during a period of observing brightenings in the quiet Sun and coronal holes, where the subject appeared as a jet-like feature emanating from a pre-existing coronal bright point. The authors demonstrate an unequivocal shaping of the origin akin to that of the Shibata standard model. The event began with an increase in intensity at the original bright point, extending to a 3 - 4 arcsec<sup>2</sup> area, which the authors identify as a micro-flare. As a result of difference imaging, the authors then concluded that there were several reconnection events during this brightening phase. The expanding plasma in the BP is shown to have a multi-thermal structure, with the first blue shifting material spotted in hotter emission lines a full minute before the cooler material appears. These reconnection events continue to deposit energy into the jet-like feature, and upon each delivery of energy, an outflow occurs. The slowing down of the outflow also coincides with visible downflows in the underlying BP. During these accelerations, the plasma was shown to have a maximum velocity of 310 km s<sup>-1</sup>, while no red shifted down flow was observed at the same time as the energy deposits which would suggest that this is not a case of a bidirectional jet. The jet is seen to last for 18 minutes, however the first energy deposit occurred 27 minutes before the spire of the jet was visible. The authors note that their observations fit particularly well with the model presented by [Moreno-Insertis et al. \(2008\)](#), in which a current sheet is shown to form at the boundaries of the jet.

What becomes clear is that these large-scale jets can only be triggered by explosive reconnection events, therefore understanding this mechanism is essential to our understanding of solar jets. [Archontis et al. \(2005\)](#) demonstrate the mechanism governing the rules of this interaction. Essential to any useful numerical simulation is a reasonable set of initial conditions which succinctly defines the environment of the feature. [Archontis et al. \(2005\)](#) define a background stratification of the gases *i.e.* a non-magnetic series of decreasing density layers. The bipole is modelled as a horizontal magnetic tube which is inherently twisted and buoyant and a uniform horizontal magnetic field is used in the corona and transition region. The exact

parameters of the background stratification and magnetic tube are defined in [Fan \(2001\)](#).

The ‘box’ which contains the simulation, incorporates the top of the solar interior, to a depth of 3.74 Mm from the photosphere, the bottom of which is set as 0 and extends to 1.7 Mm, represented as an isothermal zone. Over the next 3.7 Mm of height, the temperature rises steeply mimicking the effects of the transition region. Lastly there is a second isothermal region which extends to a distance of 11.9 Mm from the photosphere.

The horizontal magnetic tube, which will eventually emerge through the atmosphere, has a Gaussian distribution, symmetrical about the longitude and the field lines are helically twisted in a uniform fashion around the central axis. The issue with this set-up is that in the case of kink-unstable cases, the model will suppress onset of internal current sheets. The stratification of the background gas is applied to the tube by applying a perturbation in the gas pressure, such that the stress tensor has zero divergence and vanished in the case  $r/R \gg 1$ .

The gas density within the tube is not however symmetrical about the ‘latitudinal’ direction. In order to illicit a rising response from the magnetic tube, the centre region is given a density  $1/\beta$  lower than the region around it as a result of the density perturbations. This causes the tube to undertake a transformation into the characteristic  $\Omega$ -loop shape which emerges into the atmosphere. Lastly the coronal magnetic field is straight horizontal and space filling, and is highest in the corona and reduces through the transition region and photosphere.

The simulations show that reconnection is immediate when the two flux objects come into contact, with the current sheet forming between them aligned with the direction of the axis of the flux tube. This is greatly accentuated by the horizontal field above, however, once the flux tube magnetic field and the coronal magnetic field are equal, the reconnection lessens to a smaller constant volume. At the current sheet region, the magnetic field lines of the flux tube are anti parallel to those of the coronal magnetic field. As the outer regions of the flux tube are cancelled away, however, the field in the tube rotates away from anti parallel as is the nature of a twisted flux tubes. Hence the boundary behaviour changed from the current sheet to a tangential discontinuity and finally to a rotational one.

The authors present evidence of continuous reconnection at the boundary. The work demonstrates that the first line undergoing reconnection, instead of passing through the boundary of the other end of the flux tube, it passes directly into the coronal region. The end point of the field line is then travelling at a new velocity, different to that of the local plasma at the new boundary. The implication of this is that field lines at the boundary between the two regions, undergoes continuous

reconnection, however, once it has passed though, it integrates into the coronal plasma. The helically twisted nature of the flux tube, allows for multiple reconnection instances. Consider looking at the end of the flux rope as a cross sectional area. When the reconnection occurs, a magnetic field line reconnects with the magnetic field in the corona, and is draw straight into the corona while the rest of the line remains attached to the flux tube instead of the entire line detaching. As a result of this gradual detachment and the twist, the end of the field line traces out a circular motion in our cross section; first reaching into the coronal then being draw around and through the transition region, underneath the tube, back through the atmosphere and into the corona before lastly returning to the solar interior.

Importantly, high speed jets are observed at the reconnection site, the plasma blasts through the current sheet before interacting with the higher pressure gas above it, therefore guiding it along the inclined magnetic field lines. In this case, the jets are observed as curves, and as such, disappear when observed on a horizontal plane. The authors then relate this to H $\alpha$  filaments and brightenings or jets in soft X-ray. The energy required to cause brightening in soft X-ray would be supplied by the interaction of these two flux systems, [Archontis et al. \(2005\)](#) also calculate a temperature increase to 10<sup>7</sup> K.

Recent studies have demonstrated the prevalence of smaller scale jets at the magnetic network boundaries. [Tian et al. \(2014\)](#), and later built on by [Narang et al. \(2016\)](#), highlighted these features using the most recent addition to the solar observational tools available to us. The network boundaries are regions where there is a great deal of magnetic complexity and strong field values, and almost certainly a large amount of reconnection will be apparent. These strong fluxes emminate from the boundaries of the granules, and therefore, convection cells. The evidence of this is apparent when imaging the transition region, the bright lanes approximately 20 Mm in size, it is possible that these regions appear bright in the transition region due to the heating as a result of reconnective events.

[Narang et al. \(2016\)](#) find explosive upflows in the direct images from IRIS with velocities of 80–250 km s<sup>-1</sup> and using the superior resolution of IRIS identify jet-like features developing from the bright networks. These jets are long and thin features, 4-15 Mm in length and are approximately 0.3 Mm in width, and demonstrate upflows, with no downflows evident. These events are extremely shortlived, with lifetimes measured at 20-80 seconds, however, there is recurrence observed with jets forming repeatedly in the same location, with time scales in the range 2-15 mins.

The ability to use spectral information, leads [Narang et al. \(2016\)](#) to the conclusion that the jet like features heat to temperatures of the order 10<sup>5</sup> km s<sup>-1</sup>, in this case the temperature of Si IV 139.377 nm. This Si IV line also allows an analysis of the

line broadening which could possibly be due to the field aligned jets, as is proposed in [Archontis et al. \(2005\)](#). The jets are also shown to be intermittent but effectively a continuous source of mass, and therefore energy, into the solar wind. As such, [Narang et al. \(2016\)](#) propose these network jets as new mechanism for generating the solar wind.

## 2.2 Macrospicules

The subject of this thesis is a clarification of the classification of macrospicules. They are features not dissimilar to jets, however they have been distinguished from the population of jets in the current literature, which will now be discussed below.

Macrospicules were first reported by [Bohlin et al. \(1975\)](#), utilising the SkyLab mission. This was undertaken using the 30.4 nm imager, which took observations of the polar coronal holes. The initial images were taken as raw light through particular filters over the lens, the images were also over exposed in order accentuate the appearance of the solar limb. The authors found that the newly named macrospicule was visible in He II 30.4, but was not apparent in Ne VII 46.5 nm or Mg IX 36.8 nm, observing the transition region and corona respectively. They then classified macrospicules according to 3 observables: that the macrospicules are confined to the coronal holes; that the macrospicules are increasingly inclined away from the normal proportionally to their distance from the solar pole (the authors link this to the supposedly weak, inclined magnetic field again); and lastly that they are only visible in 30.4 nm.

[Bohlin et al. \(1975\)](#) specifically differentiate between macrospicules and the H $\alpha$  spicules previously observed, stating that these new features have no counterpart in that line, citing [Moe et al. \(1975\)](#), who were unable to find a correlation between the two lines by direct observation or numerical correlation. Having said this, they make the caveat that there is a possibility that the formations of the two features could be largely similar.

With the limitations of the observations at the time, there was much debate as to whether this was actually the case. Following up on the work by [Bohlin et al. \(1975\)](#), [Labonte \(1979\)](#) utilised the Big Bear Solar Observatory to examine the 'limb surges' in H $\alpha$  and Deuterium 3 (D<sub>3</sub>). The authors found that the macrospicules in H $\alpha$  had considerable complexity in their structure, with 'knots, twists and loops' within the confines of the feature. But in D<sub>3</sub>, the authors only observe the brightest parts of the macrospicule, usually at the base of the structure apparent in H $\alpha$ . Differently in this case, the authors also observe features on the disk and define three categories: the macrospicules appearing similar to filament eruptions, surge-like

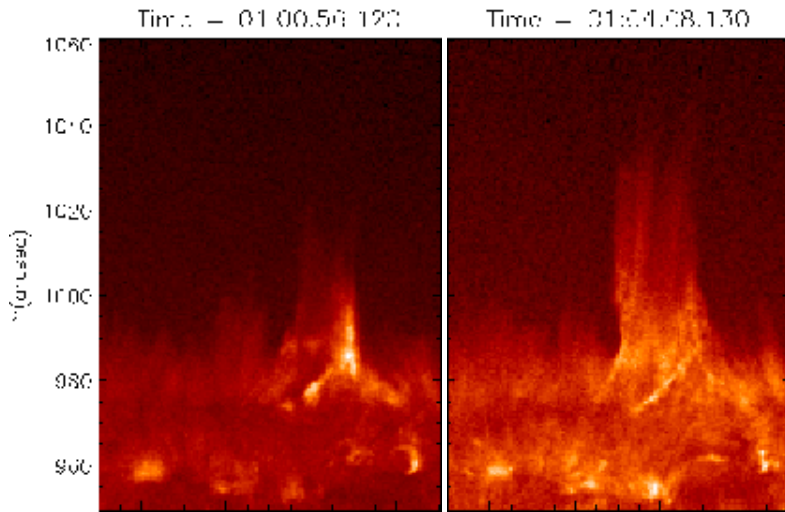


Fig. 2.2 The macrospicule examined by [Kayshap et al. \(2013\)](#). Utilising the 30.4 nm imager on AIA, the authors closely examine the bright point at the base of the jet.

macrospicules and a flare brightening type. Lastly, the paper finds the rate of occurrence of macrospicules to be of the order 1400 per solar day. This discussion as to the possible links between the two features goes on to this day, more on which later.

The next seminal work on macrospicules was published in [Dere et al. \(1989\)](#), again using an early space station, SpaceLab 2, as the platform for space based observations. In this case a Gregorian telescope was used to take a series of broadband UV observations at the solar limb. As a result of this setup the images are a convolution of the intensities from the solar continuum and therefore differentiating between structures is not possible. This means that only macrospicules' spatial extents could be observed, and specifically those which appeared above the limb, with no study of their onset. Consequently, this study was statistical in its focus with the aim of being to ascertain the basic spatial properties of the population.

[Dere et al. \(1989\)](#) then go on to compare the values obtained in this study to the two previously mentioned. The papers are generally in agreement, specifically Dere and LaBonte, citing lengths ranging between 3.75 - 24.75 Mm and similar widths, although Dere et al. find 0.45 - 6.75 Mm and LaBonte 0.45 - 4.5. Mm. The question of velocities is also raised, with values quoted as  $20 - 50 \text{ km s}^{-1}$  from Dere et al. and  $\leq 60 \text{ km s}^{-1}$  from ?. These values should possibly be taken with a pinch of salt as the temporal resolution for Dere and Labonte was 20 or 60 s and 60 s respectively, which will greatly influence the measurement of the velocity. However, Bohlin et al. found more extreme values than all of the other studies. Some of the lengths they find extend as far as 45 Mm. They also find greater widths - 3.75-11.25 Mm - and velocities reaching  $150 \text{ km s}^{-1}$ , although again the temporal resolution is poor,

$\geq \sim 180$  s. Although this early work had its limitations, the groundwork was laid here in order to be more precise when more sophisticated missions would be undertaken in the mid 90s with more focus on detail and less on statistical properties.

With the launch of SoHO in 1996, the community now had continuous viewing of the solar disk, meaning that consistent observations of macrospicules are now possible. One of the first studies utilising the new instruments was undertaken by [Pike and Harrison \(1997\)](#) using the Coronal Diagnostic Spectrometer (CDS). In this case, the instrument scanned from north to south pole, using a mosaic of rastered images, using the He I 58.433 nm, O V 62.973 nm and Mg IX 36.806 lines, corresponding to temperatures of 20,000, 250,000 and 1,000,000 K. In these observations the macrospicule is apparent at the limb, demonstrating two brightpoints visible in the footpoints either side of the structure, and a fainter column of plasma extending off the limb. [Pike and Harrison \(1997\)](#) find that the macrospicule is visible in the He I and O V lines, however not in the higher temperature magnesium line, showing that macrospicules can be found at transition region temperatures, but will not rise to coronal temperatures. The authors find the macrospicule to be 31 Mm in height and 13.3 Mm in width, agreeing with previous values.

The bright roots evident in the O V lines begin to form the 'inverted-Y' shape, typical of the standard jet formation mechanism outlined by [Shibata et al. \(1992\)](#). As a result of this, [Pike and Harrison \(1997\)](#) go on to discuss the nature of the feature and whether it is a macrospicule or X-ray jet. [Pike and Harrison \(1997\)](#) conclude that this feature is still classified as a macrospicule, due to the observations in He I and the feature adhering to the properties highlighted in [Bohlin et al. \(1975\)](#).

Building on the work done by [Pike and Harrison \(1997\)](#), [Parenti et al. \(2002\)](#) undertook an extremely detailed case study of a macrospicule observed in CDS. In this case the observations are still reliant on the macrospicule protruding above the limb, and observed using the full suite of spectra available to the authors. When discussing these papers, we must consider the rastering method of CDS. The images are comprised of vertical columns of pixels that are exposed for 30 s; the instrument then has a cooldown phase before moving onto the next vertical slit. This takes approximately 240 s, which is inappropriate for a feature which on average doesn't have a long lifespan. Because of this delay, the pixels in the x direction, from one column to the next, are separated by a time of 272 s. This means that we cannot consider the spatial structure in the x direction as continuous. As a result of this the authors use the columns of the image array to identify the temporal resolution of the macrospicule.

[Parenti et al. \(2002\)](#) find that the macrospicule extends to 26 Mm and reaches a maximum velocity of  $81.6 \text{ km s}^{-1}$  and an average outflow velocity of  $26 \text{ km s}^{-1}$ . The

spectroscopic nature of CDS allows for the calculation of temperature and density. As the full range of CDS's GIS suite is being used, the density is not strictly a single number and will be dependent on the emission in the various wavelengths. The density is highest in O IV,  $1.5 \times 10^{10}$  and varies throughout the lines but generally dropping to the order of  $10^8$  by the Si IX line. The temperatures are calculated as ratios between emission lines, *e.g.* O V 62.97 nm / O IV 55.45 nm, giving values around  $2.0 \times 10^5$  K, which the authors demonstrate is hotter than the surrounding atmosphere at that point, agreeing with previous works by [Habbal and Gonzalez \(1991\)](#).

As instrumentation improved, the use of spectroscopy resulted in the discovery of the rotational behaviour of a macrospicule as demonstrated in [Kamio et al. \(2010\)](#). In this case, the authors are utilising STEREO-A, the Hinode mission and SUMER. STEREO was used to observe the feature in 30.4 for straight-forward imaging, Hinode for dopplergrams and XRT and SUMER for spectroscopic data.

In the lead up to the particular case [Kamio et al. \(2010\)](#) examines, there were multiple coronal jets occurring at the source of the macrospicule over a 9-hour period. When the macrospicule erupted, again apparent were two footpoints at the base of the feature in the 30.4 nm STEREO images, however, in this study there is also a brightening in XRT at the same time. This is one of the first concrete examples of the relationship between macrospicules and X-ray jets. The authors highlight that the two foot-points then go on to form two threads propagating upwards, into the corona, subsequently utilising the SUMER instrument to detect their motion in detail.

The properties of this particular example in He II 30.4 are quoted as  $130 \pm 30$  km s $^{-1}$  for the radial extension of the feature and line-of-sight velocities of the order  $-15$  and  $-25$  km s $^{-1}$ . With respect to the X-ray jet behaviour, the velocity is measured at  $320 \pm 30$  km s $^{-1}$  and utilising the LOS velocity in He VIII and Fe XII led [Kamio et al. \(2010\)](#) to conclude that the structure of the macrospicule and X-ray jet. [Kamio et al. \(2010\)](#) also highlight the regression of the material back to the limb causing an enhancement in He II, a phenomenon they propose is caused by either heating in the upper part of the feature or a result of the density increase caused by the downflow of plasma.

The helical motion of macrospicules is reported in multiple papers. [Curdt and Tian \(2011\)](#) present observations of macrospicules in the transition region; they present two examples of 'explosive events'. In one case the feature is on the disk and in the second is above the limb. The discussion at the heart of the paper is differentiating between Rapid Red Extentions/Rapid Blue Extentions (RRE/RBE) pairs and helical motion, as observed in ?, due to the fact that they can be misinterpreted in

the data. In this case, the rotational velocity evident in the doppler images demonstrates symmetrical flow of the order  $40 \text{ km s}^{-1}$  for both examples. Using the slit modes of EIS, the authors rule out the possibility of lateral movement as a result of bidirectional RRE/RBEs, calculating that if this were the case, then the jet would be up to 7.2 Mm in each doppler component. This leads to the conclusion that the jet evident at the limb is moving helically, and consequently, that the feature observed on the disk is also a single jet rotating helically.

This is not the only formation mechanism for macrospicules proposed by the solar physics community; [Murawski et al. \(2011\)](#) describe an upward velocity pulse mechanism. [Murawski et al. \(2011\)](#) used the FLASH code, devised by [Lee and Deane \(2009\)](#), to solve a two dimensional scheme simulating the results of an upward velocity perturbation. Utilising both vertical and oblique magnetic field lines, [Murawski et al. \(2011\)](#) were able to generate a feature with very similar properties to an example macrospicule observed in AIA/SDO. The upward perturbation of plasma increases in amplitude with height, due to the decreasing density of the atmosphere, steepening into a shock. This shock, now in the upper chromosphere, launches cool 'spicule' material below. However, the size, velocity and height are more akin to macrospicules.

[Kayshap et al. \(2013\)](#) present a similar model to [Archontis et al. \(2005\)](#), with small scale flux emergence in the form of a magnetic tube containing an inherent kink, subsequently developing into the  $\Omega$  shape. The two halves of the tube meet at the bottom, triggering internal reconnection. The resultant macrospicule reaches 12 Mm in height, however, there is also a significant lateral drift. [Kayshap et al. \(2013\)](#) attempt to marry these observations with a two dimensional model, again using FLASH, and manage to produce similar values for the height, but not the observed drift. The amount of energy released by the macrospicule event is dependent on the location of the reconnection site, either high/low chromosphere or transition region. The velocity pulse resulting from this reconnection then goes on to initiate the slow speed shock as seen by [Murawski et al. \(2011\)](#).

# Chapter 3

## On the Statistics of Macrospicules

### 3.1 Introduction

Noticeable in Section 2.2, is the lack of recent statistical studies. A statistical study would be particularly pertinent at this time, given that we now have a generation of advanced instruments with extensive catalogues of data. It is now possible to re-examine the properties of macrospicules (MSs) and improve the picture yielded in previous studies *e.g.* [Bohlin et al. \(1975\)](#) and [Dere et al. \(1989\)](#). Furthermore, MSs are chromospheric objects which project upwards into the transition region, hence understanding MSs could enhance our knowledge of the region from the chromosphere up into the corona. We also need to confirm the features' place amongst the plethora of solar ejecta; jets, surges, rapid blue, or red, extensions, ordinary spicules to name a few [Tsirropoulou et al. \(2012\)](#).

The focus of this chapter is an observational discussion of what a macrospicule is; we present a set of characteristic spatial properties for the population of MSs investigated as well as the evolution of the structures, and also an inquiry into whether the properties of the MSs have any proxies to the solar cycle.

In order to analyse any potential relations over a solar cycle the sample of MSs will be taken over a time span of many years. Hence, we will use the 30.4 nm band-pass from the Atmospheric Imaging Assembly (AIA) camera on-board the Solar Dynamics Observatory (SDO) [Lemen et al. \(2012\)](#) which has been in place and operating since June 2010. As this was the epoch of the last solar minimum, we will take the sample through from this date until the end of 2012. This range will capture the ramp from solar minimum to the period which is estimated to be close to the solar maximum. In order to gain a significant sample size we will take two samples of two hours for each month during this period.

In Section 3.2 we present the relevant techniques used to take the measurements

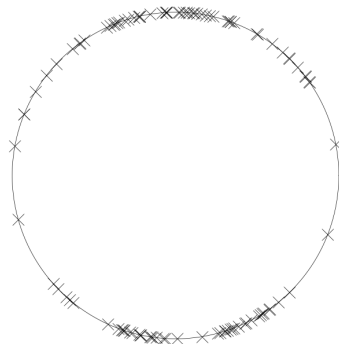


Fig. 3.1 The location of the samples of MSs displayed at the limb, indicated by the crosses.

and the instrument utilised. ?? presents the results of the study and discusses the consequences, specifically, with respect to the general spatial properties, followed by finding patterns over the sample time period and, then, a study of their evolution. Section 3.4 contains our conclusions.

## 3.2 Observations

The AIA instrument on-board SDO delivers  $4096 \times 4096$  pixel images with 0.6 arcsec/pixel spatial resolution and a 12 s cadence [Lemen et al. \(2012\)](#). Raw images were processed into a flattened-out limb such that the horizontal axis is the azimuthal angle and vertical is radius from the centre of the field of view. This allows a better measurement of the spatial properties of MSs.

The MSs were selected based on satisfying the following criteria:

- The evolution of the macrospicule is visible, *i.e.* the extension from the chromospheric surface to its maximum height and consequent regression back to the limb. This excludes examples which appear to disintegrate at some point during its evolution or the retraction of which is not visible.
- The footpoint of the macrospicule was exactly on the limb, rather than inside of or behind the limb. Avoiding the MSs which were too far inside the limb was aided by a limb indicating line, drawn based on information from the fits header files. Those events visibly crossing that line were not measured. It was harder to determine whether the MSs were behind the limb, but we made our best effort to ensure that the measured MSs were in the plane of sky, based on our inspection of the 30.4 nm movies.
- The objects were no longer than 200 arcsec; there are values for maximum length quoted in [Bohlin et al. \(1975\)](#) and [Dere et al. \(1989\)](#), however, we would

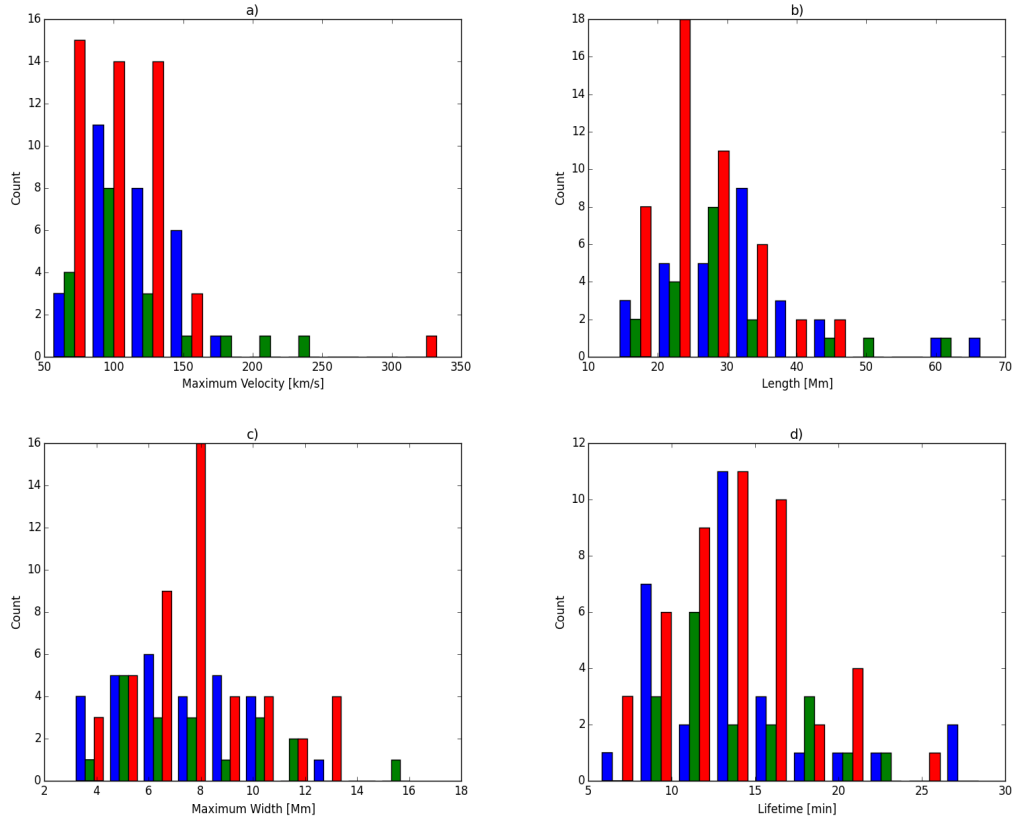


Fig. 3.2 Histograms of properties of MSs. In each bin counts from the 3 solar regions are displayed separately. Blue indicates coronal hole MSs, green represents coronal hole boundary MSs and red are occurrences in the quiet Sun. a) top left. Histogram detailing the values of maximum velocity over the sample period. General grouping around the mean for all regions, 109.7 km/s, and an absence of clear distributions is evident, particularly in the quiet Sun, top left. b) top right. Detailing the maximum lengths, separate behaviour is found for all regions, quiet Sun displaying a distinctly lower peak, top right. c) bottom left. Maximum width of the MSs, irregular distributions are clear with very little difference between the regions, bottom left. d) The lifetimes again show little difference in range, however MSs at the coronal hole boundary have a slightly higher mean, bottom right.

like to test the length limits of MSs in order to more accurately define these phenomena. There is also a lower limit imposed upon us by the data itself. The so called 'forest of spicules' at the solar limb prevents us from measuring any features with a maximum length of less than  $5z$  Mm. We also call into question whether the features observed by those earlier authors were actually MSs, there is certainly significant overlap in the lower percentiles of the population of spicules and MSs.

Each 30.4 nm image was analysed separately and the length of the macrospicule in question is measured, defined here as the distance between the foot and tip of the macrospicule. We then took the mid point of the line between the foot and tip, and

consequently used the mid point as a reference point for measuring the width. We used the bottom of the macrospicule brightening as  $l_0$  and in situations where there was none, we used the lowest point at which plasma motion was initially observed. Using this method, we obtained information on the macrospicule with 12 s cadence. Within the stated sample period we took 2-hour samples on the 1st and 15th of each and every month.

Having undertaken the study, the distribution of the locii of macrospicule events measured along the solar limb is displayed in Fig. 3.1. There are 101 examples in this study. Note that there is some ambiguity in measuring spatial properties of features near the limb due to line-of-sight integration. However, without using data observing the MSs from multiple directions, the best approximation is that MSs are generated in the plane-of-sky, despite the potential uncertainties inherent in measuring at the limb.

### 3.3 Results and Discussions

Following the analysis of the MSs as described above, the properties and, therefore, statistics for the sample of MSs are found. Of the sample we find that 30.5% of MSs occurred in polar coronal holes, 20.0% occurred at the coronal hole boundaries and 49.5% were found in the quiet Sun. The coronal hole boundary is defined loosely as the region where the coronal hole and quiet Sun meet. It is evident in the 30.4 nm images that the coronal hole is significantly dimmer than the quiet Sun. There are 10 Mm where the transition between the two regions takes place. If a macrospicule is neither clearly in the quiet Sun or coronal hole in this region and within this region, it is defined as being in the coronal hole boundary.

Macrospicules generated near complex magnetic regions were not measured, due to the possibility of these regions influencing the measurement or of falsely identifying a feature as a macrospicule. Since active regions qualify as regions of complex magnetic field, MSs forming in their proximity were excluded.

#### 3.3.1 General Properties

We begin with constructing the histograms for the individual properties, *i.e.*, distribution of velocities, lengths, widths and lifetimes. Examining these general properties, we will consider each property in terms of the magnetic environments.

Beginning with the maximum velocities in Fig. 3.2a, note the almost uniform distribution of MSs found in the quiet Sun between 50-150 km/s falling steeply after. The outlier in the 300-350 km/s band is a value which may have errors. The respec-

tive range and mean values are, for the quiet Sun: 54.1-335.1 km/s and 105.2 km/s, for coronal holes: 58.3-181.0 km/s and 113.4 km/s, and for coronal hole boundaries: 66.8-236.0 km/s and 114.5 km/s. These values are quoted with an error on each value of  $\pm 2.2$  km/s.

We observe similar maximum velocity mean values for coronal holes and coronal hole boundaries while the quiet Sun has a lower average maximum velocity. This could imply different generation processes for MSs in the coronal holes and at coronal hole boundaries, where reconnection is evident [Patsourakos et al. \(1999\)](#) and is a possible source for MSs (see [Heggland et al. \(2009\)](#)). However, there is not enough evidence to conclude that MSs are produced differently in other magnetic environments. Within the coronal hole it has been proposed that a collection of smaller spicules forms a macrospicule ?, which would explain similar mean maximum velocities.

Where the maximum velocity occurs over the trajectory of the macrospicule is important, particularly for future modelling. We find that the maximum velocity of the macrospicule occurred within the first 19% of the macrospicule's evolution in 68% of cases.

Fig. 3.2b shows the maximum lengths of all macrospicule instances. Investigation reveals ranges and means as follows, with errors of  $\pm 1.5$  Mm; coronal hole lengths range of 17.3-69.8 Mm with a mean 31.9 Mm, at coronal hole boundary the range is 16.1-60.2 Mm with a mean 30.2 Mm and for the quiet Sun the range is 14-45.3 Mm with a mean of 25.4 Mm.

We observe similar means and ranges for the lengths of the coronal hole and coronal hole boundary populations. This is unsurprising due to the open field nature of both regions allowing extension up the field lines. Whereas, in the quiet Sun, the mean value is 18% less than those observed in the coronal hole/boundary. We draw attention to the narrower range in the quiet Sun as well. These values could be the consequence of the more complex magnetic field above the feature not allowing as much growth.

From examining Fig. 3.2c, detailing the maximum width of each macrospicule, it is evident that there are no distinct peaks in any of the populations in the coronal hole/boundary regions. After investigating the means, very similar values are revealed, 7.2, 7.9 and 7.8 Mm for coronal holes, coronal hole boundaries and quiet Sun, respectively. The mean value for the quiet Sun coincides with the peak, but again, has no mathematically definable distribution. Of interest is the ratio between the width and length of MSs, particularly useful in reference to modelling. Values found are; for coronal holes, 0.24, for coronal hole boundaries, 0.26 and for quiet Sun 0.32, demonstrating that the width is small compared to the length of the

macrospicule. Finally, it is evident that MSs in the coronal hole/boundary regions have a lower ratio value than instances in the quiet Sun regions.

The lifetimes (Fig. 3.2d) have a similar lack of difference between the populations seen in the width distribution. Ranges and means are as follows; for coronal hole 7.8-28.6 min and mean 13.4 min, for coronal hole boundary 9.8-22.0 min and mean 14.4 min, and for quiet Sun 5.6-30.6 min and mean 13.6 min. The values obtained show similar ranges for coronal hole and quiet Sun instances but a smaller range for MSs at the boundary. However we suspect that these are insignificant as the error in lifetime is  $\pm 1.1$  min, implying that the means are similar for all three magnetic environments.

These values, found during the present analysis, are in-between the sets of values put forward by [Bohlin et al. \(1975\)](#) and [Dere et al. \(1989\)](#).

### 3.3.2 Inclination

From previous studies it has been noted that MSs have inherent inclination. [Bohlin et al. \(1975\)](#) noted that the further from the pole of the Sun the greater the inclination of the macrospicule. It is worth noting here that they did not in fact consider any MSs outside of the coronal holes.

We plotted the MSs according to latitude and magnetic environment, Fig. 3.3. This graph shows the latitudes of each macrospicule instance against the degree of inclination; there are clear indicators where the coronal holes are. What is noticeable at this point is the fact that lower inclinations are associated with the ordinary coronal hole features but that MSs occurring at the coronal hole boundary have a greater inclination, with no events which have a value lower than  $15^\circ$ . Quiet Sun events have an almost uniform distribution even appearing to occur in a coronal hole, but this is an artefact of the size of the coronal hole changing with the solar cycle and becoming very small as the Sun nears the solar maximum.

### 3.3.3 Relation between macrospicule properties

It is worth investigating whether the properties, discussed earlier, have any empirical relation to each other. Fig. 3.4 shows the relationships between the maximum length, maximum velocity and lifetime of each macrospicule observation. Inspecting Fig. 3.4a, reveals a clear correlation between the maximum length and the maximum velocity, as indicated by the least-squared regression,

$$v = 61.3(1 + 0.28L), \quad (3.1)$$

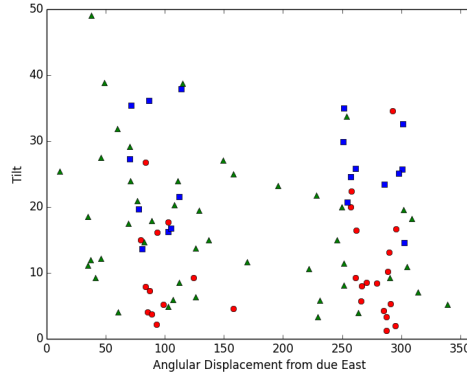


Fig. 3.3 Macrospicule events are plotted in terms of latitude and inclination. Inclination is defined here as the angle away from the normal to the limb of the Sun. The latitude is defined from due east and traces out anticlockwise. The red circles here are instances in the coronal hole, blue squares are at coronal hole boundaries and the green triangles are quiet Sun.

where  $v$  [Mm/s] is velocity and  $L$  [Mm] is the maximum length, the normal residual of which is 0.43, indicating a significant fit. There is a particular exception in the top left of the plot which may have some errors and has altered the slope of the regression line quite distinctly.

There is a similar pattern to be reported in Fig. 3.4b, where the lifetime and maximum length have been plotted against each other.

$$L = 10.39(1 + 0.12T), \quad (3.2)$$

where  $L$  length in Mm and  $T$  is the lifetime in min and normal residual value 0.66. This value is small compared the average maximum length, therefore the fit is reliable. Again, there are a few extreme instances which may not be a part of the overall macrospicule population, such as the instance in the bottom right with a short maximum length but long lifetime.

Lastly, Fig. 3.4c, shows the relationship between the maximum velocity and the lifetime of MSs, defined,

$$v = 88.9(1 + 0.016T). \quad (3.3)$$

Incongruously, relationship between the maximum velocity and the lifetime of the MSs is unclear. A shallow trend is apparent in the scaling factor, 0.016, which is inconclusive as to whether a relationship exists between the two properties, however it is unlikely.

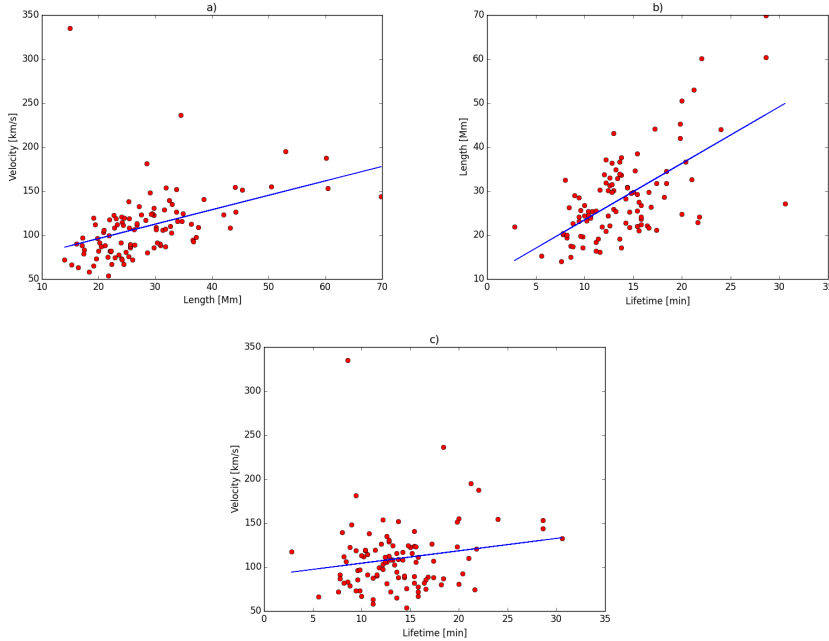


Fig. 3.4 Properties of MSs features plotted with respect to each other. a) Top: The max length against the max velocity for each individual instance. The least-squares fit shows a distinct correlation. b) Middle: The lifetime vs max length graph shows a similar degree of correlation between these two properties, middle. c) Bottom: In the case of max velocity and lifetime, there is no such relation, as is indicated by the least squares fit and scaling equation (below). Error bars associated with the least squares fit are omitted as the standard error is small compared to the range of values.

### 3.3.4 How the macrospicule general properties change over the sample period

The investigated sample period is a proxy for the process by which the Sun's activity increases from solar minimum in 2010 up to solar maximum at the end of 2012. Therefore, examining the macrospicule properties over the sample period is a worthy exercise and may give insight into the cause of MSs. Fig 3.5 illustrates how the general properties alter over the sample time period. Examining first the maximum length, Fig. 3.5a, shows a relationship over the entire sample period, with some instances where the maximum length values do not appear to be part of the overall population.

However, these examples, which are over 50 Mm, are not necessarily too extreme to be classed as MSs. Upon visual examination of the five most extreme examples there are no discernible differences in the four instances between 50 Mm and 60 Mm in height. The most extreme example, 69.8 Mm, does appear separate from the population. It is wider than average and the structure is less defined and more fractious. This can be removed from the sample. The mathematical relation of the

fitted line, using least squares, reflects the general trend upwards over the sample time period,

$$L = 24.9(1 + 0.11t), \quad (3.4)$$

where  $L$  is the maximum length of a macrospicule and  $t$  is the point in time. The gradient value is small, but is a result of the long period over which the sample has been taken.

Studying the lifetime property of the MSs over the solar cycle in Fig. 3.5b we, again, notice an increase over the sample-time period, though the gradient is not as steep as that of the fit for the maximum lengths,

$$T = 12.7(1 + 0.074t), \quad (3.5)$$

where  $T$  [min] is the lifetime of a macrospicule and  $t$  is the time [years]. There seems to be a general population close to the fit with only a few extreme examples, e.g. one below the general population and 3 above 25 min. We closely examined the extreme examples in this case as well. Only the macrospicule with the longest lifetime showed any particular differentiation from the rest of the population. Greater width is observed alongside apparent separate structures within the macrospicule, therefore this instance is eliminated from the study.

The most interesting result here is that when inspecting the maximum velocity over the sample period, see Fig. 3.5c. We notice that the maximum velocity changes very little, the magnitude of the gradient is indicative of a small decline,

$$V = 113.03(1 - 0.025t), \quad (3.6)$$

where  $V$  is the maximum velocity in Mm/s. Given that we found that in Fig. 3.5c, the maximum length and maximum velocity are related, one would naturally expect the maximum velocity to show a similar behaviour over the sample time period. Again, we visually examined the extreme examples eliminated two instances, a maximum velocity of 335.9 km/s was clearly an error in measurement and so has been removed and the second is not clearly defined and may have suffered from limb effects. (All extreme examples are included in the graphs here, but however are excluded from our final statements.)

### 3.3.5 Ballistics

How the features behave over their life-span is important in terms of possible generation mechanisms, and how they may interact with the transition region. SDO has

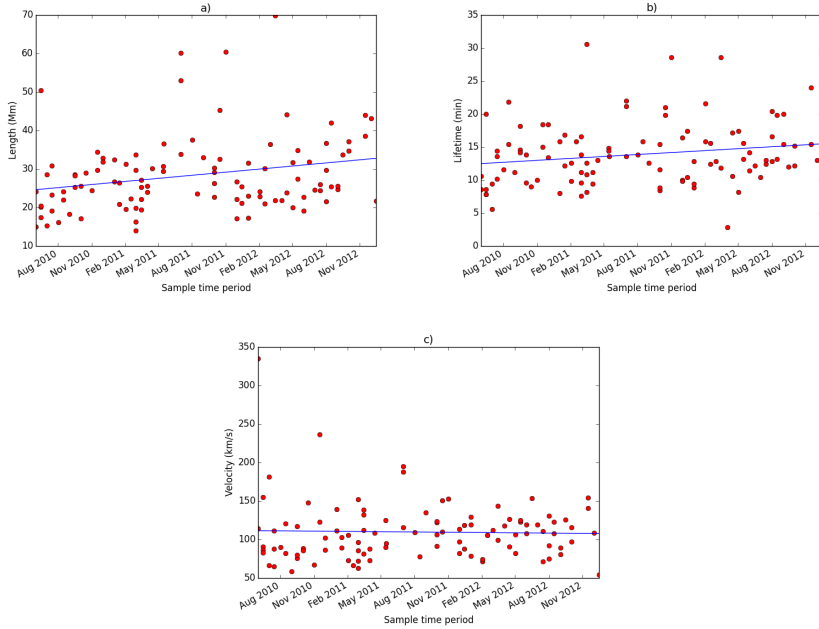


Fig. 3.5 Macrospicule properties over the sample time period. Notice that the graphs for maximum length and lifetimes, a) top and b) middle, respectively, have general trends with a positive gradient over the sample time period, while the maximum velocity graph, (c, bottom panel) has none of the same trends apparent in the others.

limited spectral data as AIA is an imager. Therefore, readings are limited to spatial measurements. One interesting question is whether MSs have a ballistic nature such that upon reaching their highest point they would then fall back only under the influence of the Sun's gravity. The question is of importance due to the nature of ordinary spicules typically located at granular lanes.

Current research proposes two varieties of spicules, type-1 and type-2, [Pereira et al. \(2012\)](#), but [Zhang et al. \(2012\)](#) debates this point, and finds no such population split. We believe that names of physical phenomena should be based on the underlying physics, not arbitrary behaviour. Type-1 spicules are potentially driven by *p*-mode global oscillations, and spicules typically have lifetimes of 4 - 10 mins and heights 7 - 10 mins [De Pontieu et al. \(2004\)](#).

Type-2 spicules are most likely reconnection events, which helps explain their high velocities, similar lengths to type-1 and typically observed with much shorter lifetimes, 10 - 150 s, [Isobe et al. \(2008\)](#). Type-2 spicules are observed not to fall back to the solar surface, however, there is debate as to whether these features are physical, or an artefact of observation [Tsiropoula et al. \(2012\)](#), [Sekse et al. \(2013\)](#) or finally whether their regression is observed in a different wavelength [Pereira et al. \(2014\)](#).

The question becomes: are these MSs giant versions of *p*-mode spicules, or

are they blown-up manifestations of reconnection spicules. Alternatively, are they related to these ejecta at all? In order to answer these questions, one needs to understand what the underlying driving mechanism for type-1 and type-2 spicule. Consequently, one needs to find signatures of driver(s) in the formation of MSs. An interesting alternative suggestion for generation of MSs is a model where multiple spicules form a macrospicule [Xia et al. \(2005\)](#).

The final case is that MSs and spicules are not related in their formation at all. [Shibata et al. \(1992\)](#) proposed a jet formation model which has become known as the 'Inverted Y' jet model which occurs on much larger scales than spicules. Using Yohkoh's Soft X-Ray Telescope (SXT), they highlighted the X-ray jets had lengths in the 5-40 Mm and velocities in the order 30-300 km/s, notably, similar to the values we have quoted above. This fits in with the observations of [Moore et al. \(1977\)](#) of X-ray bright points coinciding with H $\alpha$  MSs, (also supposed in [Kamio et al. \(2010\)](#)). Another model presented by [Jiang et al. \(2007\)](#) proposes magnetic flux emergence as a source for H $\alpha$  and EUV jets. They find lengths similar to those discovered as well, 4-22 Mm with a lifetime range of 10-34 mins (including cool and hot aspects of the jet). Both values are also comparable to those we observe in this study.

Given this, one might expect that there is a consensus that these are the same objects observed in different wavelengths, however, this is not the case. [Moore et al. \(2010\)](#) highlight a dichotomy in solar coronal jets, certainly between the standard jets [Shibata et al. \(1992\)](#) and blowout model for jet formation which the authors described. The authors concluded that the blowout jet model results in Helium 30.4 nm MSs forming from base arches of the order 10 Mm in width. If we assume that MSs observed in H $\alpha$  and Helium 30.4 nm are the same feature as supposed by [Labonte \(1979\)](#) and implied by [Parenti et al. \(2002\)](#), then is it reasonable to propose that the blowout jet mechanism also drives EUV MSs.

Examining Fig. 3.6 there are two particular trends to note. The first is shown in Fig. 3.6a, where the times for the regression back down to the solar limb were taken from the observational values, blue point in the figure, and times calculated using basic gravitational laws, assuming point mass and free-fall under uniform gravitational acceleration from the tip of the macrospicule, are in red.

We observe similar times for regression back to the limb for the estimates and the recorded times. Clearly there is a greater variance in the measured values compared to the estimates, but this is to be expected. The mean time for the tip to recede back to the limb is 7.5 min estimated and 6.6 min recorded, with the similar values indicating that gravity is the dominating force behind their fall. The difference between the two sides of the evolution is 6.6% of the average overall lifetime, which is likely not large enough to be significant.

Let us now make a brief comparison of this behaviour described by the current literature. Recent studies have found that the time taken for a jet to fall back to the solar surface is greater than expected from a ballistic model. [Nishizuka et al. \(2011\)](#) find that chromospheric jets (small jets, 1-4 Mm in length with a magnetic anemone base) share similar motions with the shock-acceleration model demonstrated in [Shibata and Suematsu \(1982\)](#), notably, slower than a ballistic model. [Moschou et al. \(2013\)](#) also find velocities lower than those under a ballistic model, however, the features highlighted here are much larger, measuring 100-190 Mm in length, than MSs. [Feng et al. \(2012\)](#) demonstrate that kinematic motions of the particles in jets follow ballistic trajectories. Therefore it is possible that in MSs the plasma-beta is high, and the entire feature follows the ballistic nature of the gas particles. Otherwise, the observed motion may be due to the surrounding magnetic environment. Macrospicules examined here were deliberately chosen in locations where there was a lack of complicated magnetic environment, hence would be allowed to evolve on their own.

Fig. 3.6b, demonstrates the change in width either side of the greatest extent of the macrospicule as a percentage. We find that after the peak of the macrospicule, the width actually decreases on average with MSs being 20% smaller. This could be due to plasma flowing down magnetic field lines causing a thinning within the macrospicule. This could delay the collapse of the macrospicule and cause the slightly longer recorded times as opposed to the estimated times.

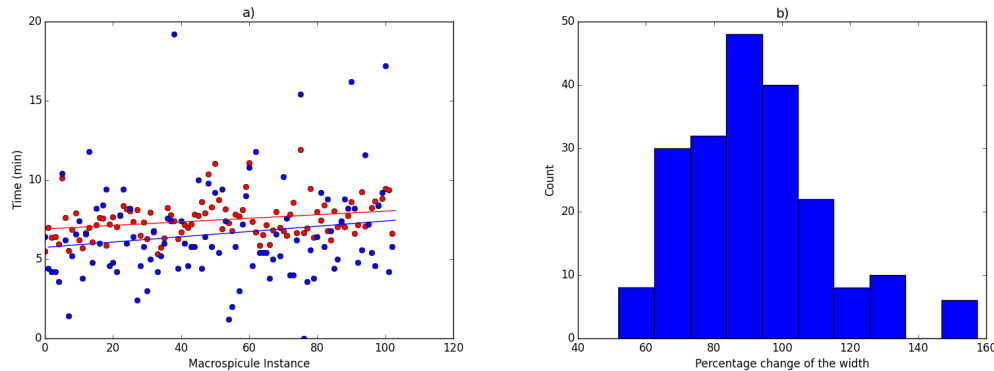


Fig. 3.6 Estimated times for a point mass falling from the apex of the macrospicule trajectories, a) top, for the macrospicule are red, while the times taken from the data are blue points, top panel. There is little deviation from ballistic model evident in the MSs measured times. b), bottom, the percentage change in width. The widths are taken before and after the peak of the length-time plot as a percentage change. The width is smaller, on average, after the peak.

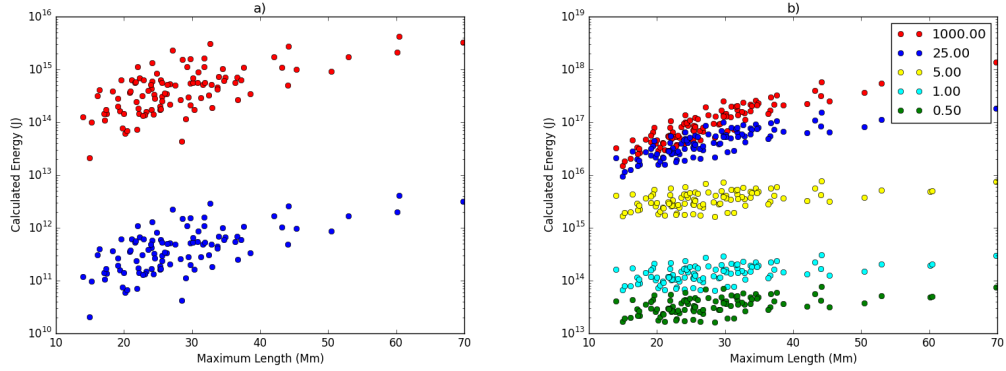


Fig. 3.7 a) Here we have used two different  $\rho_0$  values. Red indicates  $\rho_0 = 1.0 \times 10^{-8} \text{ kg/m}^3$  and blue indicates  $\rho_0 = 1.0 \times 10^{-11} \text{ kg/m}^3$ . b) The energy required to form a macrospicule plotted as a function of the maximum length of the macrospicule. The maximum length is plotted against the energy required to move a mass to this height. The scale-height value of 1000 Mm here is used as a proxy for uniform density as this is approximately 10 times greater than the largest macrospicule in the sample, which, makes the assumption valid.

### 3.3.6 Energetics and scale-height

Examining the energy required to generate MSs is a worthwhile task, in reference to the process to which they are formed. At the limb  $g = 276 \text{ ms}^2$ , hence, the gravitational scale-height will need to be taken into account when performing any calculations. [Pereira et al. \(2012\)](#) has studied this behaviour in the case of spicules, however, no such study has been performed for MSs to date. We have modelled the MSs simply as a column of plasma, with no magnetic field influences, and considered the potential energy required to reach the height at which they are observed. Choosing a  $\rho_0$  is important, measurements by [Parenti et al. \(2002\)](#) and [Withbroe et al. \(1976\)](#) give densities of MSs as  $1.0 \times 10^{-11} \text{ kg/m}^3$ . However, we assume here a scale-height over the extension of the macrospicule and these authors measure the 'body' of the macrospicule. As such, we use a  $\rho_0$  taken from [Vernazza et al. \(1981\)](#),  $\rho_0 = 1.0 \times 10^{-8} \text{ kg/m}^3$ . Given that we use a scale-height and applying our  $\rho_0$  at the footpoint, we will obtain a sensible value for the energy required to form a macrospicule.

The centre of mass was estimated, and the potential energy necessary to move the mass from the limb this point defined as:

$$R_y = \frac{Le^{-L/H} - He^{-L/H} + H}{1 + e^{-L/H}}, \quad (3.7)$$

where  $R_y$  is the distance from the solar limb,  $H$  is the scale-height and  $L$  is the maximum length of the macrospicule.

Integrating over the volume of the macrospicule, taking into account the scale-height, estimated the mass. Applying the mass as a point at  $R_y$ , the minimum me-

chanical energy required to form a macrospicule is equal to the potential energy at  $R_y$ . Fig. 3.7 demonstrates how the estimated energy required will change dependent on the scale-height of the plasma contained within the macrospicule.

As is intuitive, the more uniform the density, the higher the energy required to form the macrospicule. Noticeable are the gradients at higher scale-heights,  $1.61 \times 10^{16} \text{ J/Mm}$  with uniform scale-height, and, when  $H = 0.5 \text{ Mm}$  the gradient is  $6.88 \times 10^{11} \text{ J/Mm}$ . This is important as the more energy required to form a macrospicule of a given length, the less likely they are to form. Instances of MSs in uniform density and with a scale-height of 25 Mm are similar below heights of 25 Mm.

Macrospicules have been proposed as a source of coronal heating. In order to estimate how much mechanical energy could potentially be transferred from the MSs into the corona, we will assume that at any given moment, a macrospicule is occurring at the limb. Assuming that measurements taken here are within  $\pm 10 \text{ Mm}$  of the plane of sky, we take the next interval in which a macrospicule occurs as the angular distance, covering the  $\pm 10 \text{ Mm}$  over the plane of sky, starting at the boundary of the previous interval.

Extrapolating this around the rest of the solar surface and applying the mean macrospicule count per two hour sample, 1.9, to each interval a power output can be estimated. Assuming further that all mechanical energy is transferred from the macrospicule into the corona, the power output for uniform scale-height MSs is calculated to be  $0.153 \times 10^{-3} \text{ W/m}^2$  and decreasing with the scale-height. Given the power requirements for coronal heating in [Aschwanden et al. \(2007\)](#), MSs are an unlikely source for major coronal heating.

## 3.4 Conclusion

Now, let us summarise the general properties for the population of MSs (see Table 3.2). In general, the values presented here fall between those presented in [Bohlin et al. \(1975\)](#) and [Dere et al. \(1989\)](#). The more extreme examples, seen in [Bohlin et al. \(1975\)](#), are not found here. We find that the data in [Dere et al. \(1989\)](#) are conservative and we find maximum length and lifetimes which are larger.

Examining the individual regions, in which the MSs occur, it is evident that higher velocities are found in the coronal hole and coronal hole boundaries and so we consider the question of whether there might be a difference in the physics of formation to that in the quiet Sun. Examining the lengths, the coronal hole/boundary MSs are longer than those seen in the quiet Sun. Open magnetic field lines in coronal holes are the likely cause allowing the MSs to extend higher in these regions. We find little difference in the widths, and, examining mean lifetime values, we find percentage

differences from the total sample mean: 3.7% and 2.6% for quiet Sun and coronal hole boundary respectively, with a small increase in percentage difference of -5.3% for coronal hole MSs.

Upon examining the general properties and their relations to each other, we also find that the maximum velocity and maximum length are related, and, that the lifetime and maximum length show signs of correlation. However, the maximum velocity and lifetime appear to show little correlation with the current sample size.

A range of magnetic environments have been shown to yield MSs with different basic properties in some cases. This may be due to separate generation processes, although this is just a conjecture. The overlying solar environment is more likely to have an effect, either restricting or allowing extension, which would explain the comparatively longer MSs observed in coronal holes.

Considering the change of the properties over the sample time period, we find that the maximum length and lifetimes both show a general correlation with the sample time period. Whereas, the maximum velocity does not follow the same pattern, which is somewhat unexpected due to the maximum length being related to the maximum velocity. Consequently, one might expect the maximum velocity to increase as a function of the sample time period. At present we cannot offer any explanation as to why this is the case, but further modelling studies will hopefully reveal some answers.

We observe similar durations for regression back to the limb for the estimates and the recorded times. Clearly, there is a greater variance in the measured values compared to the estimates, but this is to be expected. The mean time for the tip to recede back to the limb is 7.5 min (estimated) and 6.6 min (recorded), which are similar, indicating that gravity is the dominating force behind their fall. This difference is not large enough to be significant, or draw any conclusions.

Lastly, let us estimate the energy required to generate the MSs. We incorporated the scale-height variations over the length of the macrospicule, such that, the density decreases from footpoint to tip. This was applied to take into account non-uniform density when estimating the centre of mass. We find that high scale-heights yield high energy requirements, which decrease with lower value scale-heights. Examining the mean macrospicule energy values for the scale-heights we obtain  $1.46 \times 10^{17}$  J,  $4.78 \times 10^{16}$  J,  $3.09 \times 10^{15}$  J,  $1.46 \times 10^{14}$  J and  $3.66 \times 10^{13}$  J for scale-heights of uniform and 25, 5, 1 and 0.5 Mm, respectively.

Our simple energetics model yields values for energy which are possibly too small, but are not unreasonable. If we compare these to energies calculated for wave-driven reconnection events in [Heggland et al. \(2009\)](#), of the order  $10^{17}$ - $10^{18}$  J, if the scale-height is around 10-25 Mm according to our estimates, the generation of

MSs may be feasible. However, this model generates jets of 1 Mm in length, a degree of magnitude away from our measurements. Models have been proposed, such as [Adams et al. \(2014\)](#), in which open magnetic field above a reconnection event allows the MSs to extend to the heights we observe.

It would be preferable to have 8-10 years worth of high-quality data to examine the possible changes in the properties of MSs over the solar cycle. Also, investigating the rotational speed of MSs, which is not possible without spectral information, would be feasible and would give additional insight. The use of modelling to understand these features further would also be of interest such that we might be able to understand how these features are generated.

Study	Bohlin et al. (1975)	Dere et al. (1989)	The present study
Max Length [Mm]	5.8-43.5	1.45-16.7 $\bar{x}$ :8.7	14.0-60.4 $\bar{x}$ :28.1
Width [Mm]	3.6-10.9	2.2-6.5 $\bar{x}$ :4.4	3.1-16.1 $\bar{x}$ :7.6
Lifetime [min]	8-45	>3	2.7-28.1 $\bar{x}$ :13.6
Max Velocity [km/s]	10-150	20-50	54.1-105.6 $\bar{x}$ :109.7
Count	25	10	101
Cadence [s]	> 180	20,60	12

Table 3.1 General properties table. Comparing the values given by Bohlin et al. (1975), Dere et al. (1989) and this study.

Magnetic Configuration	Velocity (km/s)			Length (Mm)			Width (Mm)			Lifetime (min)		
	Low	High	Mean	Low	High	Mean	Low	High	Mean	Low	High	Mean
Coronal Hole	58.3	181.3	113.4	17.3	60.4	31.9	3.1	13.0	7.2	7.8	28.6	13.5
Coronal Hole Boundary	66.8	194.8	107.4	16.1	60.4	30.5	4.0	16.1	7.9	9.8	22.0	14.0
Quiet Sun	62.8	154.3	101.2	14.0	45.3	25.6	3.4	12.6	7.8	5.6	24.0	13.5

Table 3.2 Properties associated with each region of the solar limb.



# **Chapter 4**

## **On relationships with an active longitude**

### **4.1 Introduction**

The behaviour of solar non-axisymmetric activity has been studied since the beginning of the last century [Chidambara Aiyar \(1932\)](#). It has been recognised that the distribution of sunspot groups is not uniform, they tend to cluster to a certain heliographic longitude [Balthasar and Schüssler \(1984\)](#); [Bumba and Howard \(1965\)](#); [?](#). These early studies of the active longitudes focused mainly on the distribution of sunspot groups or sunspot relative numbers. From the middle of the 20th century it has been suggested that not just the sunspot groups have a non-homogeneous longitudinal distribution. This inhomogeneity has been found in the case of solar flares [Zhang et al. \(2007\)](#), surface magnetic fields [Benevolenskaya et al. \(1999\)](#), heliospheric magnetic field [Mursula and Hiltula \(2004\)](#) and, recently, active longitudes have been observed in coronal streamers [Li \(2011\)](#).

Macrospicules (hereinafter: MS) are chromospheric objects observed in H $\alpha$  and He 30.4 nm [Bohlin et al. \(1975\)](#); [Murawski et al. \(2011\)](#); [Scullion et al. \(2010\)](#); [Wang \(1998\)](#). They are explosive jet-like features extending up to, on average, 29 Mm and velocities up to approximately 110 km/s [Zaqarashvili and Erdélyi \(2009\)](#). Their structure reflects the solar atmosphere they move through, they are proposed to have a cool core, surrounded by a hot sheath [Parenti et al. \(2002\)](#). They are of particular use in this study, as they are observed from the solar equator to the poles.

In this chapter we study the longitudinal and latitudinal spatial distributions of MS. Furthermore, we will explore the relationship between the sunspot groups, non-axisymmetric behaviour or Active Longitude (hereinafter: AL) and longitudinal distributions of MS.

## 4.2 Observations and Databases

The MS were observed using the 30.4 nm spectral window AIA on-board SDO (Solar Dynamic Observatory) [Lemen et al. \(2012\)](#). This takes a  $4096 \times 4096$  pixel, full disc, image of the Sun at a cadence of 12 s. We took typical samples of two hours, twice a month, from June 2010 until December 2012. For each image the solar limb was flattened out, making it easier to identify and measure the MS. They are extremely difficult to measure on disk and as such this study concentrates on those occurring at the limb. We record the time at the moment they become visible at the limb and their angular displacement from solar due east. Measuring MS this way we identified 101 examples of MS. The physical dimensions and the heliographic coordinates have been estimated.

The source of sunspot data that we use to calculate the most enhanced longitude of sunspot groups (AL) is the Debrecen Photoheliographic Data (DPD) sunspot catalogue [Győri et al. \(2011\)](#). This database is the continuation of the classic Greenwich Photoheliographic Results (GPR), the source of numerous works in this field. The sunspot catalogue has been used, providing a time sample from 1974. This data sample contains information about area and position for every sunspot.

## 4.3 Statistical Study of the Latitudinal Distribution of MS

To study the latitudinal spatial behaviour of MS as a first step, we determine the heliographical latitudes ( $B$ ). For further analysis, the Carrington latitudes,  $B$ , have

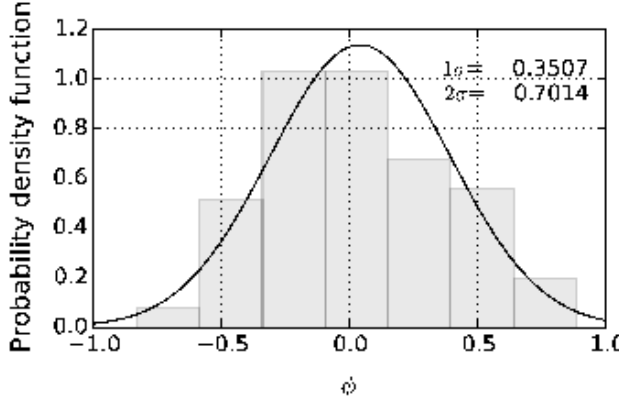


Fig. 4.1 The gray area shows the probability density function of the parameter  $\phi$ . The solid black line is the fitted Gaussian distribution. The values standard deviation  $1\sigma$  and  $2\sigma$  of the normal distribution have been indicated in the top right corner.

been transformed, into the following system:

$$\begin{aligned}\phi &= -(B + 90^\circ)/90^\circ, B < 0 \\ \phi &= -(B - 90^\circ)/90^\circ, B > 0\end{aligned}\quad (4.1)$$

The domain of interest of the quantity  $\phi$  is  $[-1; 1]$ . The  $\phi = 0$  point contains the northern and southern poles. The  $[0; 1]$  sub-domain of  $\phi$  represents the northern hemisphere, the ascending  $\phi$  values from 0 to 1 show the descending latitudes from  $90^\circ$  to  $0^\circ$ . The southern hemispheres have been considered in the same way.

Figure 4.1 shows the result of the statistics above. The histogram depicts a normal distribution. The mean of the distribution is  $\bar{\phi} = 0.043$ , suggesting that most of the MS tend to cluster to the poles. We also found that the northern hemisphere was a slightly more active in this time period. The standard deviation  $1\sigma = 0.3507$  and  $2\sigma = 0.7014$ . Hence, 68% of the data tend to cluster in a  $31.5^\circ$  wide belt from the poles. That is to say: 68% of MS are between the  $\pm 58.5^\circ$  and  $\pm 90^\circ$  heliographic latitude, and, 95% of MS are in a  $36^\circ$  degrees belt from the poles or between the  $\pm 27^\circ$  and  $\pm 90^\circ$  in heliographic latitude. Therefore, MS are able to exercise longitudinal inhomogeneity at higher latitudes.

## 4.4 Statistical study of longitudinal distribution of MS

### 4.4.1 Activity maps of active longitudes based on sunspots

According to our previous study ([Gyenge et al., 2014](#)) the active longitudes' identification method have been considered and the active longitude was found to be distinct in each hemisphere. The present investigation started with a similar method as described in our preceding paper ([Gyenge et al., 2012](#)). The areas and positions of all sunspot groups are considered. The solar surface is divided into longitudinal bins of  $20^\circ$  and the areas of all groups were summed up in each bin:  $A_i$  in certain Carrington Rotation (CR) between 2097 and 2128, which is the time interval of the MS sample. Next, the longitudinal activity concentration is represented by the quantity  $W$  defined by,

$$W_{i,CR} = \frac{A_{i,CR}}{\sum_{j=1}^N A_{j,CR}}, \quad (4.2)$$

where  $N$  is the number of bins,  $\sum_{j=1}^N A_{j,CR}$  is the sum of all sunspot groups in a given CR and  $A_{i,CR}$  is the total area of sunspot groups in a CR and at a specific longitudinal bin.

In each CR we omitted all of the  $W_{i,CR}$  values which are lower than the  $3\sigma$  significance limit. The highest peak,  $AL_{CR}$ , has been selected from this decayed sample (which contains only the significant peaks) caused by the significance test. For further analysis, the Carrington longitudes,  $\lambda$ , will now be transformed, into Carrington phase period:

$$\psi = \lambda / 360^\circ. \quad (4.3)$$

Hence, the values of the phases are always smaller or equal (which is the entire circumference) than one.

The time-variation of the parameter  $AL_{CR}$  is plotted in Figure 4.2. The vertical axis is the phase parameter, which has been repeated by 3 times. The northern (left-hand-side) and the southern (right-hand-side) cases are considered separately. Both figures unveil a clear increasing migration pattern. [Gyenge et al. \(2014\)](#); [Usoskin et al. \(2005\)](#) found similar patterns at a different time interval. Most of the migration follows a parabola shape (which has been fitted by the least-square method).

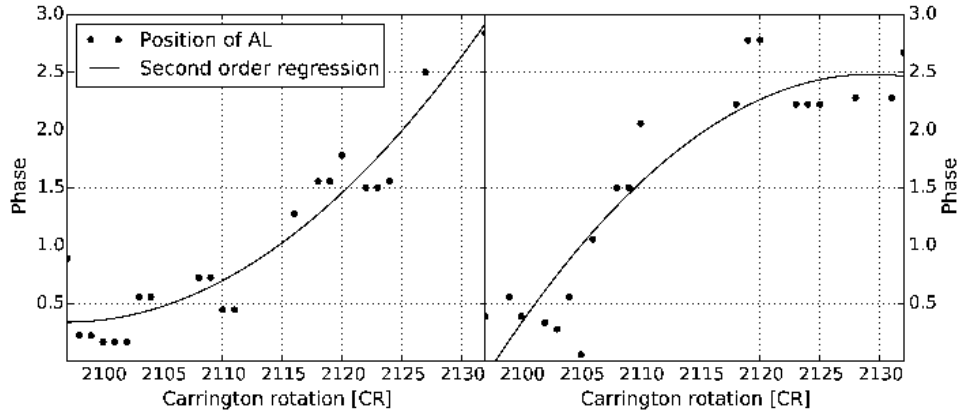


Fig. 4.2 The migration of the active longitudes in the time interval of CR 2097 to 2128 based on sunspot groups. The left panel shows the northern hemisphere. The right panel is the southern hemisphere.

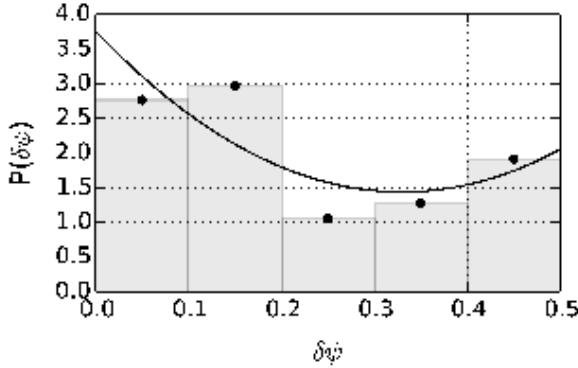


Fig. 4.3 Density distribution of the  $\delta\psi$  parameter.

#### 4.4.2 Relationship between the AL and MS longitudinal distribution

The parameter  $\delta\psi$  is now introduced to study the relationship between the active longitude  $AL_{CR}$  defined by sunspot groups, and the longitudinal position of MS  $L_{CR}$  in CR.

$$\delta\psi = |AL_{CR} - L_{CR}|. \quad (4.4)$$

The parameter  $\delta\psi$  has been reduced by a unit phase if it is larger than 0.5, which means this quantity represents the shortest phase difference between the longitudinal position of a given MS and the position of active longitudes in both hemispheres. For further analysis, the  $\delta\psi$  samples of the northern and southern hemispheres are

now combined.

The probability density function (PDF) of the quantity  $\delta\psi$  is shown in Figure 4.3. On the  $x$ -axis the meaning of the lower values reflect on the smallest longitudinal difference in phase, the value 0.5 phase jumps to the opposite side of the Sun.

The MS tend to cluster near the active longitudes, which is shown by the first and second peaks:  $\delta\psi < 0.2(< \pm 36^\circ)$  61 % of the candidates. However, there is a significant peak around 0.5, which is the signature of the appearance of secondary longitudinal belts. The secondary belt exists always at the same time as the primary. Note that the latter is always stronger than the secondary belt, and the phase shift is around 0.5. The MS show a similar behaviour. A secondary belt appears for the 22% of the events and  $\delta\psi < 0.1(< \pm 18^\circ)$ .

## 4.5 Summary

We investigated the distribution of MSs detected at the solar surface as function of their longitudinal and latitudinal coordinates in Carrington coordinates.

A non-homogeneous latitudinal macrospicule distribution has been found. Most of the events tend to cluster to the higher latitudes (95% of MS are with in the  $\pm 27^\circ$  to  $\pm 90^\circ$  heliographical latitude). The number of the events is found to be growing exponentially from the equator to the pole in both hemispheres. A slightly asymmetrical behaviour has been found between the two hemispheres in the studied time interval, where the northern hemisphere was marginally more active than the southern.

The latitudinal spatial distribution of MS is not uniform either. A large proportion of the MS (83 of from the 101 in our sample) tend to cluster to the AL. In the case of the primary active longitude belt, the MSs are within  $\pm 36^\circ$  degrees of the active longitude. The secondly belt has a  $\pm 18^\circ$  wide range where the MSs are found to be concentrated. This supports the existence of an active longitude at higher latitudes.

A large sample and more comprehensive statistical study is now in preparation for a more detailed search for further identifiable non-homogenous longitudinal distributions of MS in the entire time period covered by observations of the SDO satellite.

# Chapter 5

## A detailed case study of a jet-like feature at the limb

### 5.1 Introduction

Solar jets of various forms are ubiquitous throughout the solar atmosphere, from spicules and MSs low in the chromosphere, both of which pass through the transition region, to coronal and X-Ray jets extending into the solar corona [Archontis and Török \(2008\)](#); [Madjarska \(2011\)](#); [Morton \(2012\)](#). Investigations into these phenomena have advanced significantly with recent developments in solar telescope technology, applied on missions like Hinode and the Solar Dynamics Observatory (SDO) and the most recent mission Interface Region Imaging Spectrometer (IRIS). Features are observed in a range of wavelengths and heights in the atmosphere [Wang \(1998\)](#); [Yamauchi et al. \(2004\)](#).

Low in the chromosphere the predominant feature is the spicule, these small scale jets are generally found forming over inter-granular lanes and reaching heights of 1 - 5 Mm. They are also very short lived, lifetimes generally only reaching 10 mins. More importantly there is currently debate as to whether the population of spicules is divided into two forms, Type-1 and Type-2. Type-1 are described as longer lived and less explosive with respect to velocity, whereas Type-2 reach higher velocities and higher into the atmosphere, however, are not observed to fall back into the chromosphere [Beckers \(1972\)](#); [de Pontieu et al. \(2007\)](#); [Sterling \(2000\)](#).

Having stated this, [Pereira et al. \(2014\)](#) have revealed that Type-2 spicules disappearance may be as a result of heating and moving out of the passband, due to the fact that they are consequently observed in a hotter line which may imply that these features are not in fact separate populations and [Zhang et al. \(2012\)](#) finds no such distinction in population.

Many formation mechanisms have been proposed for spicules, including reconnection, *p*-mode driving and applying accretion disk models in a solar context, for reviews see [Sterling \(2000\)](#) and [Zaqarashvili and Erdélyi \(2009\)](#). More recently, the question surrounding spicules is how they effect the atmosphere is particularly pertinent given their vast number. Any contribution in terms of solar wind acceleration or heat transfer would be scaled up by their sheer number density. [Rouppe van der Voort et al. \(2015\)](#) used coordinated observations with SST and IRIS to study RRE's and RBE's, examining H $\alpha$ , Mg II h & k, C II and Si IV. The authors find that these spicule-like extensions observed in H $\alpha$  have counter parts in the hotter Magnesium lines and the upper chromosphere/transition region C II and Si IV, which would certainly imply that these features are heating themselves, or the atmosphere around them. These spicules are similar to other features such as surges, the already mentioned RRB's/RBE's and chromospheric jets, all of which need considering with respect to spicules [Kuridze et al. \(2015\)](#); [Tsiropoula et al. \(2012\)](#).

Higher in the chromosphere, MSs are generated, despite their origin laying low in the chromosphere, MSs extend through to the transition region and into the corona. Larger counterparts of spicules, initially observed in 1975 by [Bohlin et al. \(1975\)](#) using the Skylab 2 mission using a He 30.4 nm filter viewing the upper chromosphere. Bohlin stated their lifetimes to be 5 to 30 mins and lengths to be approximately 10 - 50 arcsec, and these values have been confirmed Chapter 3

Macrospicules are generally accepted as multi-thermal structures, featuring a cool core and a hot sheath resulting from formation in the cooler atmosphere, from being observed in H $\alpha$  ([Labonte, 1979](#)) and hotter high chromosphere lines such as in [Parenti et al. \(2002\)](#). They have also been observed to rotate, [Pike and Mason \(1998\)](#) and [Kamio et al. \(2010\)](#), the latter paper quotes  $-120 \pm 15 \text{ km s}^{-1}$  blue shift Doppler velocity on the left side of the macrospicule.

There are multiple proposals for the mechanism triggering apparent rotation of the macrospicule. [Curdt and Tian \(2011\)](#) propose that the Sun's differential rotation causes MSs rotation, whereas, reconnection events cause the relaxation of a small-scale twisted loop, as demonstrated by [Adams et al. \(2014\)](#). Again, with MSs extending high into the atmosphere, the question of their effect upon it, is one that needs answering. [Pike and Harrison \(1997\)](#) observe outflows from the macrospicule of the order  $200 \text{ km s}^{-1}$  in He I and discuss whether these outflows could potentially accelerate the solar wind. However, work by [Zaqarashvili et al. \(2014\)](#) questions whether jets moving at super-Alfvénic speeds might cause a Kelvin-Helmholtz instability to form at the macrospicule/atmosphere boundary, which would, in turn, transport heat into the corona.

A third category of jet-like features, are coronal jets, observed in slightly hotter lines of 17.1 nm but still visible in EUV, such as those discussed in [Shibata et al. \(1992\)](#) and simulated in [Wyper and DeVore \(2016\)](#). [Shibata et al. \(1994\)](#) propose that these jets are reconnection events, where reconnection is triggered by flux emergence at the base of a small-scale loop. However, after this initial reconnection, there are several models as to how the system evolves. [Moore et al. \(2010\)](#) demonstrate a dichotomy in formation mechanism of coronal jets, between the standard 'inverted Y' model by Shibata and the blow-out jet model. The blow-out model differs from the standard model due the reconnection leading to a 'curtain' of plasma flow as opposed to the 'spire' from the standard model. The difference between the two models originates in initial configuration of the overlying arch. In standard jets the arch has no appreciable shear, whereas for a blowout jet the arch is twisted and sheared sufficiently to drive the explosive outflow which forms the jet. Coronal jets have also been shown to accelerate particles into interplanetary space [Li et al. \(2011\)](#) and there is also evidence for repeat onset jets, with several re-occurrences, [Chifor et al. \(2008\)](#) demonstrate repeat onset set of jets driven by flux cancellation.

Lastly, we need to consider X-ray jets. [Shimojo and Shibata \(2000\)](#) define their physical properties studying 16 separate jet events. Due to limitations on instrumentation at the time, the authors do not cover the extent of the jets, however, they analyse temperatures, 3–8 MK, and density,  $0.4\text{--}4.0\text{ cm}^{-9}$ . The authors also discuss flaring at the foot-point of X-ray jets, in that, the temperature is proportional to the size of the initial footpoints.

[Kamio et al. \(2010\)](#) applied a great deal of the background above when studying a macrospicule and X-ray jet forming simultaneously. There is also discussion in [Pike and Harrison \(1997\)](#) and [Kim et al. \(2007\)](#) on the appearance of X-ray jets, alongside small scale jets.

In the following sections we comprehensively discuss the physical properties of a case study. In Section 5.2 we present the observations we are using. 5.3 discusses the evolution of the jet with respect to its extent and the different view of the feature utilising STEREO-A's EUVI. Then move on to a doppler analysis of the jet in Section 5.4. Lastly, attempt to quantify the effect of the jet on the atmosphere in Section 5.5 before making our conclusions.

## 5.2 Observations

We observed a jet-like (hereby referred to as 'the jet') feature at the limb on 21st June 2016 beginning at 07 : 30 : 00 in CRISP, an instrument installed on the Swedish Solar Telescope (SST) during a period of good seeing, [Scharmer et al. \(2003\)](#). We used the

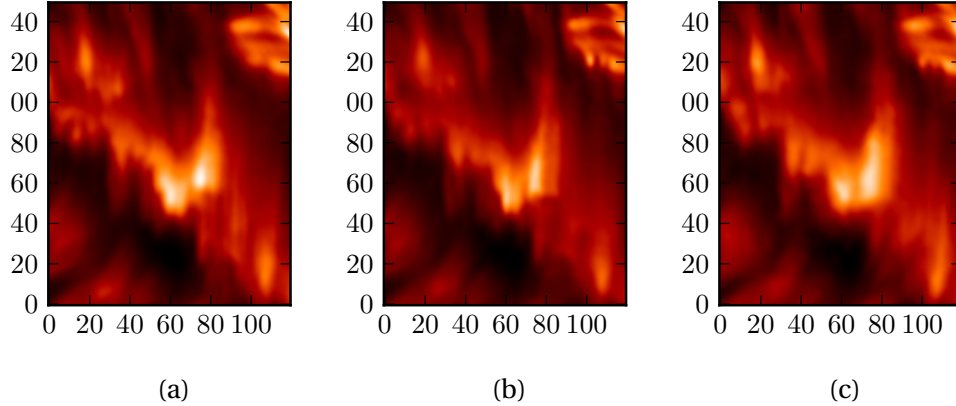


Fig. 5.1 a) Observe the two bright points in the proximity of (79, 60). The point on the left is significantly brighter than the fainter on the right. We emphasise that the brightening around (60, 50) is not a contributor to this jet. b) In this frame the bright points have extended, the fainter point has now extended up to 95 and the core of the brighter left feature has grown with it. c) At this point the two separate points are now indistinguishable and the feature is now extending as one column.

$\text{H}\alpha$  filter, core line 656.28 nm with 35 slit increments from the core covering a .32 nm range,  $-0.2$  and  $+0.12$ , further processed using te Multi-Object Multi-Frame Blind Deconvolution (MOMBFD [van Noort et al. \(2005\)](#)). The observations were of Active Region 11506 with  $xc = 893''$ ,  $yc = -250''$  in heliographic coordinates on 930x930 pixel images, with spatial resolution of 0.012 arcsec/pixel and temporal resolution of 7.5 sec. Due to the constant surveillance under which we have the Sun, we also have simultaneous observations with the Solar Dynamic Observatory (SDO) and the Solar Terrestrial Relations Observatory (STEREO).

Using the Atmospheric Imaging Assembly (AIA), we observe the jet in most of the wavelengths available, 30.4, 35.5, 211, 17.1 and 13.1 nm. AIA on-board SDO ([Lemen et al. \(2012\)](#)) provides  $4096 \times 4096$  pixel images with a spatial resolution of 0.6 arcsec per pixel and a cadence of 12 sec.

Lastly, we also have observations in STEREO using the Extreme Ultra Violet Imager (EUVI) [Defise et al. \(2001\)](#). We are fortunate that when these observations were taken, STEREO A was at approximately  $90^\circ$  to the Sun-Earth line, as such we also have observations of this feature as an on-disk feature. In this case we are using the 30.4 nm HI instrument, however, the distance from the Earth has now reached a point that the temporal cadence has reduced to 10 min. While this is possibly too high to undertake a detailed examination, we can certainly utilise this method to inform us as to the global behaviour of the macrospicule. As we have a suite of observing instruments to utilise we aim to build a comprehensive description of this

feature and how it may affect the environment around it.

## 5.3 Time-Distance Evolution

Let us begin with the evolution of the jet over time. We have utilised a self-built, manual, feature measuring tool, which uses a clicking mechanism to select the foot and tip of the macrospicule, calculates the half height and uses this as a guide to measure the width of the feature. Using this tool on each frame, and therefore the time cadence of the instrument, we obtain the evolution of the jet and general ballistic information. We have used this tool on each wavelength to examine the extent upwards through the corona. Observations in SDO record the entire lifetime of the feature, however the same is not true for observations using the SST, where the observation window in SST closes at 07 : 55 : 00.

### 5.3.1 Onset

The jet feature is observed as it forms using SST and, fortunately, we can resolve initial stages of the jet formation. The jet is observed to initiate in the core of H $\alpha$  with two small bright points forming, and an ensuing jet developing above it. Figure 5.1 captures the early evolution of the jet in detail. Evident in Figure 5.1a we find the initial two bright points at the foot of the jet, the bright point of the left being significantly brighter than its counterpart on the right. By Figure 5.1b shows the development of these two points *i.e.* have now become two columns of brighter plasma. In the final formation stage, Figure 5.1c the jet has formed and is now a distinct feature against the background. This behaviour is in keeping with the standard jet formation model demonstrated by [Shibata et al. \(1992\)](#), where the authors describe an 'inverted y' shape of brightened material that is a result of small scale flux emergence reconnection.

### 5.3.2 Evolution

Let us examine the raw evolution of the jet in the time distance plot in Figure 5.2a. Here we have utilised the measuring tool to measure the extent of the feature in all the wavelengths in which it is visible. We find that the overall profile of its evolution contains two distinct peaks in most wavelengths, with the exception of 17.1 nm. The first peak comes at 07 : 37 before a decrease in size and subsequent secondary expansion to its maximum length in H $\alpha$  and 30.4 nm at approximately 07 : 49. This strongly implies that there is a second initialising type event in which a new material

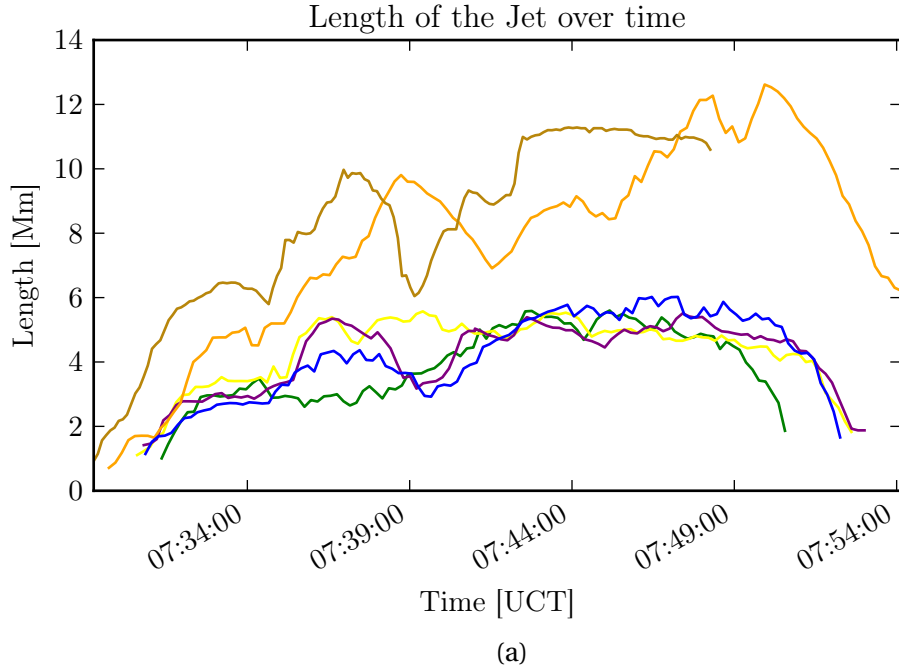
is accelerated into the atmosphere. As such let us turn to the CRISP instrument again.

With its higher resolution, a slit based analysis of the jet can be observed in ???. Notice two distinct curves in the image, the first onset is at approximately 17 and the second at a bright point originating at 85. We find that in this second phase of the jet, plasma extends higher into the atmosphere. This result is unusual as previous observations of recurrent jets have shown decay in subsequent initialisation events in observations such as [Jiang et al. \(2007\)](#). Unfortunately, a section of material is in front of the base of the jet and obscures our view of the second event.

Considering the observations in multiple wavelengths, we notice the smaller extension visible in the coronal wavelengths. In these higher temperature lines, the jet appears as a dark line. Now, this could be due to the fact that the feature is cool and can't be found in the higher temperatures. However, when examining the jet in AIA 30.4 nm, the feature appears dark beneath the limb but emissive over it. It also appears in EUVI 30.4 m, as a dark feature, therefore we can't assume there is no emission in the higher lines. This is not unexpected, given its extent in the chromospheric lines, we can categorise this as a chromospheric feature, as opposed to coronal.

Evidently, the maximum extent of this feature is in SDO 30.4 and maximises at 12.6 Mm although the measurements in H $\alpha$  may exceed this were it to be fully visible. Interestingly, the length of the jet in the coronal lines does not get larger after the second injection on plasma occurs. This subsequent acceleration of plasma originates from the same location as that of the initial formation, and on the same scale as the first onset. However, this drives the tip of the jet even higher than the initial tip, measuring the velocity accurately is difficult, due to this acceleration is set against the previous bright material. An approximation using multiple image steps and using a difference delta produces an average of  $46 \text{ kms}^{-1}$ , therefore we can infer that it reaches a higher maximum velocity than the first ejection.

The feature is very thin, averaging 1.13 Mm in H $\alpha$  and 0.787 Mm in He II. This result is unexpected, it certainly seems to contradict the cool core surrounded by a hot sheath model. However the errors on the measurement in SDO/AIA recordings are  $\pm 1.5 \text{ Mm}$ , when taking into account human measurement error and resolution of the instrument. Where as measurement error on the CRISP/SST images is  $\pm 0.0885 \text{ Mm}$ , thus, we are more inclined to believe the measurement according to CRISP. This thin spire is an expected outcome of the standard model of jet formation, more on which later.



(a)

Wavelength, nm	Maximum Length, Mm	Maximum Velocity km/s
656.2	11.3	0.09
30.4	12.6	31.5
33.5	6.0	53.6
21.1	5.5	50.1
17.1	5.6	51.9
13.1	5.6	36.6

(b)

Fig. 5.2 a) Darkgold = H $\alpha$ , Blue = 33.5 nm, Orange = 30.4 nm, Purple = 21.1 nm, Yellow = 17.1 nm, Green = 13.1 nm. The CRISP observations end earlier than the whole evolution of the jet, and the top of the jet is cut off by the top of the image. Therefore we ignore flatline at the top of the H $\alpha$  line starting at 07:42. b) Table of maximised basic spatial properties of the jet.

### 5.3.3 STEREO-A

We are fortunate that we can observe the jet feature in the STEREO-A/EUVI, with the position of the spacecraft at approximately 90° to the Sun-Earth line. This facilitates the building of a larger picture of the behaviour of the jet, the downside to this however, is that with STEREO-A being at such a distance the cadence is low, 10 mins. In this case we obtain 4 images in 30.4 nm in which the jet is observed. The jet appears as a dark fibril like feature originating at \*\*\*A POINT IN SPACE\*\*\* and extending across the disk to a length of 45.1arcsec. Significantly, the component of

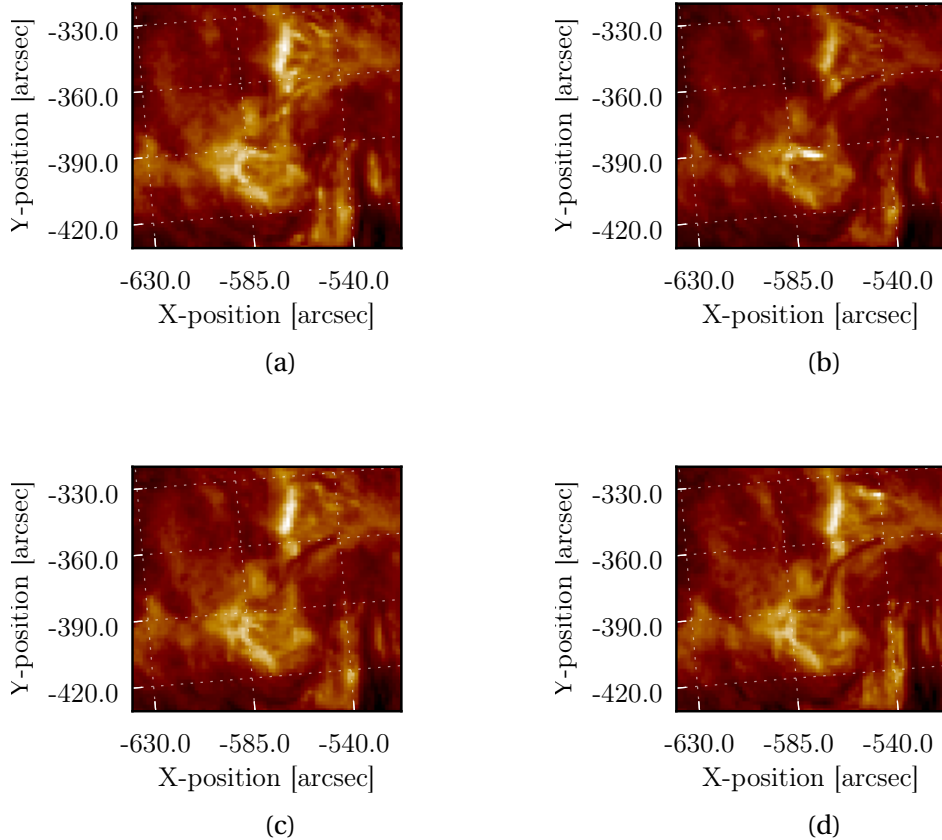


Fig. 5.4 EUVI 30.4 nm images from STEREO on 21st June at a) 07 : 26 : 15, b) 07 : 36 : 15, c) 07 : 46 : 15 and d) 07 : 56 : 15.

extension in the East-West direction is not insignificant, approximately 30 arcsec. With this information we calculate that the total length of the feature, taking into account both SDO and STEREO's view, is 25.5 Mm.

## 5.4 Doppler shift

Possibly the most valuable information to be gained about the development of jets, is pertaining to its rotational behaviour, therefore, we will use the spectral increments from the CRISP instrument to obtain line-of-sight Doppler velocities. There is, however, a hindrance with this. There are two separate forms of the emission spectra within the image. The region where the jet initialises, is on disk, and as a result the spectral analysis reveals an absorption spectra.

### 5.4.1 MCMC Method

We have developed this algorithm to address this particular problem, using the overall shift of the emission line from the standard emission. Over the limb, however, the spectral profile changes to emission and we find two peaks. As a consequence of this, finding the total shift away from the core, 656.28 nm, is made more complex. For pixel points which are on-disk, we fit a single Gaussian and calculate the minima, as is standard, and for the two peak spectra, we have utilised a double Gaussian, finding the minima between the two. However, the problem becomes evident when we need to change between the two routines.

We have utilised a Markov Chain Monte Carlo (MCMC) ([Richey \(2010\)](#)) method to find the most accurate fit and the Bayesian Information Criterion (BIC) to test which of the two fits is most appropriate from a given line as a solution to this problem.

This method takes the 35 spectral intensity for a given pixel and samples multiple possible fits for the profile these produce. We then find the most likely fit from this range and minimise this final fit to find the mean value of the fit. Difference between the original core value and mean of the new fit is the calculated shift in wavelength, and therefore, the line-of-sight velocity for the chromospheric plasma. The process is the same for both single and double Gaussian fitting and as such we apply a BIC to test which fit is more appropriate. BIC has limitations when the number of parameters is of the same order of the size of the sample and differentiating between multiple complex models. In this case the sample is larger than the number of parameters and we are only testing two possible models, as such, we can use the test with confidence in the results.

The result of applying the above method to the CRISP/SST spectroscopic dataset is presented in Figure 5.5. Immediately apparent, is the banding structured red and blue shifts, the effect is created as a result of the optical depth created when observing at the limb. The jet forms in amongst a blue band of smaller thin structures, making early observations in the dopplergrams difficult.

### 5.4.2 Analysis

This particular feature, as has already been mentioned, has two events in which material is accelerated upwards into the solar atmosphere. The first event is not readily visible in the dopplergrams, difficult as it is to pick out against a line of spicule-like features all showing blueshifts, towards the vieweing direction. This result is to be expected given the we have demonstrated movement away from the 'camera' in Figure 5.4. Whereas, the second expulsion of material, originating at 07:

37, exhibits the classic behaviour of a rotating feature in dopplergrams, a red/blue split over the body of the feature.

It is clear that the second event comes from a similarly small element to the first and evolves upwards, joining the full formation of the jet, hence why the apparent rotation of the jet does not appear to spread across the rest of the jet as seen in H $\alpha$ .

As the jet evolves we see an initial blue shift, matching the acceleration upwards seen in H $\alpha$ , and it is only after a few second seconds of evolution that rotational behaviour begins to become evident. The first panel in Figure 5.5 at 07 : 37 : 44 demonstrates the first panel where there might be an inkling of redshift on the right ride of the feature, with a thin line registering as moving away from the camera. Noticeably, this rotation does not begin at the base of the feature, instead, the rotation manifests from the tip downwards over the next two images at 07 : 37 : 51 and 07 : 37 : 59.

By the time the jet reaches 07 : 39 : 07, we begin to observe a thin formation of red shift at the right side of the base of the feature, and by 07 : 38 : 15, the red-shift has entirely taken over the right hand side. Though once again, the next frame shows progression up the spire of the feature.

We subsequently observe the shift to disappear from the right hand side of the jet, however, the subsequent two images show an element of red shift now on the left of the feature. This element consequently develops into longer feature in 07 : 38 : 53 and subsequent images, to the point where red shift now dominates the left hand side of the feature.

This is a result of the magnetic pressure acting as restoring force, and rotating the feature in the opposite direction. However in this case, not to the same magnitude, an expected outcome due to inherent loss of energy from the system. By the last panel at 07 : 39 : 16, the feature has returned to a 'neutral' state, as such we can estimate an approximate period of a minute and a half.

This behaviour is extremely interesting as it demonstrates a torsional motion of the entire body of the feature, with the structure rotating anti-clockwise and then clockwise. This is a result of the release of magnetic tension in the initial reconnection event causing an unwinding of the inherent twist in the initial loop. We suggest that, as a result of the speed of the initial acceleration of the plasma material, this untwisting began at the top of the plasma column as is seen in 07 : 37 : 51. The peak of this untwisting, when the red shift dominates the RHS at 07 : 38 : 15, with the highest velocity values observed at approximately 3 – 4 kms $^{-1}$  and the 'body' of the feature demonstrating velocities in the range 1.0 – 1.5 kms $^{-1}$ .

The velocity values given here are slow compared to those presented in previous works, however, we believe these to be accurate, and attribute this to the small scale

of the initial loop. A larger scale loop would mean that the magnetic tension would be greater, and hence, experience greater restoring force, inducing higher velocities.

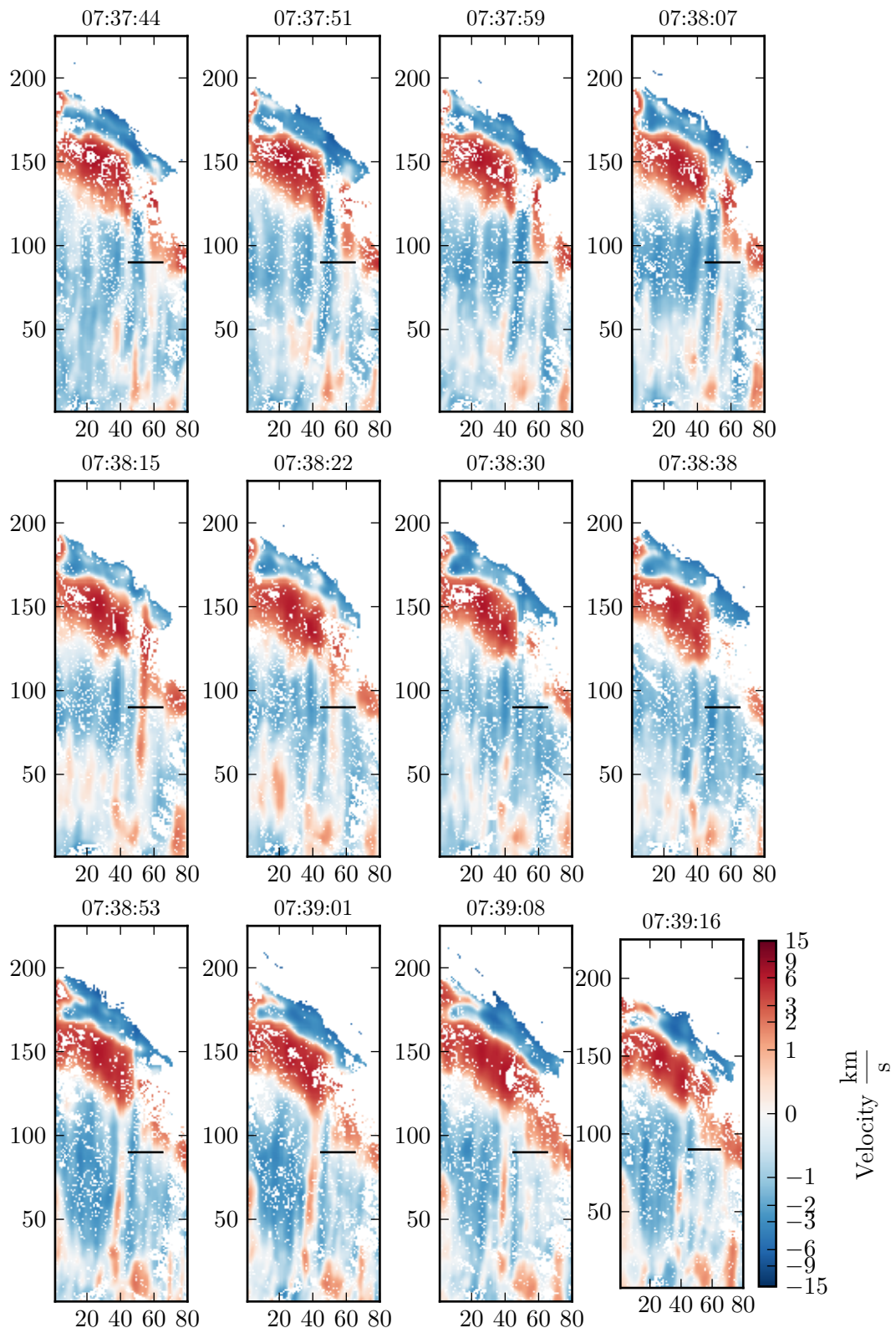


Fig. 5.5 Above is the result of the dopplergram processing during the evolution of the second ejection of plasma starting at 07 : 37 : 00. All images shown in pixel coordinates.

## 5.5 Effect on the atmosphere

With the increased resolution we can visually inspect the boundary between the jet and atmosphere. Figure 5.6 details the evolution of the jet in the core of H $\alpha$  in over 115 seconds. At the boundary we observe narrow dark columns in the emission on either side of the jet. Given that they appear on either side of the jet column and that the observations are in the core of the H $\alpha$  line, it is unlikely that this would be caused by a doppler-like effect. One possibility is that the cause is an instability effect, such as shear or Kelvin-Helmholtz, seen in [Zaqarashvili et al. \(2014\)](#) as the jet moves throughout the higher atmosphere. Supporting this hypothesis is that these images were recorded in the 'second phase' of the jet *i.e.* after the second reconnection and the jet extends to its peak in 30.4 nm. As such, it is possible that these columns are a result of plasma being accelerated through the less dense atmosphere.

One of the possible primary results of these instabilities is a dissipation of energy into the surrounding atmosphere, as such we might expect an increase in temperature of the surrounding atmosphere. To this end we will utilise the temperature calculation method highlighted in [Leonard and Morgan \(2014\)](#).

The authors use a Differential Emission Measure (DEM) to obtain a temperature response from the SDO/AIA measurements. The temperature response is a combination of the wavelength response from the instrument and the contribution function which describes the emission from a given temperature. When using such a scheme, we need to decide on a general DEM profile to be applied to all pixels. The method uses a Gaussian scan across the emission in each line and property of the Gaussian; mean, amplitude and width. Utilising a narrow Gaussian seems to provide the most accurate values when compared to synthetic observations.

Figure 5.7 demonstrates the behavioural change of the temperature across the normal of the feature by slit based analysis. By performing this analysis over the time domain of the second ejection of plasma material, we will ascertain whether the feature has any impact on the atmosphere. The difficulty with this form of measurement is that the feature itself is not particularly wide, 1 Mm, and therefore has only one or two pixels of actual jet material for us to examine. The jet is located around the 3rd and 4th pixels of the x axis, and as we would expect we see a moderate dip, when compared to the surroundings. Noticeable as well, however, is that at what is approximately the boundaries, there is a peak in temperature, before it drops as distance increases with respect to the jet.

These values are not conclusive, we require temperature maps on a much finer spatial scale, and as well, new techniques to develop to overcome the problems

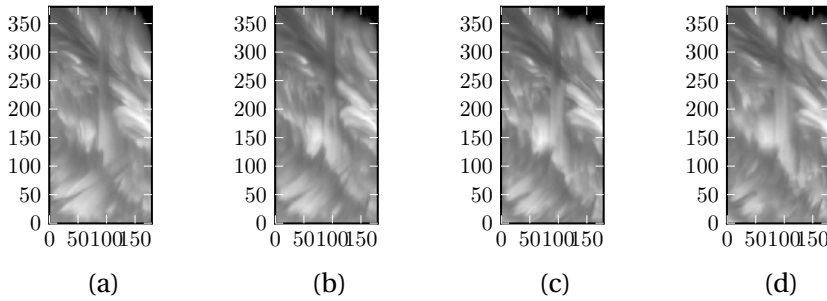


Fig. 5.6 Sequence of images detailing an intermediate phase of the jets evolution. Begginning with a) 07:36:19, b) 07:36:19, c) 07:37:36 and d) 07:38:15

of the extremely broad H $\alpha$  and He II lines causing a blurring of possible values. However, in conjunction with the observations presented here of possible shearing or Kelvin Helmholtz instability causing a lack of emission at the boundary of the jet, we can present the hypothesis more confidently. In terms of the bigger picture in which spicules/jets/MSs contribute to heating of the solar corona, the results produced by this feature are not typical. With respect to other studies, this feature cannot be considered that quick, or large, or excessively rotational, yet it may be having a measurable effect. Hence, applying this kind of comprehensive analysis to multiple jets, particularly rapidly evolving examples, to ascertain their impact on the atmosphere fully is the next area of investigation for these jets. An endeavour which will be aided significantly by the operation commencement of DKIST, with its superior everything.

## 5.6 Discussion & Conclusion

We observe a jet-like feature at the solar limb on 21st June 2012 at 07 : 30 : 00 on the solar limb, centred at 910, 234 solar x and y. We have multiple methods with which to view the feature, CRISPT/SST, the range of AIA/SDO coronal wavelengths and SECCHI/STEREO-A. We have utilised multiple analysis techniques to build a comprehensive picture of the jet-like features motion and the possible impacts on the atmosphere above it.

From the observation of this feature, we can draw the following conclusions

- This particular feature is visible in H $\alpha$  and He II 30.4, and thus, is inherently a chromospheric object.
- The jet has two separate ejections of material. Reaching a maximum *length* of 25 Mm

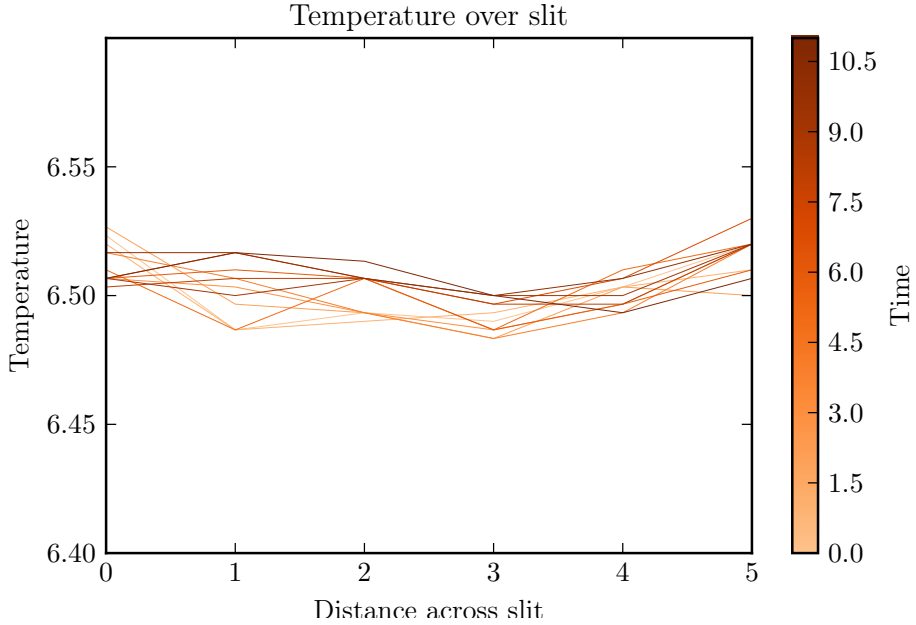


Fig. 5.7 The AIA maps were processed into temperature maps, and a slit was taken at the half height, perpendicular to the axis of evolution. The temperature maps were taken for the time over which the second acceleration of material occurred. The colorbar indicates the passage of time and the various lines applicable to the slits is demonstrated.

- The formation of the jet is observed to be similar to the standard jet formation mechanism.
- The jet has a rotational component to its motion

The feature is observed to extend to 12.6 Mm in He II 30.4 nm (and is only found to be shorter in H $\alpha$  due to moving out of the viewing field of view). Its lifetime is measured to be 20 mins and radial velocities are found to be maximised during the initial acceleration, and are of the order  $50 - 60 \text{ kms}^{-1}$  during the first acceleration of the feature. However the second acceleration of material proves awkward to measure accurately, however we estimate slightly higher maximum velocities, but similar averages over the extension upwards. This very much puts this feature in the category of MSs, agreeing with the values presented in Chapter 3.

However the feature exhibits similar formation mechanisms as a standard jet following the pattern demonstrated in [Shibata et al. \(1992\)](#) and then built on by [Moore et al. \(2010\)](#), who also presented the blowout jet mechanism. With the two visible bright points in the H $\alpha$  images which come to form an, all be it, long thin bright arch before forming the characteristic spire of a the standard jet. Unfortunatley, Hinode's XRT instrument was in a power down mode during the formation of this feature and

RHESSI did not record the event, as such, we are missing crucial X-ray data.

If an increase in the X-ray radiation were to be found, the question as to the categorisation of such a feature becomes important. Given that we observe several of the key indicators of a standard jet, could this not also be classified as a standard jet? Inspite of this features relatively small size, this could be classified as an X-ray jet. However the question remains, is this a macrospicule? And if so, do we classify the feature as a macrospicule or a standard jet?

One possible differentiator is the appearance in the higher coronal wavelengths. In this case, the jet appears as an absorption feature, against the brighter limb. This does not mean that the jet does not reach coronal temperatures, in 30.4 nm the jet appears as absorption below the limb and as emission above it. We cannot conclusively say that the jet contributes to the coronal emission by visual inspection.

Therefore, we propose that this is a standard jet, and as a community, we need to fully address the underlying physics of MSs. This is despite the ambiguity about its appearance in the coronal emission lines, but the underlying physics is enough to draw this conclusion.

The spectroscopic readings, as show in ??, demonstrates a small, but appreciable perturbation in the rotational velocity of the jet like feature. We find that the jet exhibits a torsional behaviour, demonstrating shifts indicating rotation in one direction and then the other. The magnitude of these velocities is, however, low. we conclude that this is a result of the very small source loop of the feature, although this of course needs further enquiry.

With respect to the features affect on the atmosphere, we find a boundary interaction between the jet and atmosphere in the H $\alpha$  images. This interaction has manifested as dark streaks at the every edges of the feature during the same phase in which the second event causes the acceleration of further plasma. It is also the phase in which we observe the torsional rotation of the jet. Whether these dark streaks are physically significant we cannot comment upon too confidently at this time, but they appear at the same time as the second acceleration and the onset of rotational behaviour, cannot merely be coincidence.

# Chapter 6

## Conclusions

Macrospicules are an intriguing feature of the solar atmosphere. The work that is presented in this thesis has attempted to shed some light on these prevalent parts of the atmosphere. Chapter 3 can be easily compared to the previous works on a like-for-like basis. The previous examples of measurements, given by Bohlin et al. (1975) and Dere et al. (1989), are compared in ???. The values found here compare particularly well with Bohlin, however, the work by Dere finds more conservative values. Given the improved nature of instrumentation and measuring tools utilised in this work, we assert that the values found here should become the new expected measurements defining a macrospicule.

This study also found no divergence in the population of features measured. Such an effect could be expected were MSs very similar to another feature, but with separate underlying physics. Of course, the possibility remains that, they are part of a larger scale feature, such as X-ray jets, which, has been discussed on multiple occasions, Kamio et al. (2010); Parenti et al. (2002). In these cases, the jet-like features properties are similar to those of regular MSs, but there is no evidence to support this hypothesis within this study.

With respect to the ballistics and energetic of the feature, we find the unexpected effect of a macrospicule becoming thinner post apex of its motion. Another theory could be that the magnetic pressure would cause the width to increase, however the evidence does not agree with this, as such we need to think about the macrospicule not just as a column of regular plasma. The likely case is that the plasma begins to flow down the magnetic field lines, in a similar manner to evanescence, resulting in a decrease in the width of the feature.

Chapter 5 is the culmination of this thesis and is the most comprehensive view of a macrospicule in this work. The most significant result of which, is a demonstrated very clearly in the line of sight dopplergrams. The macrospicule feature

clearly shows a rotation initially in the anti-clockwise direction, before slowing in rate, stopping and then rotating clockwise. This is the first observation of such behaviour in MSs. There have been multiple observations and simulations demonstrating rotating jet-like features, [Curdt and Tian \(2011\)](#); [Kamio et al. \(2010\)](#); [Madjarska \(2011\)](#), however, this is the first work demonstrating torsional oscillating motion. It is also apparent that the feature 'unwinds' from the tip of the macrospicule downwards before developing across the entire feature. This unequivocally proves that MSs have an intrinsic magnetic field. This is interesting, as it has implications on the formation mechanism. If it were the case that these were merely an expulsion of plasma from a reconnection method highlighted in Section 1.2.2, a more complex process is underway.

Fortunately, the resolution of SST allows us to examine the footprint of the macrospicule. The conclusion that arises from this is that the macrospicule seems to undergo a formation event similar to the [Shibata et al. \(1992\)](#) standard jet formation model. The brightenings evident in the H $\alpha$ , show too much smaller brightpoints evolving and joining before the spire eventually forms. The extension of this feature in the lower temperature emission lines, where it extends the furthest, is roughly 12 Mm, not large for a macrospicule. And so, the fact that this small scale jet features a very similar formation profile to larger coronal jets. The implications for classification are that the waters are now muddied. Should MSs be classed as standard jets? Given that this feature is very thin, but Chapter 3 shows average widths of the order of 7 Mm, should the population be separated in terms of formation processes, standard and 'blowout' style MSs, similarly to Jets?

Macrospicules and their relationship (or lack thereof) with jets, will continue to be essential to our understanding of the solar atmosphere, given that they originate in the low chromosphere and extend up into the corona. The questions of the most importance at the moment are of their structure and formation mechanism. Both of these may be answered by the new DKIST telescope. The leap forward that DKIST will take with respect to spatial and temporal resolution will allow us to examine the footpoints of these features with significantly greater accuracy. Possibly more intriguing is the body of MSs themselves. Given the 'unwinding' of magnetic twist observed in Chapter 5, it may be possible to inspect individual strands of flux rope, which could answer:

- Are the MSs unwinding in all cases?
- Could the twisting motion be a result of a driver from below?
- Do the MSs always have a tortional or helical component?

- Can MSs be considered as a major factor with respect to heating or solar wind acceleration?

Those are just the questions considering MSs on their own. Macrospicules current place in the plethora of jet-like solar features is still far from clear, despite this work. Are MSs instances of multiple spicules ‘superposing’ and becoming a much larger feature as supposed by [Xia et al. \(2005\)](#)? Are they the cool component of X-ray jets as in [Parenti et al. \(2002\)](#)? In which case should we merely be calling them X-ray jets observed in chromospheric emission lines? There has been much work on the subject of H $\alpha$  and He II 30.4 nm MSs, including work by [Labonte \(1979\)](#); [Wang \(1998\)](#) but we have yet to conclusively prove that these features are one and the same. However, Chapter 5, again demonstrates that this is the case.

Hopefully the development of new solar observational instruments and the ever improving suite of data analysis tools, will lead us to answer these questions in the near future.



# References

- Adams, M., Sterling, A. C., Moore, R. L., and Gary, G. A. (2014). A Small-scale Eruption Leading to a Blowout Macrospicule Jet in an On-disk Coronal Hole. , 783:11.
- Alfvén, H. (1942). Existence of Electromagnetic-Hydrodynamic Waves. , 150:405–406.
- Almeida, J. S., Bonet, J. A., Viticchié, B., and Moro, D. D. (2010). Magnetic bright points in the quiet sun. *The Astrophysical Journal Letters*, 715(1):L26.
- Antiochos, S. K. (1998). The Magnetic Topology of Solar Eruptions. , 502:L181–L184.
- Archontis, V., Moreno-Insertis, F., Galsgaard, K., and Hood, A. W. (2005). The Three-dimensional Interaction between Emerging Magnetic Flux and a Large-Scale Coronal Field: Reconnection, Current Sheets, and Jets. , 635:1299–1318.
- Archontis, V. and Török, T. (2008). Eruption of magnetic flux ropes during flux emergence. , 492:L35–L38.
- Aschwanden, M. J., Winebarger, A., Tsiklauri, D., and Peter, H. (2007). The Coronal Heating Paradox. , 659:1673–1681.
- Athay, R. (2000). Are spicules related to coronal heating? *Solar Physics*, 197(1):31–42.
- Athay, R. G. and Beckers, J. M. (1976). The Solar Chromosphere and Corona: Quiet Sun. *Physics Today*, 29:74.
- Bai, T. and Sturrock, P. A. (1989). Classification of solar flares. , 27:421–467.
- Baker, D. N. (1995). The Inner Magnetosphere: A Review. *Surveys in Geophysics*, 16:331–362.
- Balthasar, H. and Schüssler, M. (1984). Evidence for the 22-YEAR-CYCLE in the Longitudinal Distribution of Sunspots. , 93:177–179.
- Beckers, J. M. (1972). Solar Spicules. , 10:73.

- Benevolenskaya, E. E., Kosovichev, A. G., and Scherrer, P. H. (1999). Structure and Dynamics of Interconnecting Loops and Coronal Holes in Active Longitudes. , 190:145–151.
- Bethe, H. A. (1939). Energy Production in Stars. *Physical Review*, 55:434–456.
- Bhardwaj, A., Dhanya, M. B., Alok, A., Barabash, S., Wieser, M., Futaana, Y., Wurz, P., Vorburger, A., Holmström, M., Lue, C., Harada, Y., and Asamura, K. (2015). A new view on the solar wind interaction with the Moon. *Geoscience Letters*, 2:10.
- Bohlin, J. D., Vogel, S. N., Purcell, J. D., Sheeley, Jr., N. R., Tousey, R., and Vanhoosier, M. E. (1975). A newly observed solar feature - Macrospicules in He II 304 Å. , 197:L133–L135.
- Brown, J. C. and Smith, D. F. (1980). Solar flares. *Reports on Progress in Physics*, 43:125–197.
- Brun, A. S. (2001). The solar tachocline: Where do we stand? In Wilson, A. and Pallé, P. L., editors, *SOHO 10/GONG 2000 Workshop: Helio- and Asteroseismology at the Dawn of the Millennium*, volume 464 of *ESA Special Publication*, pages 273–276.
- Bumba, V. and Howard, R. (1965). A Study of the Development of Active Regions on the Sun. , 141:1492.
- Cao, W., Gorceix, N., Coulter, R., Ahn, K., Rimmele, T. R., and Goode, P. R. (2010). Scientific instrumentation for the 1.6 m New Solar Telescope in Big Bear. *Astronomische Nachrichten*, 331:636.
- Chaplin, W. J. (2014). *Sounding the solar cycle with helioseismology: Implications for asteroseismology*, page 1.
- Chen, P. F. (2011). Coronal Mass Ejections: Models and Their Observational Basis. *Living Reviews in Solar Physics*, 8.
- Chidambara Aiyar, P. R. (1932). Two longitudinal zones of apparent inhibition of sunspots on the solar disc. , 93:150.
- Chifor, C., Isobe, H., Mason, H. E., Hannah, I. G., Young, P. R., Del Zanna, G., Krucker, S., Ichimoto, K., Katsukawa, Y., and Yokoyama, T. (2008). Magnetic flux cancellation associated with a recurring solar jet observed with Hinode, RHESSI, and STEREO/EUVI. , 491:279–288.
- Chitta, L. P., van Ballegooijen, A. A., van der Voort, L. R., DeLuca, E. E., and Kariyappa, R. (2012). Dynamics of the solar magnetic bright points derived from their horizontal motions. *The Astrophysical Journal*, 752(1):48.

- Choudhuri, A. R. (1998). *The physics of fluids and plasmas : an introduction for astrophysicists /.*
- Cranmer, S. R. (2009). Coronal Holes. *Living Reviews in Solar Physics*, 6.
- Curdt, W. and Tian, H. (2011). Spectroscopic evidence for helicity in explosive events. , 532:L9.
- De Pontieu, B., Erdélyi, R., and James, S. P. (2004). Solar chromospheric spicules from the leakage of photospheric oscillations and flows. , 430:536–539.
- De Pontieu, B., Hansteen, V. H., Rouppe van der Voort, L., van Noort, M., and Carlsson, M. (2007). Observations and Simulations of Fibrils and Mottles. *ArXiv Astrophysics e-prints*.
- de Pontieu, B., McIntosh, S., Hansteen, V. H., Carlsson, M., Schrijver, C. J., Tarbell, T. D., Title, A. M., Shine, R. A., Suematsu, Y., Tsuneta, S., Katsukawa, Y., Ichimoto, K., Shimizu, T., and Nagata, S. (2007). A Tale of Two Spicules: The Impact of Spicules on the Magnetic Chromosphere. , 59:S655–S662.
- Defise, J.-M., Halain, J.-P., Mazy, E., Rochus, P. P., Howard, R. A., Moses, J. D., Socker, D. G., Simnett, G. M., and Webb, D. F. (2001). Design of the Heliospheric Imager for the STEREO mission. In Siegmund, O. H., Fineschi, S., and Gummin, M. A., editors, *UV/EUV and Visible Space Instrumentation for Astronomy and Solar Physics*, volume 4498 of , pages 63–72.
- Dere, K. P., Bartoe, J.-D. F., Brueckner, G. E., Cook, J. W., and Socker, D. G. (1989). UV observations of macrospicules at the solar limb. , 119:55–63.
- Dezsö, L., Gerlei, O., and Kovács, Á. (1968). The Migration of Sunspot Activity Along Solar Meridians and Parallels. In Kiepenheuer, K. O., editor, *Structure and Development of Solar Active Regions*, volume 35 of *IAU Symposium*, page 70.
- De Pontieu, B., Title, A. M., Lemen, J. R., Kushner, G. D., Akin, D. J., Allard, B., Berger, T., Boerner, P., Cheung, M., Chou, C., Drake, J. F., Duncan, D. W., Freeland, S., Heyman, G. F., Hoffman, C., Hurlburt, N. E., Lindgren, R. W., Mathur, D., Rehse, R., Sabolish, D., Seguin, R., Schrijver, C. J., Tarbell, T. D., Wülser, J.-P., Wolfson, C. J., Yanari, C., Mudge, J., Nguyen-Phuc, N., Timmons, R., van Bezooijen, R., Weingrod, I., Brookner, R., Butcher, G., Dougherty, B., Eder, J., Knagenhjelm, V., Larsen, S., Mansir, D., Phan, L., Boyle, P., Cheimets, P. N., DeLuca, E. E., Golub, L., Gates, R., Hertz, E., McKillop, S., Park, S., Perry, T., Podgorski, W. A., Reeves, K., Saar, S., Testa, P., Tian, H., Weber, M., Dunn, C., Eccles, S., Jaeggli, S. A., Kankelborg, C. C., Mashburn, K., Pust, N., Springer, L., Carvalho, R., Kleint, L., Marmie, J., Mazmanian, E., Pereira, T. M. D., Sawyer, S., Strong, J., Worden, S. P., Carlsson, M., Hansteen, V. H., Leenaarts, J., Wiesmann, M., Aloise, J., Chu, K.-C.,

- Bush, R. I., Scherrer, P. H., Brekke, P., Martinez-Sykora, J., Lites, B. W., McIntosh, S. W., Uitenbroek, H., Okamoto, T. J., Gummin, M. A., Auker, G., Jerram, P., Pool, P., and Waltham, N. (2014). The interface region imaging spectrograph (iris). *Solar Physics*, 289(7):2733–2779.
- Dungey, J. (1953). Lxxvi. conditions for the occurrence of electrical discharges in astrophysical systems. *The London, Edinburgh, and Dublin Philosophical Magazine and Journal of Science*, 44(354):725–738.
- Engvold, O. (2004). Structures and Dynamics of Solar Filaments - challenges in observing and modeling. In Stepanov, A. V., Benevolenskaya, E. E., and Kosovichev, A. G., editors, *Multi-Wavelength Investigations of Solar Activity*, volume 223 of *IAU Symposium*, pages 187–194.
- Fan, Y. (2001). The Emergence of a Twisted  $\Omega$ -Tube into the Solar Atmosphere. , 554:L111–L114.
- Feng, L., Inhester, B., de Patoul, J., Wiegmann, T., and Gan, W. Q. (2012). Particle kinetic analysis of a polar jet from SECCHI COR data. , 538:A34.
- Fredricks, R. W. (1975). *Wave-Particle Interactions in the Outer Magnetosphere: A Review*, pages 113–152. Springer Netherlands, Dordrecht.
- Gaeng, T. (1998). The TRACE Mission: Technical Overview and Current Results. In Schielicke, R. E., editor, *Astronomische Gesellschaft Meeting Abstracts*, volume 14 of *Astronomische Gesellschaft Meeting Abstracts*.
- Garrard, T. L., Christian, E. R., Mewaldt, R. A., Ormes, J. F., and Stone, E. C. (1997). The Advanced Composition Explorer Mission. *International Cosmic Ray Conference*, 1:105.
- Giovanelli, R. G. (1946). A Theory of Chromospheric Flares. , 158:81–82.
- Gloeckler, G., Geiss, J., Balsiger, H., Bedini, P., Cain, J. C., Fischer, J., Fisk, L. A., Galvin, A. B., Gliem, F., Hamilton, D. C., Hollweg, J. V., Ipavich, F. M., Joos, R., Livi, S., Lundgren, R. A., Mall, U., McKenzie, J. F., Ogilvie, K. W., Ottens, F., Rieck, W., Tums, E. O., von Steiger, R., Weiss, W., and Wilken, B. (1992). The Solar Wind Ion Composition Spectrometer. , 92:267–289.
- Goedbloed, J. P. H. and Poedts, S. (2004). *Principles of Magnetohydrodynamics*.
- Golub, L. and Pasachoff, J. M. (2009). *The Solar Corona*.
- Gyenge, N., Baranyi, T., and Ludmány, A. (2012). Distribution of activity at the solar active longitudes between 1979 - 2011 in the northern hemisphere. *Central European Astrophysical Bulletin*, 36:9–16.

- Gyenge, N., Baranyi, T., and Ludmány, A. (2014). Migration and Extension of Solar Active Longitudinal Zones. , 289:579–591.
- Győri, L., Baranyi, T., and Ludmány, A. (2011). Photospheric data programs at the Debrecen Observatory. In Prasad Choudhary, D. and Strassmeier, K. G., editors, *Physics of Sun and Star Spots*, volume 273 of *IAU Symposium*, pages 403–407.
- Habbal, S. R. and Gonzalez, R. D. (1991). First observations of microspicules at 4.8 GHz at the solar limb in polar coronal holes. , 376:L25–L27.
- Hansen, C. J., Kawaler, S. D., and Trimble, V. (2004). *Stellar interiors : physical principles, structure, and evolution*.
- Hasan, S. S., van Ballegooijen, A. A., Kalkofen, W., and Steiner, O. (2005). Dynamics of the Solar Magnetic Network: Two-dimensional MHD Simulations. , 631:1270–1280.
- Heggland, L., De Pontieu, B., and Hansteen, V. H. (2009). Observational Signatures of Simulated Reconnection Events in the Solar Chromosphere and Transition Region. , 702:1–18.
- Hertzsprung, E. (1909). Über die Sterne der Unterabteilungen c und ac nach der Spektralklassifikation von Antonia C. Maury. *Astronomische Nachrichten*, 179:373.
- Hollweg, J. V. (1982). On the origin of solar spicules. , 257:345–353.
- Innes, D. E., Inhester, B., Axford, W. I., and Wilhelm, K. (1997). Bi-directional plasma jets produced by magnetic reconnection on the Sun. , 386:811–813.
- Isobe, H., Proctor, M. R. E., and Weiss, N. O. (2008). Convection-driven Emergence of Small-Scale Magnetic Fields and their Role in Coronal Heating and Solar Wind Acceleration. , 679:L57–L60.
- Jiang, Y. C., Chen, H. D., Li, K. J., Shen, Y. D., and Yang, L. H. (2007). The H $\alpha$  surges and EUV jets from magnetic flux emergences and cancellations. , 469:331–337.
- Kaiser, M. L., Kucera, T. A., Davila, J. M., St. Cyr, O. C., Guhathakurta, M., and Christian, E. (2008). The STEREO Mission: An Introduction. , 136:5–16.
- Kamio, S., Curdt, W., Teriaca, L., Inhester, B., and Solanki, S. K. (2010). Observations of a rotating macrospicule associated with an X-ray jet. , 510:L1.
- Kawaguchi, I. (1970). Observed Interaction between Prominences. , 22:405.
- Kayshap, P., Srivastava, A. K., Murawski, K., and Tripathi, D. (2013). Origin of Macrospicule and Jet in Polar Corona by a Small-scale Kinked Flux Tube. , 770:L3.

- Kim, Y.-H., Moon, Y.-J., Park, Y.-D., Sakurai, T., Chae, J., Cho, K. S., and Bong, S.-C. (2007). Small-Scale X-Ray/EUV Jets Seen in Hinode XRT and TRACE. , 59:S763–S769.
- Klimchuk, J. A. (2012). The role of type II spicules in the upper solar atmosphere. *Journal of Geophysical Research (Space Physics)*, 117:A12102.
- Kosugi, T., Matsuzaki, K., Sakao, T., Shimizu, T., Sone, Y., Tachikawa, S., Hashimoto, T., Minesugi, K., Ohnishi, A., Yamada, T., Tsuneta, S., Hara, H., Ichimoto, K., Suematsu, Y., Shimojo, M., Watanabe, T., Shimada, S., Davis, J. M., Hill, L. D., Owens, J. K., Title, A. M., Culhane, J. L., Harra, L. K., Doschek, G. A., and Golub, L. (2007). The hinode (solar-b) mission: An overview. *Solar Physics*, 243(1):3–17.
- Kudoh, T. and Shibata, K. (1999). Alfvén wave model of spicules and coronal heating. *The Astrophysical Journal*, 514(1):493.
- Kuridze, D., Henriques, V., Mathioudakis, M., Erdélyi, R., Zaqrashvili, T. V., Shelyag, S., Keys, P. H., and Keenan, F. P. (2015). The Dynamics of Rapid Redshifted and Blueshifted Excursions in the Solar H $\alpha$  Line. , 802:26.
- Kutner, M. L. (2003). *Astronomy: A Physical Perspective*.
- Labonte, B. J. (1979). Activity in the quiet sun. I - Observations of macrospicules in H-alpha and D3. , 61:283–296.
- Larson, R. B. (2003). The physics of star formation. *Reports on Progress in Physics*, 66:1651–1697.
- Lee, D. and Deane, A. E. (2009). An unsplit staggered mesh scheme for multidimensional magnetohydrodynamics. *Journal of Computational Physics*, 228:952–975.
- Lemen, J. R., Title, A. M., Akin, D. J., Boerner, P. F., Chou, C., Drake, J. F., Duncan, D. W., Edwards, C. G., Friedlaender, F. M., Heyman, G. F., Hurlburt, N. E., Katz, N. L., Kushner, G. D., Levay, M., Lindgren, R. W., Mathur, D. P., McFeaters, E. L., Mitchell, S., Rehse, R. A., Schrijver, C. J., Springer, L. A., Stern, R. A., Tarbell, T. D., Wuelser, J.-P., Wolfson, C. J., Yanari, C., Bookbinder, J. A., Cheimets, P. N., Caldwell, D., Deluca, E. E., Gates, R., Golub, L., Park, S., Podgorski, W. A., Bush, R. I., Scherrer, P. H., Gummin, M. A., Smith, P., Auker, G., Jerram, P., Pool, P., Soufli, R., Windt, D. L., Beardsley, S., Clapp, M., Lang, J., and Waltham, N. (2012). The atmospheric imaging assembly (aia) on the solar dynamics observatory (sdo). *Solar Physics*, 275(1):17–40.
- Leonard, A. and Morgan, H. (2014). Temperature diagnostics of the solar atmosphere using SunPy. *ArXiv e-prints*.

- Li, C., Matthews, S. A., van Driel-Gesztelyi, L., Sun, J., and Owen, C. J. (2011). Coronal jets, magnetic topologies, and the production of interplanetary electron streams. *The Astrophysical Journal*, 735(1):43.
- Li, J. (2011). Active longitudes revealed by large-scale and long-lived coronal streamers. *The Astrophysical Journal*, 735(2):130.
- Liu, Z., Deng, Y., and Ji, H. (2014). The Chinese Giant Solar Telescope. In Schmieder, B., Malherbe, J.-M., and Wu, S. T., editors, *Nature of Prominences and their Role in Space Weather*, volume 300 of *IAU Symposium*, pages 349–354.
- Madjarska, M. S. (2011). Dynamics and plasma properties of an X-ray jet from SUMER, EIS, XRT, and EUVIA B simultaneous observations. , 526:A19.
- Manchester, IV, W. B., Gombosi, T. I., De Zeeuw, D. L., Sokolov, I. V., Roussev, I. I., Powell, K. G., Kóta, J., Tóth, G., and Zurbuchen, T. H. (2005). Coronal Mass Ejection Shock and Sheath Structures Relevant to Particle Acceleration. , 622:1225–1239.
- Mariska, J. T. (1986). The quiet solar transition region. , 24:23–48.
- Martínez-Sykora, J., Hansteen, V., and Moreno-Insertis, F. (2011). On the Origin of the Type II Spicules: Dynamic Three-dimensional MHD Simulations. , 736:9.
- McComas, D. J., Elliott, H. A., Schwadron, N. A., Gosling, J. T., Skoug, R. M., and Goldstein, B. E. (2003). The three-dimensional solar wind around solar maximum. , 30:24–1.
- Moe, O. K., Beckers, J. M., and Engvold, O. (1975). A comparison of spicules in the H-alpha and He II /304 Å/ lines. , 40:65–68.
- Moore, R. L., Cirtain, J. W., Sterling, A. C., and Falconer, D. A. (2010). Dichotomy of solar coronal jets: Standard jets and blowout jets. *The Astrophysical Journal*, 720(1):757.
- Moore, R. L., Sterling, A. C., Cirtain, J. W., and Falconer, D. A. (2011). Solar X-ray Jets, Type-II Spicules, Granule-size Emerging Bipoles, and the Genesis of the Heliosphere. , 731:L18.
- Moore, R. L., Tang, F., Bohlin, J. D., and Golub, L. (1977). H-alpha macrospicules - Identification with EUV macrospicules and with flares in X-ray bright points. , 218:286–290.
- Moreno-Insertis, F., Galsgaard, K., and Ugarte-Urra, I. (2008). Jets in Coronal Holes: Hinode Observations and Three-dimensional Computer Modeling. , 673:L211.
- Morton, R. J. (2012). Chromospheric jets around the edges of sunspots. , 543:A6.

- Moschou, S. P., Tsinganos, K., Vourlidas, A., and Archontis, V. (2013). SDO Observations of Solar Jets. , 284:427–438.
- Muller, R. and Roudier, T. (1992). Formation of network bright points by granule compression. , 141:27–33.
- Murawski, K., Srivastava, A. K., and Zaqrashvili, T. V. (2011). Numerical simulations of solar macrospicules. , 535:A58.
- Mursula, K. and Hiltula, T. (2004). Systematically Asymmetric Heliospheric Magnetic Field: Evidence for a Quadrupole Mode and Non-Axisymmetry with Polarity Flip-Flops. , 224:133–143.
- Narang, N., Arbacher, R. T., Tian, H., Banerjee, D., Cranmer, S. R., DeLuca, E. E., and McKillop, S. (2016). Statistical study of network jets observed in the solar transition region: a comparison between coronal holes and quiet-sun regions. *Solar Physics*, 291(4):1129–1142.
- Nishizuka, N., Nakamura, T., Kawate, T., Singh, K. A. P., and Shibata, K. (2011). Statistical Study of Chromospheric Anemone Jets Observed with Hinode/SOT. , 731:43.
- Obridko, V. N. and Shelting, B. D. (2007). Occurrence of the 1.3-year periodicity in the large-scale solar magnetic field for 8 solar cycles. *Advances in Space Research*, 40:1006–1014.
- Owens, M. J. and Forsyth, R. J. (2013). The Heliospheric Magnetic Field. *Living Reviews in Solar Physics*, 10.
- Parenti, S., Bromage, B. J. I., and Bromage, G. E. (2002). An erupting macrospicule. Characteristics derived from SOHO-CDS spectroscopic observations. , 384:303–316.
- Parker, E. N. (1957). Sweet's Mechanism for Merging Magnetic Fields in Conducting Fluids. , 62:509–520.
- Patsourakos, S., Vial, J.-C., Gabriel, A. H., and Bellamine, N. (1999). Transition-Region Network Boundaries in the Quiet Sun: Width Variation with Temperature as Observed with CDS on SOHO. , 522:540–546.
- Pereira, T. M. D., De Pontieu, B., and Carlsson, M. (2012). Quantifying Spicules. , 759:18.
- Pereira, T. M. D., De Pontieu, B., Carlsson, M., Hansteen, V., Tarbell, T. D., Lemen, J., Title, A., Boerner, P., Hurlburt, N., Wülser, J. P., Martínez-Sykora, J., Kleint, L., Golub, L., McKillop, S., Reeves, K. K., Saar, S., Testa, P., Tian, H., Jaeggli, S., and

- Kankelborg, C. (2014). An Interface Region Imaging Spectrograph First View on Solar Spicules. , 792:L15.
- Petschek, H. E. (1964). Magnetic Field Annihilation. *NASA Special Publication*, 50:425.
- Pike, C. D. and Harrison, R. A. (1997). Euv observations of a macrospicule: Evidence for solar wind acceleration? *Solar Physics*, 175(2):457–465.
- Pike, C. D. and Mason, H. E. (1998). Rotating Transition Region Features Observed with the SOHO Coronal Diagnostic Spectrometer. , 182:333–348.
- Priest, E. and Forbes, T. (2007). *Magnetic Reconnection*.
- Reale, F. (2014). Coronal Loops: Observations and Modeling of Confined Plasma. *Living Reviews in Solar Physics*, 11.
- Richey, M. (2010). The evolution of markov chain monte carlo methods. *The American Mathematical Monthly*, 117(5):383–413.
- Rimmele, T. R. and Marino, J. (2011). Solar Adaptive Optics. *Living Reviews in Solar Physics*, 8.
- Rouppé van der Voort, L., De Pontieu, B., Pereira, T. M. D., Carlsson, M., and Hansteen, V. (2015). Heating Signatures in the Disk Counterparts of Solar Spicules in Interface Region Imaging Spectrograph Observations. , 799:L3.
- Rouppé van der Voort, L., Leenaarts, J., de Pontieu, B., Carlsson, M., and Vissers, G. (2009). On-disk Counterparts of Type II Spicules in the Ca II 854.2 nm and H $\alpha$  Lines. , 705:272–284.
- Russell, H. N. (1914). Relations Between the Spectra and Other Characteristics of the Stars. *Popular Astronomy*, 22:275–294.
- Saha, M. N. (1920). Ionisation in the Solar Chromosphere. , 105:232–233.
- Scharmer, G. B., Bjelksjo, K., Korhonen, T. K., Lindberg, B., and Petterson, B. (2003). The 1-meter Swedish solar telescope. In Keil, S. L. and Avakyan, S. V., editors, *Innovative Telescopes and Instrumentation for Solar Astrophysics*, volume 4853 of , pages 341–350.
- Schmelz, J. T., Jenkins, B. S., and Kimble, J. A. (2013). Atmospheric Imaging Assembly Response Functions: Solving the Fe viii Problems with Hinode EIS Bright Point Data. , 283:325–340.
- Schwarzschild, M. (1958). *Structure and evolution of the stars*.

- Scullion, E., Doyle, J. G., and Erdélyi, R. (2010). A spectroscopic analysis of macrospicules . , 81:737.
- Sekse, D. H., Rouppe van der Voort, L., De Pontieu, B., and Scullion, E. (2013). Interplay of Three Kinds of Motion in the Disk Counterpart of Type II Spicules: Upflow, Transversal, and Torsional Motions. , 769:44.
- Shibata, K., Ishido, Y., Acton, L. W., Strong, K. T., Hirayama, T., Uchida, Y., McAllister, A. H., Matsumoto, R., Tsuneta, S., Shimizu, T., Hara, H., Sakurai, T., Ichimoto, K., Nishino, Y., and Ogawara, Y. (1992). Observations of X-ray jets with the YOHKOH Soft X-ray Telescope. , 44:L173–L179.
- Shibata, K., Nitta, N., Strong, K. T., Matsumoto, R., Yokoyama, T., Hirayama, T., Hudson, H., and Ogawara, Y. (1994). A gigantic coronal jet ejected from a compact active region in a coronal hole. , 431:L51–L53.
- Shibata, K. and Suematsu, Y. (1982). Why are spicules absent over plages and long under coronal holes. , 78:333–345.
- Shibata, K. and Uchida, Y. (1986). Sweeping-magnetic-twist mechanism for the acceleration of jets in the solar atmosphere. , 103:299–310.
- Shimojo, M., Hashimoto, S., Shibata, K., Hirayama, T., Hudson, H. S., and Acton, L. W. (1996). Statistical Study of Solar X-Ray Jets Observed with the YOHKOH Soft X-Ray Telescope. , 48:123–136.
- Shimojo, M. and Shibata, K. (2000). Physical Parameters of Solar X-Ray Jets. , 542:1100–1108.
- St. Cyr, O. C., Sánchez-Duarte, L., Martens, P. C. H., Gurman, J. B., and Larduinat, E. (1995). SOHO Ground Segment, Science Operations, and Data Products. , 162:39–59.
- Sterling, A. C. (2000). Solar Spicules: A Review of Recent Models and Targets for Future Observations - (Invited Review). , 196:79–111.
- Sweet, P. A. (1958). The Neutral Point Theory of Solar Flares. In Lehnert, B., editor, *Electromagnetic Phenomena in Cosmical Physics*, volume 6 of *IAU Symposium*, page 123.
- Takeuchi, A. and Shibata, K. (2001). Magnetic Reconnection Induced by Convective Intensification of Solar Photospheric Magnetic Fields. , 546:L73–L76.
- Tian, H., DeLuca, E. E., Cranmer, S. R., De Pontieu, B., Peter, H., Martínez-Sykora, J., Golub, L., McKillop, S., Reeves, K. K., Miralles, M. P., McCauley, P., Saar, S., Testa, P., Weber, M., Murphy, N., Lemen, J., Title, A., Boerner, P., Hurlburt, N., Tarbell,

- T. D., Wuelser, J. P., Kleint, L., Kankelborg, C., Jaeggli, S., Carlsson, M., Hansteen, V., and McIntosh, S. W. (2014). Prevalence of small-scale jets from the networks of the solar transition region and chromosphere. *Science*, 346(27):1255711.
- Tsiropoula, G., Tziotziou, K., Kontogiannis, I., Madjarska, M. S., Doyle, J. G., and Suematsu, Y. (2012). Solar Fine-Scale Structures. I. Spicules and Other Small-Scale, Jet-Like Events at the Chromospheric Level: Observations and Physical Parameters. , 169:181–244.
- Tsuneta, S., Acton, L., Bruner, M., Lemen, J., Brown, W., Caravalho, R., Catura, R., Freeland, S., Jurcevich, B., Morrison, M., Ogawara, Y., Hirayama, T., and Owens, J. (1991). The Soft X-ray Telescope for the SOLAR-A Mission. , 136:37–67.
- Ulmschneider, P. and Stein, R. F. (1982). Heating of stellar chromospheres when magnetic fields are present. , 106:9–13.
- Usoskin, I. G., Berdyugina, S. V., and Poutanen, J. (2005). Preferred sunspot longitudes: non-axisymmetry and differential rotation. , 441:347–352.
- van Noort, M., Rouppe van der Voort, L., and Löfdahl, M. G. (2005). Solar Image Restoration By Use Of Multi-frame Blind De-convolution With Multiple Objects And Phase Diversity. , 228:191–215.
- Vernazza, J. E., Avrett, E. H., and Loeser, R. (1981). Structure of the solar chromosphere. III - Models of the EUV brightness components of the quiet-sun. , 45:635–725.
- Vourlidas, A. (2006). A Review of White Light Streamers at the End of Cycle 23. In Bothmer, V. and Hady, A. A., editors, *Solar Activity and its Magnetic Origin*, volume 233 of *IAU Symposium*, pages 197–204.
- Wang, H. (1998). Comparison of H $\alpha$  and He II  $\lambda$ 304 Macrospicules. , 509:461–470.
- Welsch, B. T. (2006). Magnetic Flux Cancellation and Coronal Magnetic Energy. , 638:1101–1109.
- Wenzel, K. P., Marsden, R. G., Page, D. E., and Smith, E. J. (1992). The ULYSSES Mission. , 92:207.
- Wilkinson, W. P. (2003). The Earth's quasi-parallel bow shock: Review of observations and perspectives for Cluster. , 51:629–647.
- Withbroe, G. L., Jaffe, D. T., Foukal, P. V., Huber, M. C. E., Noyes, R. W., Reeves, E. M., Schmahl, E. J., Timothy, J. G., and Vernazza, J. E. (1976). Extreme-ultraviolet transients observed at the solar pole. , 203:528–532.

- Withbroe, G. L. and Noyes, R. W. (1977). Mass and energy flow in the solar chromosphere and corona. , 15:363–387.
- Wyper, P. F. and DeVore, C. R. (2016). Simulations of Solar Jets Confined by Coronal Loops. , 820:77.
- Xia, L. D., Popescu, M. D., Doyle, J. G., and Giannikakis, J. (2005). Time series study of euv spicules observed by sumer/soho. *A&A*, 438(3):1115–1122.
- Yamauchi, Y., Moore, R. L., Suess, S. T., Wang, H., and Sakurai, T. (2004). Macrospicules, Coronal Heating, and SolarB. In Sakurai, T. and Sekii, T., editors, *The Solar-B Mission and the Forefront of Solar Physics*, volume 325 of *Astronomical Society of the Pacific Conference Series*, page 301.
- Zaqarashvili, T. V. and Erdélyi, R. (2009). Oscillations and Waves in Solar Spicules. , 149:355–388.
- Zaqarashvili, T. V., Vörös, Z., and Zhelyazkov, I. (2014). Kelvin-Helmholtz instability of twisted magnetic flux tubes in the solar wind. , 561:A62.
- Zhang, L. Y., Wang, H. N., Du, Z. L., Cui, Y. M., and He, H. (2007). Long-term behavior of active longitudes for solar X-ray flares. , 471:711–716.
- Zhang, Y. Z., Shibata, K., Wang, J. X., Mao, X. J., Matsumoto, T., Liu, Y., and Su, J. T. (2012). Revision of Solar Spicule Classification. , 750:16.
- Åke Nordlund, Stein, R. F., and Asplund, M. (2009). Solar surface convection. *Living Reviews in Solar Physics*, 6(2).